

NONLINEAR OPTICS OF
PLANAR METAMATERIAL ARRAYS
AND
SPECTROSCOPY OF INDIVIDUAL
“PHOTONIC ATOMS”

Zur Erlangung des akademischen Grades eines
DOKTORS DER NATURWISSENSCHAFTEN
der Fakultät für Physik des
Karlsruher Instituts für Technologie (KIT)

genehmigte

DISSERTATION

von

Diplom-Physiker Nils-Agne Feth
aus Frankfurt/Main

Tag der mündlichen Prüfung: 22. Januar 2010
Referent: Prof. Dr. Martin Wegener
Korreferent: Prof. Dr. Kurt Busch

Contents

1	Introduction	1
2	Basic principles of optics	5
2.1	Linear optics	5
2.1.1	Maxwell's equations	5
2.1.2	Wave equation	7
2.1.3	Fourier transformation	8
2.1.4	Transmittance, reflectance and absorption	8
2.1.5	Interaction of a plane wave with a single scatterer	10
2.1.6	Linear optical properties of dielectrics in the Lorentz model	12
2.1.7	Linear optical properties of metals	14
2.2	Nonlinear optics	21
2.2.1	Second-order nonlinear optical effects	21
2.2.2	Third-order nonlinear optical effects	22
2.2.3	Damped anharmonic oscillator	22
2.2.4	Metals in the hydro-dynamic approach	24
2.3	The electromagnetic local density of states	26
2.4	Electron-energy-loss spectroscopy	28
2.5	Gaussian beams	30
3	The metamaterial concept	33
3.1	Effective-medium theory	34
3.2	Diluted metal	35
3.3	Split-ring resonator as magnetic atom	35
3.3.1	Split-ring resonator in the plasmonic picture	36
3.3.2	Split-ring resonator as <i>RLC</i> -circuit	38
3.3.3	Excitation geometries	40
3.3.4	Modifications of the split-ring resonator	42
3.4	A photonic negative-index metamaterial	42
3.5	Optical phenomena in metamaterials	44
3.5.1	Magnetic Brewster angle	44
3.5.2	Magnetic surface waves	45
3.5.3	Negative refractive index	46

3.5.4	Transformation optics	47
4	Experimental methods I: fabrication	49
4.1	Electron-beam lithography	49
4.1.1	Sample preparation	49
4.1.2	Lithography	51
4.1.3	Post-processing	53
4.1.4	Fabrication of CSRRs	54
4.1.5	Fabrication of isolated SRRs	55
4.1.6	Fabrication of SRRs on ultra thin substrates	55
4.2	Focused-ion-beam lithography	56
4.3	Laser-interference lithography	57
4.4	Nano-imprint lithography	57
5	Experimental methods II: characterization	59
5.1	Linear optical characterization	59
5.2	Nonlinear optical characterization	60
5.3	Spatial modulation technique	61
5.3.1	A small particle in a Gaussian focus	63
5.3.2	A small particle outside a Gaussian focus	65
5.3.3	Connection to the experiment	66
5.3.4	Experimental setup	68
5.3.5	Sample design	70
5.4	EELS of isolated photonic atoms	71
5.4.1	Experimental setup	72
5.4.2	Numerical analysis of the experimental data	74
6	Nonlinear optical experiments	77
6.1	SHG on complementary split-ring resonators	78
6.1.1	Experimental results	78
6.1.2	Numerical results	81
6.2	THG on complementary split-ring resonators	81
6.3	Conclusion	84
7	Linear optical experiments	85
7.1	Optical properties of isolated SRRs	85
7.2	Interaction effects in SRR dimers	89
7.2.1	The dipole-dipole interaction model	90
7.2.2	Investigated SRR dimer configurations	92
7.2.3	Experimental and numerical results	93
7.3	Conclusion	97

8	Mapping particle plasmons of SRRs	101
8.1	The SRR's eigenmodes in the antenna model	102
8.2	Results and discussion	103
8.3	Conclusion	105
9	Conclusions and outlook	107
A	Derivation of the Optical Theorem	111
B	Step-by-step analysis	113
B.1	A small particle in a Gaussian focus	113
B.2	A small particle outside a Gaussian focus	116
	Bibliography	118

Publications

Parts of this work have already been published in refereed scientific journals

- N. Feth, S. Linden, M. W. Klein, M. Decker, F. B. P. Niesler, Y. Zeng, W. Hoyer, J. Liu, S. W. Koch, J. V. Moloney, and M. Wegener, “Second-harmonic generation from complementary split-ring resonators,” *Opt. Lett.* **33**, 1975–1977 (2008)
- M. Husnik, M. W. Klein, N. Feth, M. König, J. Niegemann, K. Busch, S. Linden, and M. Wegener, “Absolute extinction cross-section of individual magnetic split-ring resonators,” *Nature Photon.* **2**, 614–617 (2008)

Parts of this work have been submitted to scientific journals

- N. Feth, M. König, M. Husnik, K. Stannigel, J. Niegemann, K. Busch, M. Wegener, and S. Linden, “Electromagnetic interaction of split-ring resonators: The role of separation and relative orientation,” submitted (2009)

Additional work on other topics has been published in refereed scientific journals

- M. W. Klein, M. Wegener, N. Feth, and S. Linden “Experiments on second- and third-harmonic generation from magnetic metamaterials,” *Opt. Exp.* **15**, 5238–5247 (2007) and “Experiments on second- and third-harmonic generation from magnetic metamaterials: erratum,” *Opt. Exp.* **16**, 8055–8055 (2008)
- F. B. P. Niesler, N. Feth, S. Linden, J. Niegemann, J. Gieseler, K. Busch, and M. Wegener, “Second-harmonic generation from split-ring resonators on GaAs substrate,” *Opt. Lett.* **34**, 1997–1999 (2009)

Chapter 1

Introduction

Electromagnetic radiation of all frequencies is – apart from our visual perception – of overwhelming importance for both scientific and technological achievements of the modern world. In science, light is frequently used as a probe for the investigation of the fundamental properties of matter. For instance, experiments on the linear interaction between light and atoms revolutionized physics by paving the way to Quantum Mechanics. Especially, the laser realized by T. H. Maiman in 1960 [1] nowadays serves as reliable and powerful tool for investigating light-matter interactions. It made new fields of optics accessible, for example nonlinear optics in which electromagnetic fields can interact with each other *via* excitations of a medium leading.

Without precise control over electromagnetic waves by controlling their electric-field component, technologies we use on an every-day basis like telecommunication, optical data storage, and such “simple” things as microwave ovens would simply not be possible. Nowadays, data is primarily transmitted *via* optical fibers guiding the light with small losses and superior bandwidth – even this year’s Nobel prize has been awarded to C. K. Kao, the pioneer in optical communication through fibers. Most of these modern technologies rely on classical electromagnetism. Its theoretical and experimental foundations have been established much earlier, by J. C. Maxwell in 1864 and by H. Hertz in 1888, respectively [2]. In this context, it is noteworthy that H. Hertz performed his groundbreaking experiments at the Technische Hochschule in Karlsruhe – just a few hundred meters away from the laboratories where our optical experiments are carried out. Although, this work was done more than 120 years ago, classical electromagnetism still provides many interesting and highly competitive fields of research.

One of the most recent examples for such a research field is the development of metamaterials. These are composite materials, whose fundamental building blocks (“photonic atoms”) are arranged with a period much smaller than the corresponding wavelength of the light. This allows for describing the metamaterial’s optical properties by effective material parameters: the refractive index n , impedance Z , permittivity ϵ and the permeability μ . By a proper design of the photonic atoms and their relative arrangement, these effective parameters can be tailored in a desired way. Especially intriguing is the possibility of a permeability different from one at elevated frequencies, that is, frequencies in the GHz-regime and above

(1GHz = 10^9 Hz) since such materials are simply not provided by nature. In addition, astonishing optical properties have been proposed and demonstrated for materials with designed values of the permittivity and the permeability as, for example, a negative refractive index n [3]. Generally speaking, metamaterials promise precise control over electromagnetic waves *via* their electric- *and* their magnetic-field components.

A permeability different from unity requires magnetic dipoles oscillating with a sufficiently large oscillator strength. In this context, in 1999, J. B. Pendry *et al.* [4] introduced the splitting resonator (SRR) as a functional element with a magnetic dipole moment at elevated frequencies. In essence, the SRR is a tiny metallic ring with a small gap. An incident light field can induce a circulating ring current that generates an out-of-plane magnetic dipole moment. In analogy to electric circuit theory, the SRR can be described as *LC*-circuit with a coil of one winding and a capacitor formed by the gap. For the proper frequency, the *LC*-circuit is driven in resonance for which the magnetic dipole moment becomes maximal. Densely packed SRRs lead to an overall magnetic response, which in turn can be described by a permeability different from one. Hence, SRRs can be considered as the prototypical fundamental building blocks for most metamaterials with a magnetic response.

V. Veselago discussed in Ref. [3] the properties of an at the time fictitious material exhibiting simultaneously a negative permittivity and a negative permeability as early as 1968. However, the stimulus for starting intensive research on metamaterials was a publication by J. B. Pendry [5]. Here, he proposed that a flat slab of a material with $\epsilon = \mu = -1$ (and hence $n = -1$) works as a perfect lens allowing for images with perfect resolution. A dream seemed to come true: deep sub-wavelength resolution would have a tremendous impact on, for instance, optical microscopy or optical lithography. In general, both suffer from Abbe's resolution limit [6].

The concept of transformation optics and especially electromagnetic cloaking introduced by U. Leonhardt and J. B. Pendry *et al.* [7, 8] was another stimulus for intensive research activities in the field of metamaterials [9–13]. In transformation optics, a spatial distribution of the permittivity $\epsilon(\mathbf{r})$ and the permeability $\mu(\mathbf{r})$ is tailored such that light travels along a desired path.

The ultimate goal in the research on metamaterials is realizing the corresponding phenomena at optical frequencies [14, 15]. On this way, many challenges have to be faced. Since in the GHz- and THz-regime metals behave like almost perfect conductors, electromagnetic waves induce surface excitations in metallic objects. In contrast, in the optical domain, the wave penetrates substantially into the metallic nanoparticle. As a consequence, the entire electron gas – the so-called plasma of the metallic nanoparticle participates in the excitations induced by electromagnetic radiation. The optical properties of metallic nanoparticles that are connected to these excitations are investigated in another current field of research: plasmonics. Additionally, the above mentioned miniaturization of the fundamental building blocks for a response in the optical domain requires using state-of-the-art fabrication technologies and still remains challenging. Thus, bringing the metamaterial response from the microwave and THz-regime to the optical domain, merges the metamaterial concept with plasmonics and state-of-the-art fabrication technologies.

Clearly, the best starting point for understanding the optical properties of metamaterials and

the underlying physics is to investigate their individual building blocks. This is exactly what we do in this work by measuring both the absolute extinction-cross-section spectra of isolated split-ring resonators and the electron-energy-loss spectra that allow for mapping plasmonic modes with deep sub-wavelength spatial resolution. We even go one step further by investigating the interaction in pairs of split-ring resonators.

Light is confined by resonant metallic objects to length scales well-below the operating wavelength – even in the optical spectral range. This confinement together with the intrinsic nonlinearity of metals promises an extremely interesting playground for nonlinear optics of metallic nanoparticles. This idea was partly picked up in the above mentioned publication of Pendry and coworkers [4], who pointed out that SRRs may possess extraordinary nonlinear optical properties due to the high electric field in the gap of the loop. Indeed, first experiments on SRR arrays [16–18] confirmed this promise. In this thesis, we report on subsequent experiments on complementary SRRs (CSRRs) exhibiting the same symmetry but different electromagnetic near fields.

Before we move on to the outline of this thesis, we dedicate the last sentences of the Introduction to an astonishingly actual aspect of H. Hertz’ experiments: his experimental apparatus consisted of a transmitter generating radio waves and a receiver which essentially was a macroscopic metallic loop with a tiny split – a very early split-ring resonator that enabled the detection of the radio waves *via* their electromagnetic fields. Nowadays, we use the same design miniaturized down to the nanometer scale to couple to the magnetic component of the light field and utilize this coupling to manipulate the properties of light through its magnetic field component – a possibility not provided by nature in the optical spectral range.

Outline of this thesis

This work comprises two main parts: (i) the nonlinear optical properties of metamaterial arrays and (ii) optical and electron-energy-loss spectroscopy on individual photonic atoms. Thus, in chapter 2, we review the basic principles of linear and nonlinear optics, as well as the interaction of fast electrons with photonic systems that is capitalized on in electron-energy-loss spectroscopy. Chapter 3 is dedicated to the metamaterial concept with focus on the introduction of the split-ring resonator as *the* photonic atom with a magnetic dipole moment. Additionally, we try to stimulate the reader’s enthusiasm for metamaterials by a short review of some astonishing optical phenomena metamaterials allow for. The experimental methods used for fabrication and characterization of metamaterial arrays and individual photonic atoms are reported in chapter 4 and 5. In chapter 6, we discuss the nonlinear optical properties, that is, the second- and third-harmonic generation (SHG and THG, respectively) of complementary split-ring resonators in direct comparison to split-ring resonators under normal incidence. The absolute SHG conversion efficiencies are directly compared to numerical calculations based on a microscopic theory of the second-order nonlinearity of metals. We address the linear optical properties of individual split-ring resonators and the coupling mechanism in pairs of split-ring resonators in chapter 7. Also for these experiments, the experimental results are directly compared to microscopic numerical calculations. Chapter 8 is devoted to our work on electron-energy-loss spectroscopy of individual split-ring resonators.

We achieve a mapping of the occurring plasmonic modes on the nanometer scale. Finally, we conclude and give a short outlook in chapter 9.

Chapter 2

Basic principles of optics

The optical properties of metamaterials rely on linear and nonlinear interactions of electromagnetic waves with matter. In general, these interactions are described by Maxwell's equations and the dispersion properties of the constituting materials. Thus, in this chapter, we introduce Maxwell's equations describing the basic properties of electromagnetic fields first. Then, we present the linear and nonlinear interaction of electromagnetic waves with optical media. Here, our focus lies on the interaction with metals and metallic particles. Finally, we consider the interaction of charged particles with matter.

2.1 Linear optics

2.1.1 Maxwell's equations

The properties of classical electromagnetic fields in media are completely described by the macroscopic Maxwell equations. In SI-units, they read [2]

$$\nabla \cdot \mathbf{D}(\mathbf{r}, t) = \rho(\mathbf{r}, t), \quad (2.1a)$$

$$\nabla \cdot \mathbf{B}(\mathbf{r}, t) = 0, \quad (2.1b)$$

$$\nabla \times \mathbf{E}(\mathbf{r}, t) = -\frac{\partial \mathbf{B}(\mathbf{r}, t)}{\partial t}, \quad (2.1c)$$

$$\nabla \times \mathbf{H}(\mathbf{r}, t) = \mathbf{j}(\mathbf{r}, t) + \frac{\partial \mathbf{D}(\mathbf{r}, t)}{\partial t}, \quad (2.1d)$$

with the dielectric displacement $\mathbf{D}(\mathbf{r}, t)$, the electric field $\mathbf{E}(\mathbf{r}, t)$, the magnetic field $\mathbf{H}(\mathbf{r}, t)$, the magnetic induction $\mathbf{B}(\mathbf{r}, t)$, the external charge density $\rho(\mathbf{r}, t)$, and the external current density $\mathbf{j}(\mathbf{r}, t)$.

The external charge density and the external current density are connected through the charge conservation law, also known as continuity equation

$$\nabla \cdot \mathbf{j}(\mathbf{r}, t) + \frac{\partial \rho(\mathbf{r}, t)}{\partial t} = 0. \quad (2.2)$$

Here, we use the term “external” since all “internal” charge separations and currents induced by the electromagnetic fields lead to a macroscopic electric polarization \mathbf{P} and a macroscopic

magnetization \mathbf{M} . These two physical quantities influence the wave propagation in media and connect the dielectric displacement and the magnetic induction with the electric and magnetic field, respectively *via* the material equations

$$\mathbf{D}(\mathbf{r}, t) = \epsilon_0 \mathbf{E}(\mathbf{r}, t) + \mathbf{P}(\mathbf{r}, t), \quad (2.3a)$$

$$\mathbf{B}(\mathbf{r}, t) = \mu_0 \mathbf{H}(\mathbf{r}, t) + \mathbf{M}(\mathbf{r}, t). \quad (2.3b)$$

Here, we introduced the permittivity of free space $\epsilon_0 = \frac{1}{c_0^2 \mu_0} = 8.85 \times 10^{-12} \text{ F/m}$ with the vacuum speed of light $c_0 = 299792458 \text{ m/s}$ and the permeability of free space $\mu_0 = 1.27 \times 10^{-6} \text{ Tm/A}$.

In linear optics, the polarization and the magnetization are connected to the external fields \mathbf{E} and \mathbf{H} *via* the electric and magnetic susceptibilities $\chi_e(\mathbf{r} - \mathbf{r}', t - t')$ and $\chi_m(\mathbf{r} - \mathbf{r}', t - t')$, respectively, leading to (in the dipole limit) [2]

$$\mathbf{P}(\mathbf{r}, t) = \int_{-\infty}^{\infty} \int_{-\infty}^t \epsilon_0 \chi_e(\mathbf{r} - \mathbf{r}', t - t') \mathbf{E}(\mathbf{r}', t') dt' d^3 r', \quad (2.4a)$$

$$\mathbf{M}(\mathbf{r}, t) = \int_{-\infty}^{\infty} \int_{-\infty}^t \mu_0 \chi_m(\mathbf{r} - \mathbf{r}', t - t') \mathbf{H}(\mathbf{r}', t') dt' d^3 r'. \quad (2.4b)$$

In general, both susceptibilities are second rank tensors. Since most materials are isotropic, the susceptibilities become scalar implying that the induced electric and magnetic dipoles are aligned parallel or antiparallel to the corresponding external fields. Furthermore, most materials provide a local response. Consequently, we can omit the integration over $d^3 r'$. Accordingly, in linear optics, we rewrite Eqs. (2.3a) and (2.3b) in frequency domain (see section 2.1.3) as

$$\mathbf{D}(\mathbf{r}, \omega) = \epsilon_0 [1 + \chi_e(\omega)] \mathbf{E}(\mathbf{r}, \omega) = \epsilon_0 \epsilon(\omega) \mathbf{E}(\mathbf{r}, \omega), \quad (2.5a)$$

$$\mathbf{B}(\mathbf{r}, \omega) = \mu_0 [1 + \chi_m(\omega)] \mathbf{H}(\mathbf{r}, \omega) = \mu_0 \mu(\omega) \mathbf{H}(\mathbf{r}, \omega). \quad (2.5b)$$

Here, we introduced the effective material parameters permittivity ϵ and permeability μ that describe the linear interaction of the electromagnetic fields with isotropic and homogeneous materials. By using these parameters, we avoid treating every single charge and the corresponding currents in the considered matter. In section 2.1.6, we give a simple microscopic model of dielectrics from which we will derive the effective material parameters. This model is based on an arrangement of simplified atoms consisting of a negatively charged electron and its corresponding atomic core being positively charged.

Equations (2.3a) - (2.5b) describe how an applied electric field \mathbf{E} interacts with the medium such that it induces electric dipoles or orients the already existent electric dipoles in the medium. As a consequence, the dielectric displacement \mathbf{D} is being modified. The magnetic field \mathbf{H} induces or orients magnetic dipoles that lead to modification of the magnetic induction \mathbf{B} . In general, also the possibility exists that an applied electric field leads to magnetic dipole moments and an applied magnetic field leads to electric dipole moments. Formally, this leads to cross-coupling terms in Eqs. (2.5a) and (2.5b). We refrain from a deeper treatment since this effect is barely existent in naturally occurring materials which are of interest

here. Nevertheless, it occurs in natural, so-called optically active materials and artificial metamaterials [19].

2.1.2 Wave equation

Maxwell's equations (2.1a) - (2.1d) can be rewritten such that we obtain the inhomogeneous wave equations for the electric and magnetic field [20]

$$\nabla \times \nabla \times \mathbf{E} + \mu_0 \epsilon_0 \frac{\partial^2 \mathbf{E}}{\partial t^2} = -\frac{\partial}{\partial t} \left(\mu_0 \mathbf{j} + \mu_0 \frac{\partial \mathbf{P}}{\partial t} + \nabla \times \mathbf{M} \right) \quad (2.6a)$$

$$\nabla \times \nabla \times \mathbf{H} + \mu_0 \epsilon_0 \frac{\partial^2 \mathbf{H}}{\partial t^2} = \nabla \times \mathbf{j} + \nabla \times \frac{\partial \mathbf{P}}{\partial t} + \frac{\partial \mathbf{M}}{\partial t}. \quad (2.6b)$$

The terms on the right hand side of both wave equations act as source terms. We can distinguish between two types of source terms of Eq. (2.6a): (i) the external source current density \mathbf{j} and (ii) $\frac{\partial}{\partial t} \mathbf{P}$ and $\nabla \times \mathbf{M}$ as polarization and magnetization current density, respectively. The latter describe the interaction of electromagnetic radiation with matter.

For homogeneous and isotropic media for which $\epsilon, \mu = \text{const.}$ without external currents and charges, the wave equation for the electric field can be written as

$$\nabla^2 \mathbf{E} + \mu_0 \mu \epsilon_0 \epsilon \frac{\partial^2 \mathbf{E}}{\partial t^2} = 0. \quad (2.7)$$

This means that the source terms of Eq. (2.6a) can be accounted for by the material parameters ϵ and μ . The wave equation (2.7) has solutions of the type

$$\mathbf{E}(\mathbf{r}, t) = \frac{1}{2} [\mathbf{E}_0 \exp(i\mathbf{k} \cdot \mathbf{r} - i\omega t) + cc.], \quad (2.8)$$

representing plane waves oscillating in time with frequency ω and propagating in the direction of the wave vector \mathbf{k} , $cc.$ denotes the complex conjugate. Inserting the plane wave solution into the wave equation (2.7) leads to the dispersion relation

$$\frac{\omega^2}{|\mathbf{k}|^2} = \frac{c_0^2}{\epsilon \mu}. \quad (2.9)$$

From the dispersion relation, we obtain the refractive index

$$n = \pm \sqrt{\epsilon \mu}. \quad (2.10)$$

The decision which sign of the refractive index we have to choose, can be easily deduced from the continuity conditions for the fields at interfaces (see section 2.1.4) when both permittivity and permeability are real numbers. If one or both are complex numbers, we can use a lengthy formula to deduce the sign of n for given complex values of ϵ and μ from Ref. [21]. Since natural materials do not exhibit a magnetic response in the optical domain ($\mu = 1$), we do not have to worry about the sign of the refractive index: for natural materials, we always choose the positive branch of Eq. (2.10) – this is different for metamaterials (see chapter 3).

2.1.3 Fourier transformation

Sometimes it is advantageous – for example for the solution of differential equations – to switch from the time domain to the frequency domain by applying the Fourier transformation to the electromagnetic fields. The Fourier transformation of a (scalar) function $f(t)$ expressed in the time domain to a function $f(\omega)$ expressed in the frequency domain then reads

$$f(\omega) = \frac{1}{\sqrt{2\pi}} \int_{-\infty}^{\infty} \exp(-i\omega t) f(t) dt. \quad (2.11)$$

The inverse operation is performed by

$$f(t) = \frac{1}{\sqrt{2\pi}} \int_{-\infty}^{\infty} \exp(i\omega t) f(\omega) d\omega. \quad (2.12)$$

The Fourier transformation is analogous for vectorial functions like the electric field.

In optics, Fourier transformations are widely used for the mathematical treatment since we often deal with monochromatic plane waves and these Fourier transformations are equivalent to a representation of time dependent electromagnetic fields as a linear combination of monochromatic plane waves. Thus, we can write the electric field of one frequency component as

$$\mathbf{E}(\mathbf{r}, t) = \mathbf{E}(\mathbf{r}, \omega) \exp(i\omega t). \quad (2.13)$$

In frequency space, we obtain for the homogeneous wave equation (2.7)

$$\nabla^2 \mathbf{E}(\mathbf{r}, \omega) - \frac{\omega^2}{c^2} \mathbf{E}(\mathbf{r}, \omega) = 0, \quad (2.14)$$

where we used the definition of the speed of light in media $c^2 = \frac{1}{\mu_0 \mu \epsilon_0 \epsilon}$.

We also perform the Fourier transformation when transforming a function $f(\mathbf{r})$ in real space to a function $f(\mathbf{k})$ in reciprocal space by

$$f(\mathbf{k}) = \frac{1}{(2\pi)^{3/2}} \int_{-\infty}^{\infty} \int_{-\infty}^{\infty} \int_{-\infty}^{\infty} \exp(-i\mathbf{k} \cdot \mathbf{r}) f(\mathbf{r}) d^3 r. \quad (2.15)$$

2.1.4 Transmittance, reflectance and absorption

We consider a plane wave incident onto an interface formed by two half spaces with $\mu_1 = 1$, ϵ_1 , n_1 and $\mu_2 = 1$, ϵ_2 and n_2 , respectively (see Fig. 2.1). The general case with μ_1 , ϵ_1 , n_1 , μ_2 , ϵ_2 and n_2 will be considered in section 3.5. One part of the wave is reflected and the other is transmitted into half space 2. The transmitted wave is refracted obeying Snell's law

$$\frac{\sin \theta_i}{\sin \theta_t} = \frac{n_2}{n_1}, \quad (2.16)$$

where both angles are defined in Fig. 2.1. For calculating the relative intensities that are transmitted and reflected, we decompose the incoming wave into an s - and a p -polarized

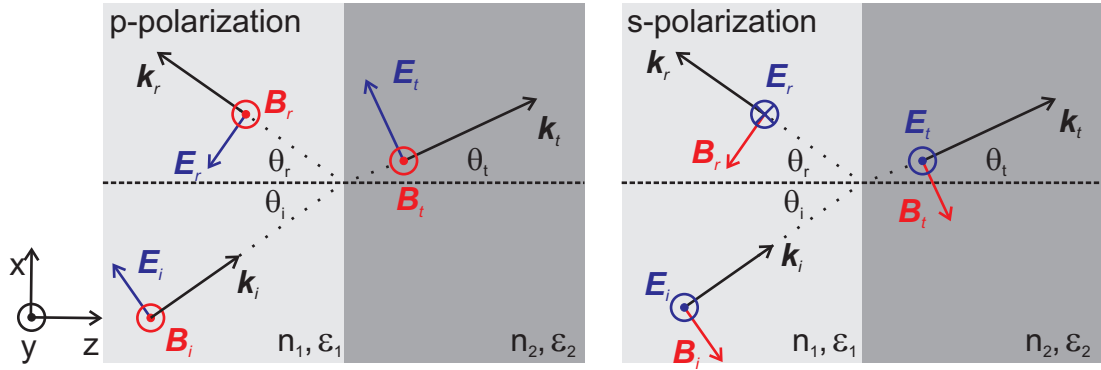


Figure 2.1: Reflection and transmittance of incident p - and s -polarized light at an interface of two half spaces of different permittivities.

part as illustrated in Fig. 2.1¹. These two contributions correspond to electric field vectors orthogonal (s -polarized) and parallel (p -polarized) with respect to the plane of incidence, which is defined by the wave vector \mathbf{k}_i of the incident wave and the normal vector of the interface. We aim for coefficients that relate the incident electric fields to the reflected and transmitted electric fields – the so-called Fresnel equations. The Fresnel equations result from the continuity relations at the interface for the \mathbf{E} - and \mathbf{D} -field components [2] when crossing an interface.:

- (i) The tangential component of \mathbf{E} and the normal component of \mathbf{D} are continuous.
- (ii) The normal component of \mathbf{E} and the tangential component of \mathbf{D} are discontinuous.

Additionally, the transverse components of the wave vector (here, k_x - and k_y -components) are conserved when the wave crosses the interface.

The transmittance and reflectance coefficients, t and r , respectively relate the incident and transmitted and the incident and reflected fields. They read [22]

$$r_s(k_x, k_y) = \frac{k_{z1} - k_{z2}}{k_{z1} + k_{z2}}, \quad r_p(k_x, k_y) = \frac{\epsilon_2 k_{z1} - \epsilon_1 k_{z2}}{\epsilon_2 k_{z1} + \epsilon_1 k_{z2}}, \quad (2.17a)$$

$$t_s(k_x, k_y) = \frac{2k_{z1}}{k_{z1} + k_{z2}}, \quad t_p(k_x, k_y) = \frac{2\epsilon_2 k_{z1}}{k_{z1} + k_{z2}} \sqrt{\frac{\epsilon_1}{\epsilon_2}}. \quad (2.17b)$$

The transmittance T and reflectance R are obtained by relating the corresponding intensities. Formally, the intensity I is defined as time average of the Poynting vector $\langle \mathbf{S} \rangle = \frac{1}{2} \text{Re}(\mathbf{E} \times \mathbf{H}^*)$ ². For plane waves, this leads to

$$|\langle \mathbf{S} \rangle| = \frac{1}{2} \sqrt{\frac{\epsilon_0 \epsilon}{\mu_0 \mu}} |\mathbf{E}|^2. \quad (2.18)$$

¹Here, the term “polarization” occurs for the second time. In the preceding section 2.1.1, polarization refers to the spatial average over all occurring electric dipole moments. In the context of plane waves it is a common term for the direction of the electric field vector with respect to a reference direction.

²In the following, we will name the time average of the Poynting vector $\langle \mathbf{S} \rangle$ just Poynting vector \mathbf{S} .

Thus, we obtain $T = \frac{n_2 \cos \theta_t}{n_1 \cos \theta_i} |t|^2$ and $R = |r|^2$.

For dispersive, that is, lossy media the refractive index becomes complex which in turn leads to a decrease in the amplitude – the wave amplitude decays and its energy is absorbed in the medium. The amount of energy absorbed is clearly a function of the propagation length within the lossy material. The proper quantity to describe the absorption is the so-called extinction constant γ that is defined by

$$I(z) = I_0 \exp(-\gamma z). \quad (2.19)$$

Here, the propagation direction is the z -direction, and I_0 is the intensity at a given point in time and space. Assuming a refractive index of $n = \text{Re}(n) + i \text{Im}(n)$, we obtain for the extinction constant

$$\gamma = \frac{4\pi \text{Im}(n)}{\lambda}. \quad (2.20)$$

2.1.5 Interaction of a plane wave with a single scatterer

In the following section, we give a short introduction to the concept of cross-sections of single scatterers. This concept is illustrated for the special case when the scatterer is a dipole.

When discussing the optical properties of single isolated scatterers, we have to keep in mind that we can not describe its optical properties by the usual material parameters ϵ and n or with quantities like transmittance, reflectance, and absorption. Instead, we introduce the physical quantities scattering, absorption, and extinction cross-section, C_{scat} , C_{abs} , and $C_{\text{ext}} = C_{\text{scat}} + C_{\text{abs}}$, respectively. The interpretation of these quantities becomes more familiar when considering the case of geometrical optics where the extinction cross-section is just the area of the shadow of an opaque object illuminated by a plane wave. Here, the first important property becomes evident: the extinction cross-section has the dimensions of an area.

In general, we discuss a situation as sketched in Fig. 2.2: an incident plane wave impinges onto a scatterer. *Via* its electric field \mathbf{E}_i , the plane wave induces a dipole moment (or higher order multipoles) that reradiates parts of the incoming power (accounted for by the scattering cross-section) and parts are absorbed (accounted for by the absorption cross-section). The energy the plane wave is carrying is given by its intensity. In the far field, that is, at the position of the detector, the scattered field \mathbf{E}_s and the incident field \mathbf{E}_i superimpose to the total field \mathbf{E}_{tot}

$$\mathbf{E}_{\text{tot}} = \mathbf{E}_i + \mathbf{E}_s. \quad (2.21)$$

The expression for the magnetic field is analogous. Without restrictions to generality, we assume that the incident wave is x -polarized: $\mathbf{E}_i = E_i \mathbf{u}_x$, where \mathbf{u}_x is the unit vector in x -direction. In the far field, the scattered wave is a spherical wave represented by its electric field vector at position r

$$\mathbf{E}_s = \frac{\exp(ikr)}{-ikr} \mathbf{X}(\theta, \varphi) E_i. \quad (2.22)$$

Here, we use the so-called vector-scattering amplitude $\mathbf{X}(\theta, \varphi)$ which defines both the scattering strength and the angular distribution of the scattered far field. The absolute value of

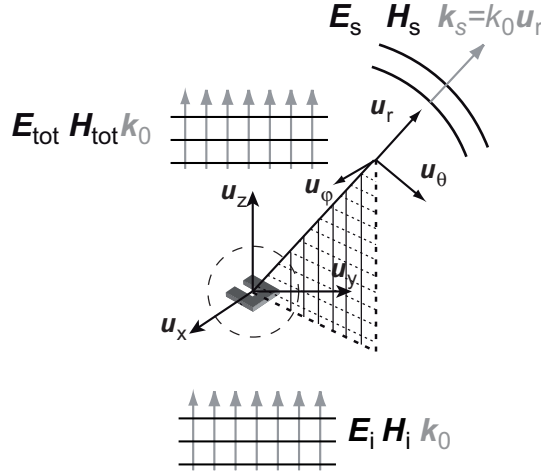


Figure 2.2: Geometry of the scattering problem: an incident electromagnetic wave (\mathbf{E}_i , \mathbf{H}_i , and $\mathbf{k}_0 = k_0 \mathbf{u}_z$) interacts with a particle. One part of the radiation is scattered and the rest is absorbed. The scattered field (\mathbf{E}_s , \mathbf{H}_s , and $\mathbf{k}_s = k_0 \mathbf{u}_r$) is radiated, in general, into all directions. In the far field, the scattered field is superimposed with the incident field to give the total field (\mathbf{E}_{tot} , \mathbf{H}_{tot} , and \mathbf{k}_0). The dashed circle illustrates a closed surface around the scatterer.

the wave vector is given by k . The power of the scattered wave is the power that leaves a closed surface around the scatterer, indicated as dashed circle around the scatterer in Fig. 2.2. The scattered power is given by

$$P_s = r^2 \int_{4\pi} \mathbf{S}_s \cdot \mathbf{u}_r d\Omega \quad (2.23)$$

$$= r^2 \int_{4\pi} \frac{1}{2} \text{Re} (\mathbf{E}_s \times \mathbf{H}_s^*) \cdot \mathbf{u}_r d\Omega. \quad (2.24)$$

With $\mathbf{H}_s = \frac{k}{\omega \mu_0 \mu} \mathbf{u}_r \times \mathbf{E}_s$ and with Eqs. (2.22) and (2.24), we obtain

$$P_s = \frac{|E_i|^2}{2\omega k \mu_0 \mu} \int_{4\pi} |\mathbf{X}|^2 d\Omega, \quad (2.25)$$

where Ω is the solid angle. The scattering cross-section is defined as the quotient of the power reradiated by the scatterer into the far field and the intensity $I_i = \frac{|E_i|^2}{2\omega \mu_0 \mu} k$ of the incident plane wave. Thus, the scattering cross-section reads

$$C_{\text{scat}} = \frac{1}{k^2} \int_{4\pi} |\mathbf{X}|^2 d\Omega. \quad (2.26)$$

Optical Theorem The extinction cross-section is usually calculated using the Optical Theorem [23]. We explicitly derive the Optical Theorem in appendix A.

In general, the extinction cross-section is given by the fraction of the extinguished power and the incident intensity. The extinguished power is the sum of the absorbed power and the scattered power; the scattered power is given by Eq. (2.23) and the absorbed power by

$$P_{\text{abs}} = -r^2 \int_{4\pi} \mathbf{S}_{\text{tot}} \cdot \mathbf{u}_r d\Omega, \quad (2.27)$$

with $\mathbf{S}_{\text{tot}} = \frac{1}{2}\text{Re}[(\mathbf{E}_s + \mathbf{E}_i) \times (\mathbf{H}_s^* + \mathbf{H}_i^*)]$. Thus, we obtain

$$P_{\text{ext}} = P_{\text{abs}} + P_s = r^2 \int_{4\pi} (-\mathbf{S}_{\text{tot}} \cdot \mathbf{u}_r + \mathbf{S}_s \cdot \mathbf{u}_r) d\Omega. \quad (2.28)$$

Following the Optical Theorem, we obtain as extinguished power

$$P_{\text{ext}} = I_i \frac{4\pi}{k^2} \text{Re}[\mathbf{u}_x \cdot \mathbf{X}(\theta = 0)]. \quad (2.29)$$

Hence, the extinction cross-section reads

$$C_{\text{ext}} = \frac{4\pi}{k^2} \text{Re}[\mathbf{u}_x \cdot \mathbf{X}(\theta = 0)]. \quad (2.30)$$

We learn from the Optical Theorem that the extinction cross-section is solely determined by the scattering in the forward direction although the principal equation (2.28) for calculating the extinguished power requires an integration over the entire solid angle.

For completeness, we note that the absorption cross-section is given by

$$C_{\text{abs}} = C_{\text{ext}} - C_{\text{scat}}. \quad (2.31)$$

2.1.6 Linear optical properties of dielectrics in the Lorentz model

The classical response of atoms to electromagnetic waves can be described in a driven oscillator model – the so-called Lorentz model [6, 24]. Here, the atom is modeled as an electron which is bound to the atom core. Applying an oscillating electric field leads to an oscillation of the electron around its rest position.

Damped harmonic oscillator

In linear optics, that is, for small incident electric field strengths, the atom can be described by a damped harmonic oscillator leading to the differential equation for the trajectory x of the electron

$$m_e \frac{\partial^2}{\partial t^2} x(t) + m_e \Gamma \frac{\partial}{\partial t} x(t) + m_e \omega_0^2 x(t) = -e E_0 \exp(-i\omega t), \quad (2.32)$$

where m_e is the electron mass, Γ describes the damping (it accounts for both radiation damping and non-radiative damping due to, for instance, the generation of heat), e is the electron charge and $E(t)$ is the applied electric field. We assume the incident plane wave to be polarized in x -direction: $\mathbf{E}(\mathbf{r}, t) = \mathbf{u}_x E_0 \exp[i(\mathbf{k} \cdot \mathbf{r} - \omega t)]$. Since the atom is much smaller than the wavelength of the plane wave, the electric field is constant across the atom. This allows us to neglect the position dependence of the electric field. The steady state solution of Eq. (2.32) reads $x(t) = a \exp(-i\omega t)$ leading to the electric dipole moment of a harmonic oscillator

$$p(t) = -ex(t) = \frac{e^2 E_0 / m_e}{\omega_0^2 - \omega^2 - i\Gamma\omega} \exp(-i\omega t). \quad (2.33)$$

Thus, the electric dipole moment is proportional to the electric field. The corresponding proportionality factor $\alpha(\omega)$ is called polarizability. It reads

$$\alpha(\omega) = \frac{e^2/m_e}{\omega_0^2 - \omega^2 - i\Gamma\omega}. \quad (2.34)$$

The radiated electric field in the far field is given by [2]

$$\mathbf{E}_s = Z_0 \frac{ck^2}{4\pi} \frac{\exp(ikr)}{r} p [(\mathbf{n} \times \mathbf{u}_x) \times \mathbf{n}], \quad (2.35)$$

where $Z_0 = \sqrt{\frac{\mu_0}{\epsilon_0}} = 377 \Omega$ is the vacuum impedance, k the wave vector, and \mathbf{n} is the unit vector pointing into the direction of interest. \mathbf{u}_x denotes the orientation of the electric dipole moment. We note that according to Eq. (2.35), no energy is radiated into the far field by an oscillating electric dipole along the direction of the corresponding dipole moment vector.

This classical electric dipole model leads to a contradiction. In order to clarify this contradiction, we assume that the dissipation Γ of the electronic oscillation is entirely given by radiation damping, thus, $\Gamma = \Gamma_{\text{rad}}$. In general, the damping Γ can be written as a sum of a radiative and a non-radiative contribution, Γ_{rad} and Γ_{nonrad} , respectively. This leads to $\Gamma = \Gamma_{\text{rad}} + \Gamma_{\text{nonrad}}$. If the radiation damping approaches zero ($\Gamma_{\text{rad}} \rightarrow 0$), we expect the dipole not to radiate. In fact, in resonance the electron displacement diverges. Thus, the dipole moment diverges as well leading to a diverging radiated electric field [see Eq. (2.35)]. That in turn contradicts the assumption that no energy is lost due to radiation. In electrodynamics, this contradiction can be partially resolved by introducing a reaction force leading to the so-called Abraham-Lorentz formula [20]. This reaction force accounts for the interaction of the dipole with its own radiation. Unfortunately, this contradiction needs a quantum mechanical treatment to be completely resolved [25]. Here, the limitations of classical electrodynamics become evident.

Dipole scattering

In the following, we discuss a single scatterer that can be described by the Lorentz model. For simplicity, we assume all losses of the dipole to be due to scattering. Clearly, for this case the extinction cross-section equals the scattering cross-section and the absorption cross-section vanishes. The far field distribution of the dipole is given by Eq. (2.35) where $p = \alpha E_i$ is the electric dipole moment with the scalar polarizability α . For the spherical wave defined by Eq. (2.35), the absolute value of the Poynting vector (it points in the \mathbf{u}_r -direction) reads

$$|\mathcal{S}_s| = Z_0 \frac{c^2 k^4}{32\pi^2} \frac{|\mathbf{p}|^2}{r^2} \sin^2 \theta. \quad (2.36)$$

θ is the angle between \mathbf{u}_r and the electric dipole moment vector \mathbf{p} . This leads to the scattering cross-section

$$C_{\text{scat}} = \frac{Z_0^2 c^2 k^4}{6\pi} |\alpha|^2, \quad (2.37)$$

which is depicted in Fig. 2.3. Note that Eq. (2.37) does not fulfill the Optical Theorem for the reasons given above.

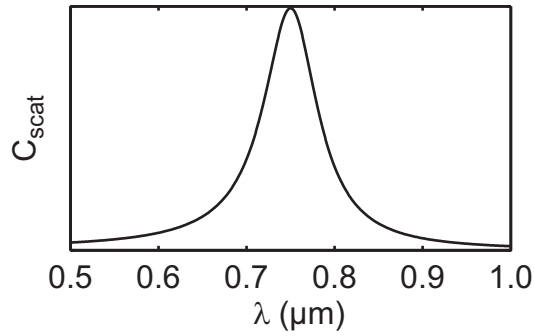


Figure 2.3: Scattering cross-section of an Lorentz oscillator described by Eq. (2.37). It nicely resembles a Lorentzian form. For modeling the dipole, we took $\omega_0 = 2\pi \times 400 \times 10^{12} \text{ s}^{-1}$, and $\Gamma = \frac{\omega_0}{10}$.

Permittivity from the Lorentz model

In Eq. (2.34), we obtained a microscopic polarizability of one isolated atom. Here, we sketch how the macroscopic permittivity ϵ of Eq. (2.5a) of a material composed of many (of these isolated) atoms is related to the microscopic polarizability α .

We consider a plane wave interacting with many atoms, each of which reradiates spherical waves of the form of Eq. (2.22). These reradiated spherical waves superimpose to a plane wave. Thus, we can define the macroscopic electric dipole moment as the spatial average over many microscopic dipole moments leading to³

$$P(\omega) = E(\omega) \left\langle \sum_{\nu} \alpha_{\nu}(\omega) \delta(\mathbf{r} - \mathbf{r}_{\nu}) \right\rangle. \quad (2.38)$$

Here, $\langle \dots \rangle$ denotes the spatial average, the index ν counts the atoms located at position r_{ν} having the polarizability $\alpha_{\nu}(\omega)$. If we consider only atoms of the same type with polarizability $\alpha(\omega)$, arranged with a constant density n_0 , we obtain

$$P(\omega) = n_0 \alpha(\omega) E(\omega) = \epsilon_0 \chi(\omega) E(\omega), \quad (2.39)$$

where $\chi(\omega) = \frac{n_0 \alpha(\omega)}{\epsilon_0}$ is the electric susceptibility.

2.1.7 Linear optical properties of metals

In the following section, we describe the linear optical properties of metals within the so-called Drude model [6, 26], which – like the Lorentz model for dielectrics – gives an intuitive understanding of the microscopic processes leading to the typical metallic response when interacting with light. In this discussion, we include surface modes on metal-dielectric interfaces – so-called surface plasmon polaritons and collective oscillations of the free-electron gas being confined to a small volume – the so-called particle plasmons.

³We neglect all modifications due to interaction between the atoms. This approximation holds true for diluted gases but breaks down when the atoms are densely packed such that the electronic wave functions overlap and form electronic bands. Nevertheless, even for this case we can define a new polarizability of the same form [see Eq. (2.34)] leading to a qualitatively good description of the linear optical properties of nonmetallic solids. This new polarizability has nothing to do with the polarizability of the constituting single atoms.

Linear optical properties of free-electron gases – the Drude model

In metals, the electrons of the conduction band can move almost freely through the crystal. Thus, the free electrons (approximately one per atom of the crystal) form a free-electron gas. The response of the free-electron gas to an applied electric field can be described similarly to the Lorentz model but with vanishing restoring force. Hence, the resonance frequency vanishes as well. Also the other electrons that are bound to the atoms contribute to the permittivity of the metal but in most frequency regions the response of the free-electron gas dominates.

The formal transition from the Lorentz model to the Drude model, that is, removing the restoring force from the electron equation of motion (2.32), leads to

$$m_e \frac{\partial^2 x(t)}{\partial t^2} + m_e \gamma \frac{\partial x(t)}{\partial t} = -eE(\omega) \exp(-i\omega t). \quad (2.40)$$

Along the lines of section 2.1.6, we obtain for the permittivity

$$\epsilon(\omega) = 1 - \frac{\omega_{\text{pl}}^2}{\omega^2 + i\gamma\omega}, \quad (2.41)$$

where we introduce the plasma frequency $\omega_{\text{pl}} = \sqrt{\frac{ne^2}{m_e \epsilon_0}}$, with n being the number density of free electrons. In order to account for the influence of the atomic cores, we introduce an empirical offset ϵ_∞ , leading to

$$\epsilon(\omega) = \epsilon_\infty - \frac{\omega_{\text{pl}}^2}{\omega^2 + i\gamma\omega}. \quad (2.42)$$

In Fig. 2.4, experimentally determined values from Ref. [27] of the real part and imaginary part of the permittivity of gold are plotted over frequency in comparison to the permittivity obtained from the Drude model [Eq. (2.42)] with the parameters $\omega_{\text{pl}} = 2\pi \times 2086 \times 10^{12} \text{ s}^{-1}$,

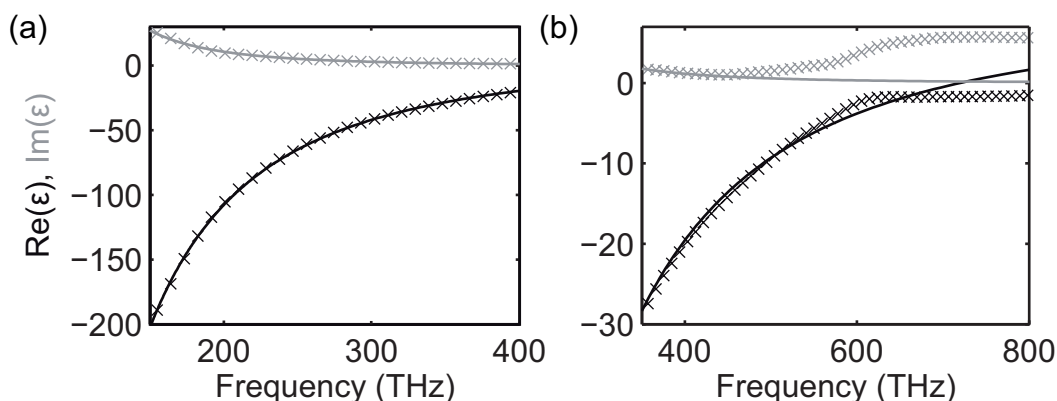


Figure 2.4: Imaginary (gray) and real (black) part of the permittivity of gold for two spectral regions: (a) 150-400 THz and (b) 350-800 THz. The crosses correspond to experimentally determined values of ϵ from Ref. [27] and the solid line to a fit of the experimental data to the Drude formula (2.42) (the crosses are obtained by interpolating the actually measured data with a cubic spline).

$\gamma = 2\pi \times 19 \times 10^{12} \text{ s}^{-1}$, and $\epsilon_\infty = 11$. The Drude model resembles the experimental values for frequencies below 550 THz (corresponding to wavelengths above 600 nm) very well. The deviations for frequencies above 550 THz (below 600 nm-wavelengths) are due to the excitation of electrons associated with lower lying bands into the conduction band – so-called interband transitions [28]⁴. These excitations can be modeled by a sum of Lorentz oscillators [see Eq. (2.39)]. The corresponding susceptibility is just added to the Drude permittivity giving

$$\epsilon(\omega) = \epsilon_\infty + \sum_{\nu} \frac{\omega_{L,\nu}^2}{\omega_{0,\nu}^2 - \omega^2 - i\Gamma_{\nu}\omega} - \frac{\omega_{\text{pl}}^2}{\omega^2 + i\gamma\omega}, \quad (2.43)$$

where we account for several Lorentz oscillators by the sum.

Since we are mainly interested in the spectral region in which interband transitions do not play a major role, we stick to Eq. (2.41) for the description of the permittivity of metals.

Surface plasmon polaritons

Interfaces of dielectric and metallic half spaces are known to support waves that travel along these interfaces – so-called surface plasmon polaritons (SPPs). In this section we sketch how to obtain the dispersion relation of SPPs.

In general, SPPs are eigenmodes of the system consisting of the two half spaces: the upper half space with $\epsilon_+ = 1$ being a dielectric (for simplicity, we choose vacuum) and the lower half space with $\epsilon_- = \epsilon(\omega)$ being a metal. The eigenmodes are solutions to the differential equation [20]

$$\nabla \times \nabla \times \mathbf{E}(\mathbf{r}, \omega) - \frac{\omega^2}{c_0^2} \epsilon(\mathbf{r}, \omega) \mathbf{E}(\mathbf{r}, \omega) = 0, \quad (2.44)$$

with $\epsilon(\mathbf{r}, \omega) = \epsilon(\omega)$ if $z < 0$ and $\epsilon(\mathbf{r}, \omega) = 1$ if $z > 0$. Surface plasmon polaritons are modes traveling along the surface of the metal. Thus, the only transverse electric field component is normal to the surface and they are evanescent in the z -direction. For an SPP traveling along the x -direction, the corresponding wave vector component is given by

$$k_x^2 = \frac{\epsilon(\omega)}{\epsilon(\omega) + 1} \frac{\omega^2}{c_0^2}, \quad (2.45)$$

which is the dispersion relation for SPPs [20]. It is plotted in Fig. 2.5. For the z -component of the wave vector in the lower half space, we obtain

$$k_z^2 = \frac{\epsilon(\omega)^2}{\epsilon(\omega) + 1} \frac{\omega^2}{c_0^2}, \quad (2.46)$$

and analogous in the upper half space

$$k_z^2 = \frac{1}{\epsilon(\omega) + 1} \frac{\omega^2}{c_0^2}. \quad (2.47)$$

⁴In gold, electrons from the $5d$ -band (valence band) are excited into the $6s$ -band (conduction band). The required energy is 2.38 eV (corresponding to 575 THz-frequency and 522 nm-wavelength, respectively).

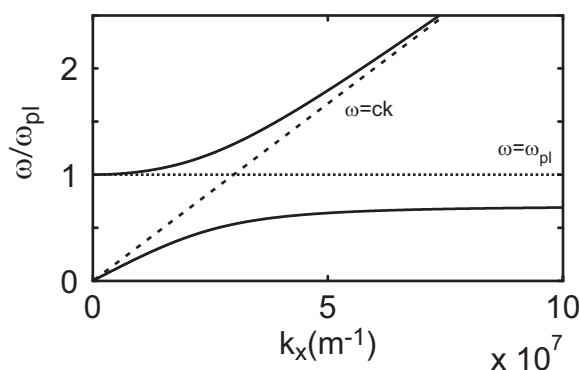


Figure 2.5: The solid lines represent the dispersion relation for a surface plasmon polariton traveling along a metal-vacuum interface. The dashed line is the light line, that is, the free-space dispersion of electromagnetic waves. The dotted line corresponds to the dispersion of the bulk plasmon.

Since we are aiming for waves that travel along the x -direction, we search for real values of k_x ⁵. Additionally, SPPs are confined in the xy -plane. Thus, in both half spaces, the z -component of the wave vector must be imaginary, that is, no energy is transported away from the surface. Both conditions (k_x is real and k_z is imaginary) are only fulfilled if [see Eqs. (2.45), (2.46), and (2.47)]

$$\begin{aligned}\epsilon(\omega) + 1 &< 0 \text{ and} \\ \epsilon(\omega) &< 0.\end{aligned}$$

In a broad spectral range, these conditions are only met if one half space is metallic and the other one is dielectric.

For a Drude metal with $\epsilon_\infty = 1$, $\omega_{\text{pl}} = 2\pi \times 2086 \times 10^{12} \text{ s}^{-1}$, and $\gamma = 0$, we obtain the SPP dispersion relation shown in Fig. 2.5 as solid line. The dashed line is the free-space dispersion $\omega = ck$ of electromagnetic waves and the dotted horizontal line corresponds to the bulk plasmon which is the collective longitudinal oscillation of the conduction band electrons relative to the atomic cores. The physical origin of the large deviation of the dispersion relations of the free-space electromagnetic wave and the bulk plasmon and the dispersion relation of the SPP lies in the strong coupling between the electromagnetic field of the photon and the induced charges of the metal. The effect is also called anti-crossing.

The dispersion relation of the SPP consists of two branches. The lower one approaches a horizontal line for $\omega = \omega_{\text{pl}}/\sqrt{2}$. It is below the free space dispersion (represented by the dashed line) for all frequencies, that is, SPPs do not couple to propagating modes. *Vice versa* electromagnetic waves from free-space can not excite SPPs due to the wave vector mismatch. Thus, tricks have to be applied for exciting SPPs by plane electromagnetic waves:

- (i) SPPs can be launched by using an attenuated total internal reflection geometry in the so-called Otto [30] and Kretschmann configurations [31].

⁵We restrict this discussion to real values of $\epsilon(\omega)$. Thus, the wave vector becomes either imaginary or real. For complex values of $\epsilon(\omega)$, the wave vector becomes complex as well, leading to damped propagation. We refer to Ref. [29].

- (ii) A grating is fabricated on the metal surface. This grating transfers quasi momentum *via* a reciprocal lattice vector to the photon in order to correct for the momentum mismatch between SPPs and photons [32].

Additionally, SPPs can be efficiently excited by electrons passing through the metal [33]. Here, we do not have to deal with the momentum mismatch between photons and SPPs. Figure 2.5 also illustrates that the frequency of the SPP's lower branch is limited whereas the wave vector $k_x = 2\pi/\lambda$ is not limited. Thus, the wavelength can approach – in principle – arbitrarily small values. In real metals, however, these modes are damped and will die out after a very short propagation length due to the large number of oscillations within the propagation length [29].

The upper branch of the dispersion relation of SPPs lies above the light line. Thus, these excitations radiate, *i.e.*, in this region ($\omega > \omega_{pl}$), the metal behaves like an ordinary dielectric. Similar to SPPs being electromagnetic excitations confined to the two-dimensional (2D) metal surface, there are also eigenmodes of metallic wires [20] corresponding to excitation that are confined in one dimension.

Particle plasmons

In this section, we will shortly sketch the properties of so-called particle plasmons, collective excitations of the free-electron gas being confined to a volume of – in principle – arbitrary shape. These shapes include spheres, ellipsoids [34], cubes [35], shells [36, 37], and the fundamental building blocks of metamaterials like split-ring resonators [38, 39].

First, we consider the so-called quasi-static regime, that is, particle plasmons that are confined to volumes with dimensions much smaller than the considered vacuum wavelength.

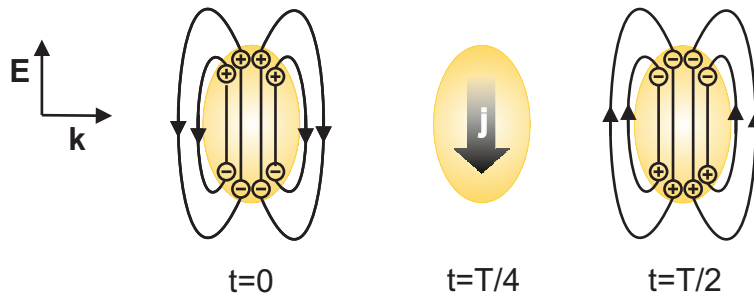


Figure 2.6: Illustration of a particle plasmon excited by an oscillating external electric field.

In a first approximation, the metallic particle can be viewed as an antenna in which the incident electric field \mathbf{E}_0 induces a dipole moment. The dipole moment leads to a restoring force that in turn leads to a current. The entire system starts to oscillate and behaves analogous to the Lorentz oscillator of section 2.1.6. For a sphere, we obtain the polarizability α that reads [34]

$$\alpha = 4\pi\epsilon_0 R^3 \frac{\epsilon - \epsilon_m}{\epsilon + 2\epsilon_m}, \quad (2.48)$$

where R is the radius of the sphere, ϵ_m denotes the permittivity of the surrounding medium and ϵ the permittivity of the material the sphere consists of. The corresponding dipole moment is given by $p = \epsilon_m \alpha E_0$. For real valued ϵ , the polarizability has a maximum where the absolute value of the denominator $|\epsilon + 2\epsilon_m|$ becomes minimal. This is the condition for the existence of particle plasmons.

Within the quasi-static approximation, we can also deal with ellipsoidal particles with the principal axes a , b , and c . In this formalism, the principal axes of the ellipsoids are represented by the normalized geometry parameters L_i , with $i = 1, 2$, and 3 , and $\sum_i L_i = 1$. Clearly, we obtain a tensorial polarizability leading to a vectorial equation for the polarization

$$\begin{pmatrix} p_x \\ p_y \\ p_z \end{pmatrix} = \epsilon_m \begin{pmatrix} \alpha_1 & 0 & 0 \\ 0 & \alpha_2 & 0 \\ 0 & 0 & \alpha_3 \end{pmatrix} \begin{pmatrix} E_{0,x} \\ E_{0,y} \\ E_{0,z} \end{pmatrix}. \quad (2.49)$$

Here, we assumed that the principal axes of the ellipsoidal particle are aligned along the unit vectors of the Cartesian coordinate system. For the elements of the polarization tensor, we obtain

$$\alpha_i = \epsilon_0 \frac{\epsilon - \epsilon_m}{\epsilon_m + (\epsilon - \epsilon_m)L_i} V_{\text{ellipsoid}}. \quad (2.50)$$

From Eq. (2.50), we learn that the resonance frequency depends on the exact geometry of the ellipsoid, *i.e.*, on L_i . For instance, when we assume incident x -polarized light ($E_{0,y} = E_{0,z} = 0$) on an ellipsoidal metallic particle, the resonance frequency is increased when increasing L_y and L_z . In contrast, the resonance frequency is decreased when L_x is increased (the sum $L_x + L_y + L_z$ is always one).

We now aim for a general expression for the optical properties of particles of spherical shape. This can be done analytically within the so-called Mie theory [40]. However, for particles of arbitrary shape rigorous numerical calculations are required.

The Mie formalism requires a lengthy calculation that is not presented here but can be found in Ref. [23]. There, Maxwell's equations are solved in spherical coordinates for an incident plane wave and a sphere of radius R with permittivity ϵ embedded in a surrounding medium with permittivity ϵ_m .

Instead of the polarizability, we use scattering, absorption, and extinction cross-sections that provide an adequate description of the optical properties of a sphere of arbitrary size. In this context, also possible multipole excitations are taken into account. The Mie theory gives the extinction cross-section as multipole expansion [23]

$$C_{\text{ext}} = \frac{2\pi}{k^2} \sum_{L=1}^{\infty} (2L+1) \text{Re}(a_L + b_L). \quad (2.51)$$

The corresponding scattering cross-section reads

$$C_{\text{scat}} = \frac{2\pi}{k^2} \sum_{L=1}^{\infty} (2L+1) (|a_L|^2 + |b_L|^2). \quad (2.52)$$

The absorption cross-section results from Eq. (2.31). In Eqs. (2.51) and (2.52), L denotes the order of the multipole expansion ($L = 1$: electric and magnetic dipole moment, $L = 2$:

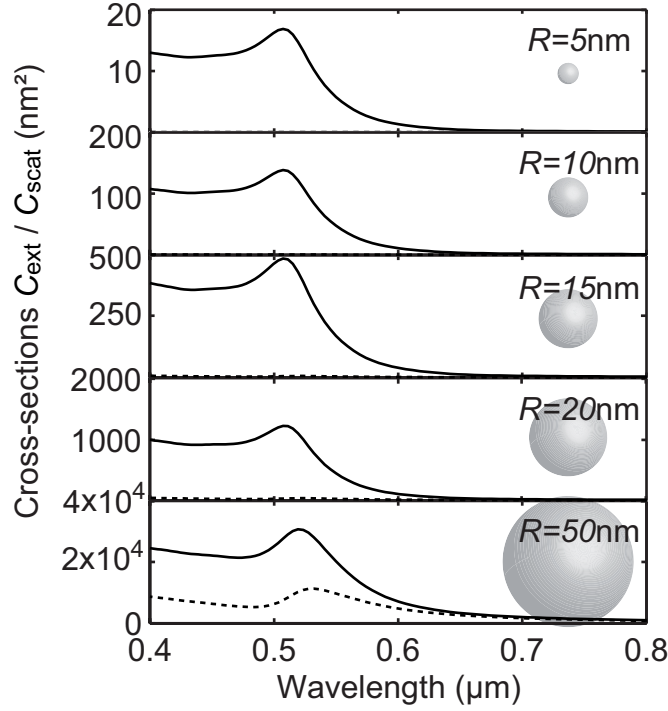


Figure 2.7: Extinction- (solid curves) and scattering-cross-section (dashed curves) spectra for gold sphere of different radii (5, 10, 15, 20, and 50 nm). The surrounding medium is air ($n=1$). For $R < 20$ nm, the scattering cross-section almost vanishes. Thus, absorption dominates the response of small spherical gold particles. When calculating the extinction and scattering cross-section, we took the experimental values for the permittivity of gold from Ref. [27]. The cross-section spectra are calculated numerically based on Appendix A of Ref. [23].

electric and magnetic quadrupole moment, . . .). For the expansion coefficients a_L and b_L , we obtain

$$a_L = \frac{m\psi_L(mx)\psi'_L(x) - \psi'_L(mx)\psi_L(x)}{m\psi_L(mx)\eta'_L(x) - \psi'_L(mx)\eta_L(x)} \quad \text{and} \quad b_L = \frac{\psi_L(mx)\psi'_L(x) - m\psi'_L(mx)\psi_L(x)}{\psi_L(mx)\eta'_L(x) - m\psi'_L(mx)\eta_L(x)}, \quad (2.53)$$

respectively. Here, $m = n/n_m$ is the quotient of the complex index of refraction of the sphere's material and the index of refraction of the surrounding material. The so-called size parameter is given by $x = kR$ (k is the free-space wave vector) and finally ψ_L and η_L denote the Riccati-Bessel cylindrical functions [41].

Figure 2.7 illustrates the extinction- and scattering-cross-section spectra for gold spheres of different radii. We observe a resonance for all radii at around $0.51 \mu\text{m}$ -wavelength. The maximum of the absolute value for the extinction cross-section equals 18 nm^2 for spheres of 5 nm radius corresponding to $C_{\text{ext, max}} \approx (1/4)\pi R^2$. For spheres of 50 nm radius we obtain 3000 nm^2 corresponding to $C_{\text{ext, max}} \approx 4\pi R^2$. Furthermore, the spectra show that for small spheres the scattering cross-section almost vanishes. Hence, for small particles absorption dominates the response. The limit of small particles is equivalent to the dipole approximation: we assume $x \ll 1$ and truncate the sum of Eq. (2.51) at $L = 1$. This leads to

$$C_{\text{ext}} = 12\pi \frac{\omega}{c} \epsilon_m^{3/2} R^3 \frac{\text{Im}(\epsilon)}{(\text{Re}(\epsilon) + 2\epsilon_m)^2 + \text{Im}(\epsilon)^2}. \quad (2.54)$$

We note, in the limit of small particles, the scattering cross-section vanishes as we see in Fig. 2.7. This changes for larger particles: scattering becomes more and more important due to the growing electric dipole moment.

2.2 Nonlinear optics

With the advent of the laser [1], a new field of optics became accessible in which electromagnetic fields can interact with each other *via* excitations of a medium. This is fundamentally different from the field of linear optics: here, we always assume that fields can be linearly superimposed. The interaction of two, three or more waves leads to interesting phenomena like the generation of new frequencies [42]. These phenomena can often be formally described by introducing a nonlinear polarization \mathbf{P}_{NL} [43–45]. Thus, in nonlinear optics, the polarization reads [43]

$$\mathbf{P} = \underbrace{\epsilon_0 \chi_e^{(1)} \mathbf{E}}_{\mathbf{P}_L} + \underbrace{\epsilon_0 \chi_e^{(2)} : \mathbf{E}\mathbf{E} + \epsilon_0 \chi_e^{(3)} : \mathbf{E}\mathbf{E}\mathbf{E} + \dots}_{\mathbf{P}_{\text{NL}}}, \quad (2.55)$$

with the nonlinear susceptibilities $\chi_e^{(2),(3),\dots}$ being tensors of third, fourth, ... rank. They are complex quantities relating the complex amplitudes of the electric fields with the nonlinear polarization \mathbf{P}_{NL} . The colon denotes the product of $\chi_e^{(2),(3),\dots}$ with the electric fields and the linear susceptibility $\chi_e^{(1)}$ accounts for the linear interaction of the fields with the medium. The series in Eq. (2.55) has to converge. Thus, we must have

$$\chi_e^{(1)} \mathbf{E} \gg \chi_e^{(2)} : \mathbf{E}\mathbf{E} \gg \chi_e^{(3)} : \mathbf{E}\mathbf{E}\mathbf{E}. \quad (2.56)$$

This regime is often referred to as the regime of perturbative nonlinear optics [44]. As already indicated in Eq. (2.55), the polarization can be split into a linear and a nonlinear contribution, \mathbf{P}_L and \mathbf{P}_{NL} , respectively. Putting the sum of linear and nonlinear polarization into Maxwell's equations (2.1a) - (2.1d) leads to a source term in the wave equation (2.6a). Now, the nonlinear wave equation reads [44]

$$\nabla^2 \mathbf{E}(\mathbf{r}, t) + \mu_0 \epsilon_0 \epsilon \frac{\partial^2 \mathbf{E}(\mathbf{r}, t)}{\partial t^2} = -\mu_0 \frac{\partial^2 \mathbf{P}_{\text{NL}}(\mathbf{r}, t)}{\partial t^2}. \quad (2.57)$$

2.2.1 Second-order nonlinear optical effects

In this section, we terminate the series in Eq. (2.55) after the second order. The resulting nonlinear polarization leads to the second-order nonlinear effects of optical rectification (OR), second-harmonic generation (SHG), sum-frequency generation (SFG), and difference frequency generation (DFG).

In the following, we discuss the interaction of two electric fields oscillating with frequencies ω_n and ω_m , respectively. We assume the simple case in which the second-order nonlinearity

$\chi^{(2)}$ is a scalar quantity⁶. The termination of the nonlinear polarization after the second order leads to

$$\mathbf{P}^{(2)}(\omega_n + \omega_m) = \epsilon_0 \sum_{n,m} \chi^{(2)}(\omega_n + \omega_m, \omega_n, \omega_m) E(\omega_n) E(\omega_m). \quad (2.58)$$

If the two frequencies happen to be the same ($\omega_n = \omega_m = \omega$), we obtain two contributions to the nonlinear polarization: (i) $\mathbf{P}^{(2)}(2\omega)$ oscillating with twice the fundamental frequency leading to SHG, (ii) $\mathbf{P}^{(2)}(0)$ leading to a dc-contribution, the so-called optical rectification. If the two frequencies are different, we obtain DFG with the nonlinear source term $\mathbf{P}^{(2)}(|\omega_n - \omega_m|)$ oscillating at $|\omega_n - \omega_m|$ and SFG with the nonlinear source term $\mathbf{P}^{(2)}(\omega_n + \omega_m)$ oscillating at $\omega_n + \omega_m$.

Symmetry considerations As we are used to in physics, also the second-order nonlinear effects are subject to symmetry of the underlying physical system. The symmetry of the second-order nonlinear susceptibility $\chi_{ijk}^{(2)}$ represents the symmetry of the crystal for which it describes the nonlinear effects. Especially important for this thesis is the impact of inversion symmetry on $\chi_{ijk}^{(2)}$. If a system is inversion symmetric every physical vectorial quantity changes its sign if the operation $\mathbf{r} \rightarrow -\mathbf{r}$ (here, \mathbf{r} denotes a position in real space) is executed. This means that both the second-order nonlinear polarization $\mathbf{P}^{(2)}$ and the electric field \mathbf{E} have to change signs – this leads to a contradiction in Eq. (2.58). This contradiction can only be resolved by setting $\chi_{ijk}^{(2)} = 0$. Thus, there are no second-order nonlinear optical effects in systems with inversion symmetry. Consequently, the leading order is the third order.

2.2.2 Third-order nonlinear optical effects

We restrict the discussion of third-order nonlinear optical effects to third harmonic generation (THG). The others like four wave mixing, the optical Kerr effect or two-photon absorption [44] although being very interesting are not discussed here.

In general, the THG nonlinear susceptibility $\chi_{ijkl}^{(3)}(3\omega, \omega, \omega, \omega)$ has 81 entries. Again, we consider only the simplest case for which the THG nonlinear susceptibility becomes a scalar. Thus, we obtain as THG nonlinear polarization

$$\mathbf{P}^{(3)}(3\omega, \omega, \omega, \omega) = \epsilon_0 \chi^{(3)}(3\omega, \omega, \omega, \omega) E(\omega) E(\omega) E(\omega). \quad (2.59)$$

This is the source of an electromagnetic wave oscillating at 3ω . In contrast to the second-order nonlinear susceptibility, the third-order nonlinear susceptibility does not vanish for inversion symmetric systems.

2.2.3 Damped anharmonic oscillator

As the Lorentz model allows for a qualitative understanding of linear optical properties of dielectrics, we try to expand this model such that it also describes the nonlinear optical

⁶In general, it is a complex third rank tensor with 27 entries. These entries are subject to the symmetry of the crystalline structure and – in the low-frequency limit – subject to Kleinman's symmetry [44].

properties. For this purpose, we add a second-order nonlinearity in the restoring force leading to the equation of motion of the electron (2.32)

$$m_e \frac{\partial^2}{\partial t^2} x(t) + m_e \Gamma \frac{\partial}{\partial t} x(t) + \underbrace{m_e \omega_0^2 x(t) + m_e a x(t)^2}_{\text{nonlinear restoring force}} = -eE(t). \quad (2.60)$$

Here, the restoring force is a quadratic function of the displacement requiring a potential which is a cubic function of the displacement. Thus, the system is not centrosymmetric and allows for second-order nonlinearities.

For calculating the second-order nonlinear susceptibility, we assume two incident plane waves $E(t) = \frac{1}{2} [E_1 \exp(-i\omega_1 t) + E_2 \exp(-i\omega_2 t) + cc.]$. The equation of motion (2.60) is usually solved by a perturbation ansatz [44,45] which is only valid if $\omega_0^2 x(t) \gg a x(t)^2$. In order to distinguish between the different orders of perturbation, we introduce an expansion parameter λ leading to

$$\frac{\partial^2}{\partial t^2} x(t) + \Gamma \frac{\partial}{\partial t} x(t) + \omega_0^2 x(t) + a x(t)^2 = -\lambda \frac{e}{m_e} E(t). \quad (2.61)$$

This equation of motion is solved by the ansatz $x(t) = \lambda x^{(1)}(t) + \lambda^2 x^{(2)}(t) + \lambda^3 x^{(3)}(t) + \dots$. Thus, we obtain terms proportional to $\lambda, \lambda^2, \dots$. Each term of the ansatz must satisfy the equation in order that the ansatz is a solution to Eq. (2.60). This leads to a set of equations sorted by powers of the expansion parameter λ

$$\propto \lambda : \quad \frac{\partial^2}{\partial t^2} x^{(1)}(t) + \Gamma \frac{\partial}{\partial t} x^{(1)}(t) + \omega_0^2 x^{(1)}(t) = -\frac{e}{m_e} E(t), \quad (2.62)$$

$$\propto \lambda^2 : \quad \frac{\partial^2}{\partial t^2} x^{(2)}(t) + \Gamma \frac{\partial}{\partial t} x^{(2)}(t) + \omega_0^2 x^{(2)}(t) + a x^{(1)}(t)^2 = 0, \quad (2.63)$$

⋮

The solution of Eq. (2.62) is analogous to that of the linear damped harmonic oscillator: $x^{(1)}(t) = \frac{1}{2} [x^{(1)}(\omega_1) \exp(-i\omega_1 t) + x^{(1)}(\omega_2) \exp(-i\omega_2 t) + cc.]$, with $x^{(1)}(\omega_j) = -\frac{e/m_e}{D(\omega_j)}$. Here, $D(\omega_j)$ is defined like for the harmonic oscillator $D(\omega_j) = \omega_0^2 - \omega_j^2 - i\omega_j \Gamma$. This solution leads to a quadratic inhomogeneity in Eq. (2.63). The resulting χ^2 -processes are: (i) second harmonic generation ($2\omega_1$ and $2\omega_2$) (ii) sum frequency generation [$(\omega_1 + \omega_2)$], (iii) difference frequency generation [$(\omega_1 - \omega_2)$], and (iv) optical rectification (0).

Here, we are mainly interested in SHG. Consequently, we consider only the component oscillating with $2\omega_1$. The corresponding equation of motion reads

$$\frac{\partial^2}{\partial t^2} x^{(2)}(t) + \Gamma \frac{\partial}{\partial t} x^{(2)}(t) + \omega_0^2 x^{(2)}(t) + a \frac{e^2}{m_e^2 D(\omega_1)^2} E(\omega_1)^2 \exp(-i2\omega_1 t) = 0. \quad (2.64)$$

The steady state solution is again of the type

$$x^{(2)}(t) = x^{(2)}(2\omega_1) \exp(-i2\omega_1 t), \quad (2.65)$$

with

$$x^{(2)}(2\omega_1) = -a \frac{e^2 E(\omega_1)^2}{m_e^2 D(\omega_1)^2 D(2\omega_1)}. \quad (2.66)$$

Similarly to the procedure in the preceding section, the microscopic nonlinear electric dipole moment is deduced from the microscopic nonlinear displacement. After performing the spatial average, we obtain the macroscopic nonlinear polarization describing SHG

$$P^{(2)}(2\omega_1, \omega_1, \omega_1) = \frac{n_0 a e^3}{m_e^2 D(\omega_1)^2 D(2\omega_1)} E(\omega_1)^2. \quad (2.67)$$

This leads via $P^{(2)}(2\omega_1, \omega_1, \omega_1) = \epsilon_0 \chi^{(2)}(2\omega_1, \omega_1, \omega_1) E(\omega_1)^2$ to the SHG susceptibility

$$\chi^{(2)}(2\omega_1, \omega_1, \omega_1) = \frac{n_0 a e^3}{\epsilon_0 m_e^2 D(\omega_1)^2 D(2\omega_1)}. \quad (2.68)$$

2.2.4 Metals in the hydro-dynamic approach

For the description of the nonlinear optical properties of metals, we extend the Drude model and describe the free-electron gas as a fluid. This treatment intrinsically leads to nonlinear effects of arbitrary order similar to nonlinearities in hydro-dynamics [46]. The approach is based on the work of the groups of J. V. Moloney and S. W. Koch in Tucson and Marburg, respectively [47].

The nonlinear optical properties of metals can be described by assuming the free-electron gas to behave like a fluid. To do so, we have to leave the single electron picture in which each electron is described by its trajectory and velocity. We rather describe the optical properties of the free-electron gas by a number density $n_e(\mathbf{r}, t)$ and a velocity field $\mathbf{v}(\mathbf{r}, t)$. The positively charged background formed by the ions of the metal is accounted for by a time-independent number density n_0 . For the charge density ρ and the current density $\mathbf{j}(\mathbf{r}, t)$, we find

$$\rho(\mathbf{r}, t) = e[n_0 - n_e(\mathbf{r}, t)] \quad (2.69)$$

and

$$\mathbf{j}(\mathbf{r}, t) = -en_e(\mathbf{r}, t)\mathbf{v}(\mathbf{r}, t) = [\rho(\mathbf{r}, t) - en_0]\mathbf{v}(\mathbf{r}, t), \quad (2.70)$$

respectively. An applied electromagnetic field leads to a Lorentz force density that changes the velocity field of the electron fluid.

Similarly to the previous section 2.2.3, we search for a source term that generates the nonlinear effects. Here, the source is the current density field $\mathbf{j}(\mathbf{r}, t)$ induced by the external electric field. Precisely, on the right-hand side of Eq. (2.6a), we have the derivative of the current density with respect to time. Thus, we search for an expression of $\frac{\partial}{\partial t}\mathbf{j}(\mathbf{r}, t)$. For this purpose, we use the continuity equation [Eq. (2.2)] and we rewrite the total differential

$$\begin{aligned} d\mathbf{j} &= \frac{\partial}{\partial t}\mathbf{j}dt + \frac{\partial}{\partial x}\mathbf{j}dx + \frac{\partial}{\partial y}\mathbf{j}dy + \frac{\partial}{\partial z}\mathbf{j}dz \\ &= \left[\frac{\partial}{\partial t} + (\mathbf{v} \cdot \nabla) \right] \mathbf{j}dt. \end{aligned}$$

The operator $(\frac{\partial}{\partial t} + \mathbf{v} \cdot \nabla)$ is also known as *convective derivative* [46]. It considers the explicit time dependence $\frac{\partial}{\partial t}$ of the current density field and by the scalar operator $\mathbf{v} \cdot \nabla$, it accounts for the spatial variation of the quantity considered (here, the current density field) because of the fluid's motion. Finally, we obtain

$$\begin{aligned}
\frac{\partial \mathbf{j}(\mathbf{r}, t)}{\partial t} &= \frac{d\mathbf{j}}{dt} - (\mathbf{v} \cdot \nabla)\mathbf{j} \\
&= -en_e \frac{d\mathbf{v}}{dt} - \mathbf{v}e \frac{dn_e}{dt} + e\mathbf{v}(\mathbf{v} \cdot \nabla)n_e + en_e(\mathbf{v} \cdot \nabla)\mathbf{v} \\
&= -en_e \frac{d\mathbf{v}}{dt} - e\mathbf{v} \left(\frac{\partial n_e}{\partial t} + (\mathbf{v} \cdot \nabla)n_e \right) + e\mathbf{v}(\mathbf{v} \cdot \nabla)n_e + (\mathbf{j} \cdot \nabla)\mathbf{v} \\
&= -e \underbrace{n_e \frac{d\mathbf{v}}{dt}}_{\text{force density}} + \underbrace{\mathbf{v}(\nabla \cdot \mathbf{j}) - (\mathbf{j} \cdot \nabla)\mathbf{v}}_{=+\sum_l \frac{\partial}{\partial r_l} \frac{\mathbf{j}j_l}{\rho - en_0}} \\
&= -e\mathbf{f} + \sum_l \frac{\partial}{\partial r_l} \frac{\mathbf{j}j_l}{\rho - en_0}. \tag{2.71}
\end{aligned}$$

The force density is based on the Lorentz force. Thus, we find

$$\mathbf{f} = \frac{1}{m_e} [(\rho - en_0)\mathbf{E} + \mathbf{j} \times \mathbf{B}]. \tag{2.72}$$

After inserting in Eq. (2.71), we obtain

$$\frac{\partial}{\partial t}\mathbf{j} = \frac{e^2 n_0}{m_e} \mathbf{E} - \gamma \mathbf{j} - \frac{e}{m_e} (\rho \mathbf{E} + \mathbf{j} \times \mathbf{B}) + \sum_k \frac{\partial}{\partial r_k} \left(\frac{\mathbf{j}j_k}{en_0 - \rho} \right). \tag{2.73}$$

Here, $\gamma \mathbf{j}$ is a phenomenological term describing the losses. The first two terms in Eq. (2.73) describe the linear response of the metal to an applied electric field. The last two terms describe nonlinearities to arbitrary order. In this model, all material properties of the metal are described by ρ and \mathbf{j} . Thus, we have $\mathbf{D} = \epsilon_0 \mathbf{E}$ and $\mathbf{B} = \mu_0 \mathbf{H}$.

Perturbative nonlinear optics of the hydro-dynamic model

Along the lines of the nonlinear optics section 2.2, we expand the fields \mathbf{E} , \mathbf{B} , and \mathbf{j} in a power series

$$\mathbf{E}(\mathbf{r}, t) = \sum_l \mathbf{E}^{(l)}(\mathbf{r}, t), \tag{2.74}$$

$$\mathbf{H}(\mathbf{r}, t) = \sum_l \mathbf{H}^{(l)}(\mathbf{r}, t), \tag{2.75}$$

$$\mathbf{j}(\mathbf{r}, t) = \sum_l \mathbf{j}^{(l)}(\mathbf{r}, t). \tag{2.76}$$

Here, the summation index l denotes the order of nonlinearity. When we separate the different orders, we have to keep in mind that the product of two quantities of the order l and k is

of the order $l + k$. Combining these expanded fields and Eq. (2.73) with Eq. (2.57) gives the well-known equations, which we also get from the linear Drude model of metals

$$\nabla \times \mathbf{E}^{(1)}(\mathbf{r}, t) = -\frac{\partial \mathbf{B}^{(1)}(\mathbf{r}, t)}{\partial t}, \quad (2.77)$$

$$\nabla \times \mathbf{B}^{(1)}(\mathbf{r}, t) = \frac{1}{\epsilon_0} \mathbf{j}^{(1)}(\mathbf{r}, t) + \frac{1}{c^2} \frac{\partial \mathbf{E}^{(1)}(\mathbf{r}, t)}{\partial t}, \quad (2.78)$$

$$\frac{\partial}{\partial t} \mathbf{j}^{(1)} = \frac{e^2 n_0}{m_e} \mathbf{E}^{(1)} - \gamma \mathbf{j}^{(1)}. \quad (2.79)$$

The second-order nonlinear fields read

$$\nabla \times \mathbf{E}^{(2)}(\mathbf{r}, t) = -\frac{\partial \mathbf{B}^{(2)}(\mathbf{r}, t)}{\partial t}, \quad (2.80)$$

$$\nabla \times \mathbf{B}^{(2)}(\mathbf{r}, t) = \frac{1}{\epsilon_0} \mathbf{j}^{(2)}(\mathbf{r}, t) + \frac{1}{c^2} \frac{\partial \mathbf{E}^{(2)}(\mathbf{r}, t)}{\partial t}, \quad (2.81)$$

$$\frac{\partial}{\partial t} \mathbf{j}^{(2)} = \frac{e^2 n_0}{m_e} \mathbf{E}^{(2)} - \gamma \mathbf{j}^{(2)} + \Psi^{(2)}. \quad (2.82)$$

Here, we introduced

$$\Psi^{(2)} = \sum_k \frac{\partial}{\partial r_k} \left(\frac{\mathbf{j}^{(1)} j_k^{(1)}}{e n_0} \right) - \frac{e}{m_e} \left[\epsilon_0 (\nabla \cdot \mathbf{E}^{(1)}) \mathbf{E}^{(1)} + \mathbf{j}^{(1)} \times \mathbf{B}^{(1)} \right] \quad (2.83)$$

as the second-order nonlinear source term. The other terms describe the linear interaction of the generated nonlinear field with the metal.

The second-order nonlinearity source term, Eq. (2.83), has three different contributions that stem from either the metal volume or the surface of the metal, or both: (i) the term $\nabla \cdot \mathbf{E}^{(1)} \mathbf{E}^{(1)}$ has only nonzero contributions on the surface of the metal. (ii) In contrast, the only nonzero contributions of the term $\mathbf{j}^{(1)} \times \mathbf{B}^{(1)}$ stems from the volume of the metal. (iii) The term $\sum_k \frac{\partial}{\partial r_k} \left(\frac{\mathbf{j}^{(1)} j_k^{(1)}}{e n_0} \right)$ has contributions from both the metal volume and the surface. This term originates from using a continuum formulation of the free-electron gas instead of the usual single-electron picture.

Within the numerical treatment of the groups of J. V. Moloney and S. W. Koch, it is possible to find out which contribution dominates by a switch-on switch-off analysis of the aforementioned terms (see section 6.1).

2.3 The electromagnetic local density of states

In this section, we briefly introduce a new quantity – the electromagnetic local density of states (LDOS). We start the explanation by means of Fermi's Golden Rule describing the spontaneous decay rate of an excited two-level atom [20]. Then, we rewrite the LDOS in terms of the eigenmodes of the system.

The spontaneous decay rate γ of a two-level atom is related to the electromagnetic LDOS

ρ_p : the more electromagnetic states are available in the vicinity of the atom, the higher is the decay rate. In particular, this becomes evident in Photonic Crystals where no states are present in the photonic band gap. Thus, the spontaneous decay rate of an atom vanishes [48]. Usually, the decay rate is described by Fermi's Golden Rule [20]

$$\gamma = \frac{2\pi}{\hbar^2} \sum_f |\langle f | \hat{H}_I | i \rangle|^2 \delta(\omega_i - \omega_f), \quad (2.84)$$

where \hbar is the reduced Planck's constant, $|f\rangle$ denotes the ground state of the atom, $|i\rangle$ the excited state of the atom, and $\delta(\omega_i - \omega_f)$ is Dirac's delta function. \hat{H}_I is the interaction Hamiltonian describing the interaction of an electric field \mathbf{E} with an electric dipole moment \mathbf{p} in the electric dipole approximation. Thus, \hat{H}_I is just the product of the operator describing the electric dipole moment $\hat{\mathbf{p}}$ and the operator describing the electric field $\hat{\mathbf{E}}$. Explicitly, the interaction Hamiltonian reads

$$\hat{H}_I = -\hat{\mathbf{p}} \cdot \hat{\mathbf{E}}. \quad (2.85)$$

In terms of the LDOS, Fermi's Golden Rule can be written as [20]

$$\gamma = \frac{\pi\omega}{3\hbar\epsilon_0} |\mathbf{p}|^2 \rho_p(\mathbf{r}_0, \omega_0). \quad (2.86)$$

The LDOS can be expanded in the eigenmodes of the system under consideration leading to [20]

$$\rho_p(\mathbf{r}_0, \omega_0) = 3 \sum_{\mathbf{k}} [\mathbf{u}_p \cdot (\mathbf{n}_k \mathbf{n}_k^*) \cdot \mathbf{u}_p] \delta(\omega_k - \omega_0), \quad (2.87)$$

with \mathbf{u}_p being the unit vector in the direction of the dipole moment and \mathbf{n}_k denoting the electromagnetic eigenmodes or normal modes of the system the two-level atom is placed in. The eigenmodes at the position \mathbf{r}_0 are characterized by their wave vector \mathbf{k} and their frequency ω_k . They have to fulfill the eigenmode equation

$$\nabla \times \nabla \times \mathbf{n}_k(\mathbf{r}_0, \omega_k) - \frac{\omega_k^2}{c^2} \mathbf{n}_k(\mathbf{r}_0, \omega_k) = 0. \quad (2.88)$$

This equation can be solved by an approach based on dyadic Green's functions $\bar{\bar{G}}(\mathbf{r}, \mathbf{r}', \omega)$ which is defined by

$$\nabla \times \nabla \times \bar{\bar{G}}(\mathbf{r}, \mathbf{r}', \omega) - \frac{\omega^2}{c^2} \bar{\bar{G}}(\mathbf{r}, \mathbf{r}', \omega) = \bar{\bar{I}} \delta(\mathbf{r} - \mathbf{r}'), \quad (2.89)$$

where $\bar{\bar{I}}$ denotes the unit dyad. The dyadic Green's function is expanded in the eigenmodes with vectorial expansion parameters \mathbf{A}_k leading to $\bar{\bar{G}} = \sum_{\mathbf{k}} \mathbf{A}_k \mathbf{u}_k$. Using that the eigenmodes form a complete set of equations, we obtain for the dyadic Green's function [22]

$$\bar{\bar{G}}(\mathbf{r}, \mathbf{r}', \omega) = \sum_{\mathbf{k}} c^2 \frac{\mathbf{n}_k^*(\mathbf{r}', \omega_k) \mathbf{n}_k(\mathbf{r}, \omega_k)}{\omega_k^2 - \omega^2}. \quad (2.90)$$

By the mathematical identity

$$\lim_{\eta \rightarrow 0} \text{Im} \left[\frac{1}{\omega_k^2 - (\omega + i\eta)^2} \right] = \frac{\pi}{2\omega_k} [\delta(\omega - \omega_k) - \delta(\omega + \omega_k)], \quad (2.91)$$

we find

$$\text{Im} \left[\bar{\bar{G}}(\mathbf{r}, \mathbf{r}', \omega) \right] = \frac{\pi c^2}{2\omega} \sum_{\mathbf{k}} \mathbf{n}_{\mathbf{k}}^*(\mathbf{r}', \omega_{\mathbf{k}}) \mathbf{n}_{\mathbf{k}}(\mathbf{r}, \omega_{\mathbf{k}}) \delta(\omega - \omega_{\mathbf{k}}). \quad (2.92)$$

This result allows us to rewrite the LDOS [Eq. (2.87)] in terms of the dyadic Green's function

$$\rho_{\mathbf{p}}(\mathbf{r}_0, \omega_0) = \frac{6\omega_0}{\pi c^2} \left[\mathbf{u}_{\mathbf{p}} \cdot \text{Im} \left[\bar{\bar{G}}(\mathbf{r}_0, \mathbf{r}_0, \omega_0) \right] \cdot \mathbf{u}_{\mathbf{p}} \right]. \quad (2.93)$$

We can interpret the dependence of the decay rate on its environment: the excited atom is modeled by a dipole moment inducing an electric field distribution to its environment that in turn acts back on the dipole. This back action does not only influence the decay rate that is connected to the width of the resonance by the energy-time uncertainty relation but it can also shift the energy of the resonance.

2.4 Electron-energy-loss spectroscopy on photonic systems

In this section, we discuss the theoretical foundations of electron-energy-loss-spectroscopy (EELS) experiments where a fast electron passes through a photonic system which can be, for example, a plasmonic particle or a metamaterial. It turns out that the measured quantity, namely the energy-loss probability is related to the electromagnetic LDOS.

When passing through the system, each electron with velocity \mathbf{v} can excite one mode of the system that is associated with the frequency ω . The energy of the excitation $\hbar\omega$ is delivered from the kinetic energy of the electron. Thus, after passing through the system, the kinetic energy of the electron is altered. At the end, we measure the change in energy of each electron leading to a electron-energy-loss spectrum [49]. The measured quantity is the probability, that the electron excites a mode with energy $\hbar\omega$.

For the theoretical treatment of the interaction of an electron with a photonic system, we make the following assumptions:

- (i) The energy loss of the electron is caused by the induced electromagnetic fields represented by \mathbf{E}_{ind} exerting a force \mathbf{F} on the electron. This is similar to the previous section where a dipole induces electric fields in its environment and these fields act back on the dipole. Here, the induced electric fields act back on the electron causing the energy loss [50–53].
- (ii) We consider only single scattering processes.
- (iii) In the experiment, we use a scanning-transmission-electron microscope, that focuses the electron beam down to areas of a few Ångströms in diameter. Thus, we model the current generated by the electron as a Dirac delta function.
- (iv) The kinetic energy of the electron is much larger than the energy of the excited mode. Indeed, the initial kinetic energy is usually 100 keV and the expected energy loss is on the order of 1 eV, that is, the energy of a plasmonic excitation leading to a relative energy loss of 1×10^{-5} . In other words, the velocity of the electron is constant.

The presented approach goes back to R. H. Ritchie [50] and was adopted by the work of J. G. de Abajo and M. Kociak [53] who connected the electron-energy-loss probability to the optical properties of the investigated system. We start from the Lorentz force experienced by the electron. It reads

$$\mathbf{F} = -e\mathbf{E}_{\text{ind}}. \quad (2.94)$$

We neglected the magnetic part of the Lorentz force because it does not contribute to the energy loss. Equation (2.94) leads directly to the energy W the electron loses when passing through the medium by integrating the force the electron feels along its path

$$W = \int_{z=-\infty}^{\infty} \mathbf{F} \cdot d\mathbf{r}. \quad (2.95)$$

The integration boundaries represent the trajectory of the considered electron. Inserting the force from Eq. (2.94) and substituting $d\mathbf{r} = \frac{d\mathbf{r}}{dt}dt = \mathbf{v}dt$, we find

$$W = \int_{t=-\infty}^{\infty} -e\mathbf{v} \cdot \mathbf{E}_{\text{ind}}(\mathbf{r}_e, t)dt. \quad (2.96)$$

Since we assume single scattering processes, the considered electron loses the energy quantum $\hbar\omega$ once and then it is analyzed by the detector. Equation (2.96) gives the energy loss an electron experiences on average. To obtain the loss probability density, we express W as an integral of a loss probability density $\Gamma(\omega)$ over the entire frequency space, where each frequency is weighted with its energy $\hbar\omega$. Thus, we obtain

$$W = \int_{\omega=0}^{\infty} d\omega \hbar\omega \Gamma(\omega). \quad (2.97)$$

In this picture, W can be interpreted as the expectation value of the energy loss of the electrons. Comparing with Eq. (2.96), we recognize that we have to switch to Fourier space, that is, we have to Fourier transform the induced electric field (see section 2.1.3). We finally find

$$\Gamma(\omega) = \frac{e}{\pi\hbar\omega} \int_{t=-\infty}^{\infty} dt \text{Re}[e^{-i\omega t} \mathbf{v} \cdot \mathbf{E}_{\text{ind}}(\mathbf{r}_e(t), \omega)]. \quad (2.98)$$

Now, we model the fast moving electron by a current density

$$\mathbf{j}(\mathbf{r}, t) = e\mathbf{v}\delta[\mathbf{r} - \mathbf{r}_e(t)]. \quad (2.99)$$

Here, $\mathbf{r}_e(t)$ is the trajectory, \mathbf{v} is the velocity and e the elementary charge of the fast moving electron. For an electron moving in the z -direction (along \mathbf{u}_z), we obtain

$$\begin{aligned} \mathbf{j}(\mathbf{R}, z, t) &= e\mathbf{v}\mathbf{u}_z\delta(\mathbf{R} - \mathbf{R}_0)\delta[z - z(t)] \\ &= e\mathbf{u}_z\delta(\mathbf{R} - \mathbf{R}_0)\delta(z/v - t). \end{aligned} \quad (2.100)$$

Here, \mathbf{R} is a position vector in the plane perpendicular to the z -direction and \mathbf{R}_0 the actual position of the electron in the xy -plane. The current density in the frequency domain reads

$$\mathbf{j}(\mathbf{r}, \omega) = e\mathbf{u}_z e^{i\omega z/v} \delta(\mathbf{R} - \mathbf{R}_0). \quad (2.101)$$

The interaction of the electron with the surrounding medium leads *via* the induced electric field to the energy loss of the electron. Thus, we have to find the induced electric field $\mathbf{E}_{\text{ind}}(\mathbf{r}_e, \omega)$ of Eq. (2.98). By the geometrical constraints and the current, we can compute a particular solution of the electric field with the help of dyadic Green's functions $\bar{\bar{G}}(\mathbf{r}, \mathbf{r}', \omega)$ (see Refs. [20, 53]), namely,

$$\mathbf{E}_{\text{ind}}(\mathbf{r}, \omega) = i\omega\mu_0 \int_V d\mathbf{r}'^3 \bar{\bar{G}}(\mathbf{r}, \mathbf{r}', \omega) \mathbf{j}(\mathbf{r}', \omega). \quad (2.102)$$

This leads to the electron-energy-loss-probability density

$$\Gamma(\mathbf{R}_0, \omega) = \frac{e^2\mu_0}{\pi\hbar} \int_{t=-\infty}^{\infty} \int_{t'=-\infty}^{\infty} dt dt' \text{Im} \left[e^{-i\omega(t-t')} \mathbf{u}_z \cdot \bar{\bar{G}}(\mathbf{R}_0, z(t), \mathbf{R}_0, z(t'), \omega) \cdot \mathbf{u}_z \right]. \quad (2.103)$$

The integral describes the Fourier transform of the dyadic Green's function with respect to z and z' . Equations (2.103) and Eq. (2.90) allow us to calculate the energy-loss probability from numerical simulations providing the eigenmodes of the system.

After performing the Fourier transform, we find

$$\Gamma(\omega) = \frac{e^2\mu_0}{\hbar} \text{Im} \left[\mathbf{u}_z \cdot \bar{\bar{G}}(\mathbf{R}_0, q, \mathbf{R}_0, -q, \omega) \cdot \mathbf{u}_z \right]. \quad (2.104)$$

Here, $q = \omega/v$ is the wave number of the electron and $\bar{\bar{G}}(\mathbf{R}_0, q, \mathbf{R}_0, -q, \omega)$ is the Fourier transformed dyadic Green's function. When inserting Eq. (2.93) into Eq. (2.104), we obtain the connection between the electromagnetic LDOS and the electron-energy-loss probability

$$\Gamma(\omega) = \pi \frac{e^2}{6\hbar\epsilon_0\omega} \rho(\mathbf{R}_0, q, \omega). \quad (2.105)$$

The energy-loss-probability density Γ of electrons passing through photonic systems depends on the LDOS ρ and hence on the eigenmodes of the system [see Eqs. (2.90) and (2.93)]. The exact interpretation of the relation between the LDOS and the energy-loss-probability density is currently under controversial discussion [53, 54].

2.5 Gaussian beams

In optical experiments, we often use Gaussian beams that can be described within the so-called paraxial approximation [20], that is, the divergence angle of the beam is small. Here, the transverse intensity profile of a Gaussian beam of an overall power P in cylindrical coordinates is given by

$$I(r, z) = \frac{P}{\pi w(z)^2/2} \exp\left(-\frac{2\rho^2}{w(z)^2}\right), \quad (2.106)$$

where $w(z)$ denotes the beam radius – the length scale on which the intensity drops to $1/e^2$ of the maximum value. Clearly, the beam axis is located at $\rho = 0$. Figures 2.8(a) and (b)

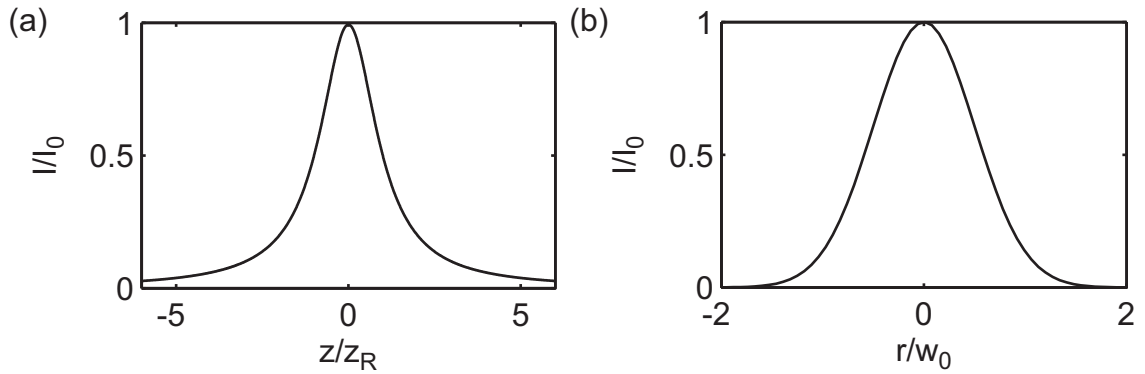


Figure 2.8: (a) Relative intensity (that is, $I(\rho, z)/I(\rho = 0, z = 0) = I/I_0$) of a Gaussian beam along the beam axis, *i.e.*, at $\rho = 0$. (b) Relative intensity as a function of the radial coordinate ρ in the focus, *i.e.*, at $z = 0$.

illustrate the intensity distribution of a Gaussian beam along the beam axis and in the focus (at $z = 0$), respectively. For the beam radius, see Fig. 2.9(a), we obtain

$$\begin{aligned} w(z) &= w_0 \sqrt{1 + \left(\frac{\lambda z}{\pi w_0^2}\right)^2} \\ &= w_0 \sqrt{1 + \left(\frac{z}{z_R}\right)^2}, \end{aligned} \quad (2.107)$$

where we introduced the Rayleigh length $z_R = \frac{\pi w_0^2}{\lambda}$, which measures the divergence of the beam. Precisely, it is the distance from the focus for which $w(z) = \sqrt{2}w_0$. Alternatively, the divergence of the beam is given by the divergence angle $\theta \approx \lambda/(\pi w_0)$ as illustrated in Fig. 2.9(a). Here, we can also define a numerical aperture of the Gaussian beam (in vacuum)

$$\text{NA}_B = \sin \theta. \quad (2.108)$$

The electric field amplitude of a Gaussian beam reads [55]

$$E(r, z) = E_0 \frac{w_0}{w(z)} \exp\left(-\frac{\rho^2}{w(z)^2}\right) \exp\left[i\left(kz - \varphi_G + \frac{k\rho^2}{2R(z)}\right)\right]. \quad (2.109)$$

Here, we introduced the curvature radius of the wave fronts $R(z) = z[1 + (z_R/z)^2]$ and the Gouy phase $\varphi_G = \arctan(z/z_R)$ which is sketched in Fig. 2.9. The impact of the Gouy phase is illustrated in Fig. 2.10 (a) and (b) where the phase fronts of a Gaussian beam (dashed red lines) are compared to the phase fronts of a plane wave (dashed blue lines). The Gouy phase becomes visible through the relative shift of the phase fronts. We note that the curvature radius becomes infinite in the focus (at $z = 0$), *i.e.*, in the focus the wavefronts are equivalent to those of a plane wave. In contrast, in the far field region, that is, for $z \gg z_R$, the curvature radius becomes z , *i.e.*, the wavefronts are equivalent to those of a spherical wave originating from $z = 0$.

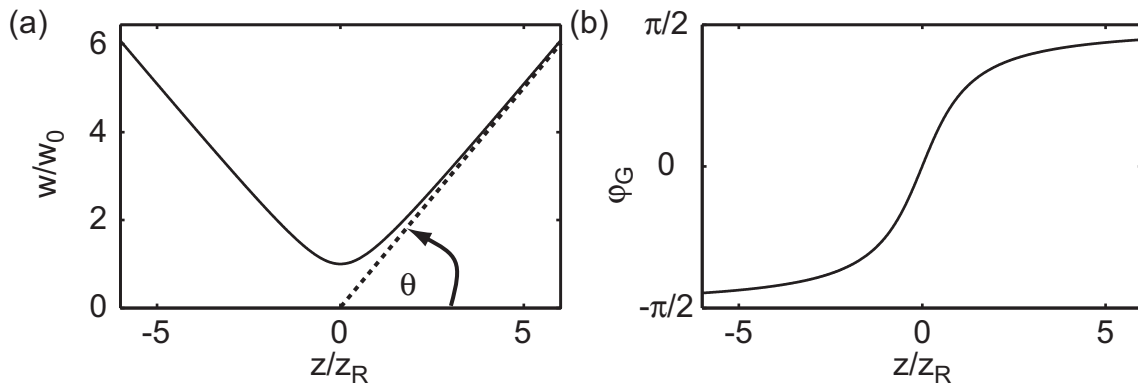


Figure 2.9: The width $w(z)$ (a) and the Gouy phase $\varphi(z)$ of the Gaussian beam along the beam axis. θ is the divergence angle of the beam.

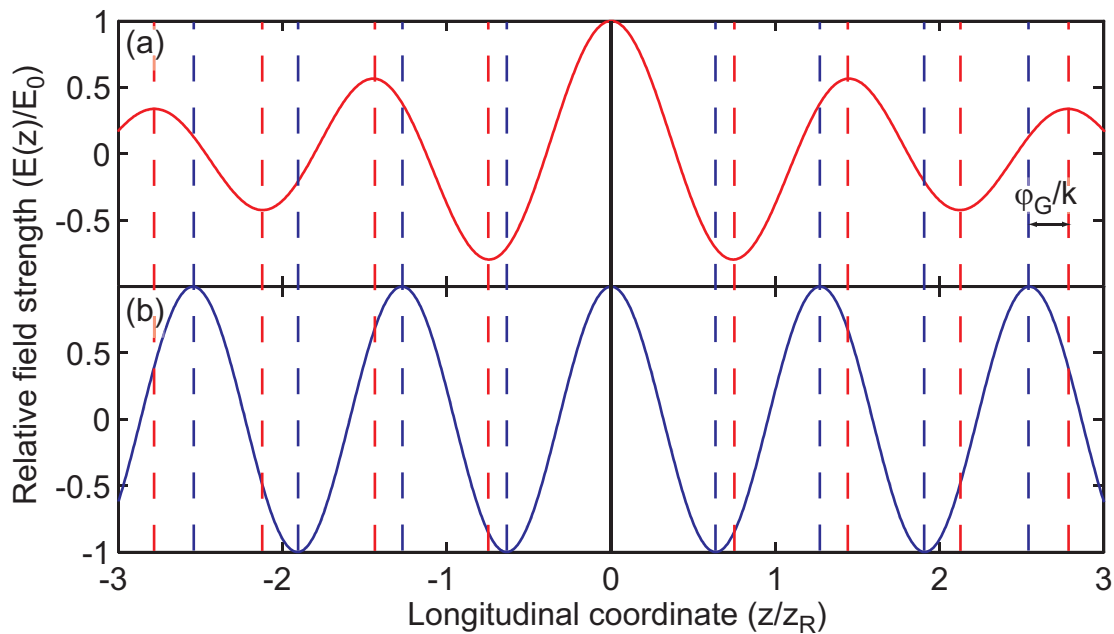


Figure 2.10: Illustration of the Gouy phase of a Gaussian beam. (a) depicts the peak electric field of a Gaussian beam along the optical axis, (b) the electric field of a plane wave with the same wavelength. The dashed lines correspond to the wave fronts of a Gaussian beam (red) and a plane wave (blue).

Chapter 3

The metamaterial concept

Photonic metamaterials are artificial composite materials with outstanding optical properties which rely on the fundamental building blocks metamaterials consist of. In contrast to natural materials, the fundamental building blocks of photonic metamaterials are not real atoms but artificial atoms, that is, artificial metallic nanostructures, which we also call photonic atoms. Since the overall size of each photonic atom is smaller than the relevant wavelength of the light, we can describe the metamaterial's optical properties by the effective material parameters permittivity ϵ , permeability μ , refractive index n , and impedance Z . They are obtained analogously to the usual homogenization procedure leading to the macroscopic Maxwell equations (see chapter 2.1 and Ref. [2]).

In this manner, photonic metamaterials pave the way for tailoring the optical properties to obtain exceptional dispersion relations. In particular, we point out that metamaterials allow for adjusting the permeability at optical frequencies corresponding to magnetic dipoles oscillating at optical frequencies – a property that does not occur in natural materials. Thus, materials for which the permeability is different from one can show astonishing optical effects not known from ordinary materials. For instance, when both ϵ and μ are simultaneously negative, the refractive index is negative as well¹. The negative refractive index has a number of physical implications including refraction to the “wrong” side of the surface normal, opposing wave and Poynting vector, reverse Cerenkov radiation² [3], and extraordinary imaging properties of planar lenses made of negative index materials [5, 58].

In this chapter, we address how to obtain effective material parameters from composite materials consisting of electric and magnetic atoms by the effective-medium theory. Here, electric and magnetic atoms provide the electric and magnetic response, respectively. By properly designing electric and magnetic atoms, we can tailor the corresponding material parameters, ϵ and μ . Since nature provides materials with a large range of possible values of ϵ , we focus on tailoring μ by magnetic atoms. Finally, we present some of the fascinating effects offered by metamaterials.

¹There are also alternative ways to achieve a negative refractive index, for example in media with strong dispersion in ϵ and μ [56], or in bi-anisotropic [19] and chiral media [57].

²These effects may also occur in common optical media as a result of strong dispersion.

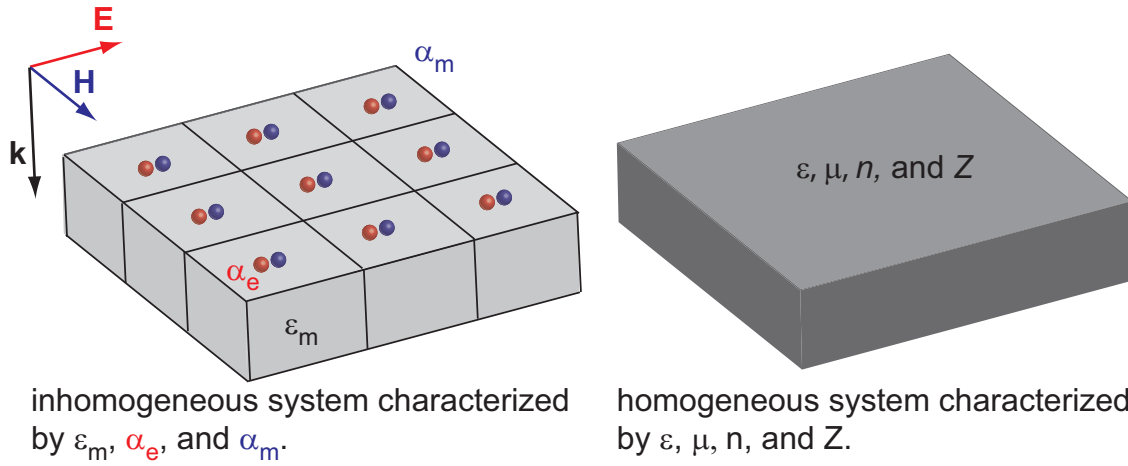


Figure 3.1: (a) An inhomogeneous metamaterial consisting of magnetic (blue) and electric (red) artificial atoms generating a magnetizability α_m and an electric polarizability α_e , respectively. The permittivity of the host material is ϵ_m . (b) Equivalently, the optical properties of the metamaterial can be described by the effective medium parameters ϵ , μ , n , and Z resulting from an averaging procedure of the electric and magnetic dipole moments.

3.1 Effective-medium theory

In this section, we discuss a composite material as illustrated in Fig. 3.1 consisting of periodically arranged electric and magnetic atoms causing the electric and magnetic response, respectively. We assume that these photonic atoms are arranged with a lattice constant a which is small enough that the dipole approximation can be applied, *i.e.*, $ka \ll 1$, where k is the absolute value of the wave vector of the light. For simplicity, the spacing between the photonic atoms is large enough that there is no electromagnetic interaction between them allowing us to assume that the optical properties of the atoms are not altered by the presence of their neighbors. Figure 3.1 (a) shows an inhomogeneous metamaterial as a periodic arrangement of electric (red) and magnetic (blue) atoms generating the electric and magnetic response, respectively. The response is described by an electric polarizability α_e and a magnetizability α_m . If the lattice constant is much smaller than the relevant wavelength of the light, the *inhomogeneous* system may be formally replaced by a *homogeneous* (effective) medium with the material parameters ϵ , μ , n , and Z . Here, $Z = Z_0 \sqrt{\frac{\mu}{\epsilon}}$ is the so-called impedance.

For a number density of n_0 identical electric atoms per unit volume, the polarization becomes (see section 2.1.6)

$$P = n_0 \alpha_e E = \epsilon_0 \chi_e E. \quad (3.1)$$

From this relation, we find for the permittivity

$$\epsilon = 1 + \chi_e = 1 + \frac{n_0}{\epsilon_0} \alpha_e. \quad (3.2)$$

The magnetization caused by a number density of n_0 magnetic atoms per unit volume is treated in an analogous way

$$M = n_0 \alpha_m H = \mu_0 \chi_m H. \quad (3.3)$$

And thus,

$$\mu = 1 + \chi_m = 1 + \frac{n_0}{\mu_0} \alpha_m. \quad (3.4)$$

Here, χ_m is the magnetic susceptibility. We note that the effective-medium theory allows to describe inhomogeneous materials by material parameters ϵ , μ , n , and Z giving a more intuitive understanding of the macroscopic optical properties, like transmittance, reflectance, absorption or refraction. For more general effective-medium theories, we refer to Ref. [34] and references therein.

3.2 Diluted metal

In this section, we discuss how diluted metals allow for tailoring the electric response. The permittivity of a metal is given by Eq. (2.41). Here, the only contribution which depends on the material properties is the plasma frequency $\omega_{\text{pl}} = \sqrt{\frac{n e^2}{m_e \epsilon_0}}$, where n is the density of electrons in the free-electron gas (see section 2.1.7). The density can be changed by diluting the metal, *i.e.*, by introducing dielectric inclusions. Most commonly used are metallic cylinders in air [59, 60] or stripes on glass substrates [39, 61, 62].

For metallic cylinders of radius r arranged in a square lattice with a period a , the plasma frequency becomes [59]

$$\omega_{\text{pl}} = \sqrt{\frac{n_{\text{eff}} e^2}{m_{e,\text{eff}} \epsilon_0}}, \quad (3.5)$$

where $m_{e,\text{eff}} = \frac{\mu_0}{2\pi} a^2 e^2 n_{\text{eff}} \ln(a/r)$ is the new effective mass of the electrons and $n_{\text{eff}} = n \frac{\pi r^2}{a^2}$ is the effective electron density. The effective mass of the electrons is altered by the self inductance of the wires. Thus, we can shift the effective plasma frequency from the ultra-violet spectral region to spectral regions of much larger wavelengths. This provides a tool for obtaining a large range of negative values of the permittivity.

We note that metallic cylinders or stripes can only be described as diluted metals if the electric field is oriented along the stripes. For the perpendicular polarization, we obtain plasmonic resonances in the corresponding spectral range [63, 64].

3.3 Split-ring resonator as magnetic atom

In this section, we will introduce the split-ring resonator (SRR), which is *the* prototypical magnetic atom. Its name goes back to Hardy and Whitehead [65]. Basically, an SRR is a metallic ring with one slit. In its original form (first applied to change the permeability at elevated frequencies), it is a horse-shoe-shaped metallic structure [4]. An external electromagnetic wave can excite a resonantly oscillating ring current leading to an oscillating magnetic dipole moment. Its resonance frequency strongly depends on the dimensions of the SRR but saturates for frequencies approaching the plasma frequency of the metal used [66, 67].

First, we describe the optical properties of SRRs by viewing them as metallic structures

supporting plasmonic resonances similar to those in metallic spheres and ellipsoids (see section 2.1.7). One of these resonances – the so-called magnetic resonance – leads to the oscillating ring current generating the desired magnetic dipole moment. In an intuitive model, we treat the SRR as a coil with one winding connected to a plate capacitor forming a resonant LC -circuit. Since, to excite the magnetic resonance, we need the proper orientation of magnetic and electric field of the exciting plane wave with respect to the SRR, we also discuss different excitation geometries. Finally, we present some modifications to the original SRR design.

3.3.1 Split-ring resonator in the plasmonic picture

As known from basic electrodynamics, straight metallic antennae support different eigenmodes [2]. The eigenmodes, three of which are illustrated by their current distributions in Fig. 3.2(a), result from the boundary conditions given by the geometrical dimensions of the antenna. When we bend the outer parts of the antenna upwards, we obtain an SRR. Its eigenmodes are obtained analogously from the antenna's eigenmodes as depicted in Fig. 3.2(b). The fundamental mode or resonance shown in the first row of Fig. 3.2(b) leads to an oscillating ring current generating a magnetic dipole moment. Thus, we call this mode magnetic mode. As shown in Fig. 3.3, the corresponding magnetic dipole moment is aligned normal to the plane of the SRR. Consequently, it will not lead to a modification of the permeability μ if the incident magnetic field is perpendicular to the generated magnetic dipole moment (see section 3.3.3). In addition to the magnetic dipole moment, the magnetic mode exhibits an electric dipole moment pointing perpendicular to the side wires of the SRR, sketched as red arrow in Fig. 3.3(a). This electric dipole moment allows for coupling to the magnetic mode by an external electric field – materials exhibiting this property are called bi-anisotropic [19]. For the higher-order modes [second and third row of Fig. 3.2(b)], the magnetic dipole moment vanishes or is significantly smaller than for the fundamental mode; the electric dipole moment dominates. Thus, we call these modes: (i) vertical-electric and (ii) horizontal-electric resonance. The terms “vertical” and “horizontal” correspond to the orientation of the electric field needed to excite the respective resonance by a plane wave under normal incidence [the SRR is oriented as sketched in Fig. 3.2(b)].

In the following, we briefly note the qualitative dependence of the spectral position of the magnetic resonance with respect to the SRR's physical dimensions given in Fig. 3.3(b): the total width is l_x , the total height l_y , the thickness t , the width of the side wires w , and the height of the bottom wire h . Altering one of these dimensions leads to the following observations (see the discussion about the polarizability of an ellipsoidal metallic particle in section 2.1.7):

- (i) Scaling down l_x leads to a blue shift (shift to shorter wavelengths) of the magnetic resonance.
- (ii) In contrast, scaling down l_y leads to a red shift (shift to longer wavelengths) of the magnetic resonance.

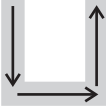
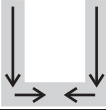
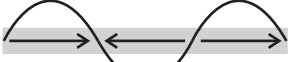
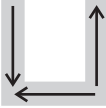
(a) Antenna	(b) SRR	polarization
fundamental mode 	magnetic mode 	
first-order mode 	vertical-electric mode 	
second-order mode 	horizontal-electric mode 	

Figure 3.2: (a) Eigenmodes of a straight antenna. The black arrows illustrate the direction of the eigenmode's currents and the arcs their sinusoidal current distributions. (b) When bending the ends of the antenna upwards, we obtain an SRR. Its eigenmodes can be directly deduced from the eigenmodes of the antenna. The red arrows relate the modes of the SRR to the electric-field direction with which the corresponding mode can be excited by a plane wave under normal incidence (with respect to the plane of the SRR).

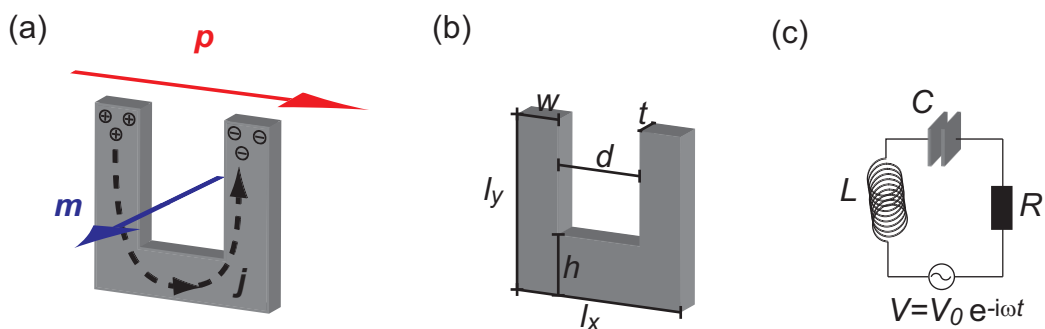


Figure 3.3: (a) Electric (red) and magnetic (blue) dipole moment (p and m , respectively) generated by a separation of charges and the resulting ring current j in an SRR. (b) Dimensions of an SRR and (c) the equivalent RLC -circuit.

- (iii) In the same manner, scaling down t , w , or h leads to a red shift of the magnetic resonance.

Out of these geometrical parameters, the thickness is the one that is the easiest to adjust experimentally (usually the thickness is 25 nm and can easily be doubled to blue-shift the magnetic resonance) since the lateral dimensions of the SRR can be kept constant (this is a fabrication issue, see chapter 4). When altering the width of the side wires and the height of the bottom wire, we note that the magnetic dipole moment is reduced for increased w or h [68]. Usually, SRRs are fabricated on a substrate with a refractive index $n > 1$ leading to a red shift of the spectral position of all resonances (with respect to SRRs in vacuum).

3.3.2 Split-ring resonator as RLC -circuit

The SRR driven by an incident plane wave mimics a driven RLC -circuit as sketched in Fig. 3.3(c) [69]. This equivalent electric circuit consists of a coil with inductance L and a capacitor with capacitance C . In this simple model, the capacitor is formed by the two side wires and the coil is formed by the entire SRR. Thus, the coil consists of a loop with one winding. The damping of the oscillation is accounted for by the resistance R . In the equivalent circuit model, the voltage source takes over the role of the incident plane wave. Then, the LC -resonance frequency is given by

$$\omega_{LC} = \frac{1}{\sqrt{LC}} \quad (3.6)$$

and its quality factor by

$$Q_{LC} := \frac{\omega_p}{\Delta\omega} = \frac{\sqrt{L/C}}{R}, \quad (3.7)$$

where ω_p is the peak position of the resonance and $\Delta\omega$ is the full-width-at-half-maximum (FWHM) of the resonance.

To calculate inductance and capacitance of the SRR, we use textbook formulae. Thus, we assume the coil to be infinitely long leading to $L = (\text{No. of windings}) \mu_0 \frac{\text{area}}{\text{length}}$ and for the capacity, we assume infinitely large rectangular plates leading to $C = \epsilon_0 \epsilon \frac{\text{area}}{\text{distance}}$. In order to obtain a uniform current distribution, the thickness must be much smaller than the lateral dimensions ($t \ll l_x, l_y$). As inductance and capacitance, we find

$$L = \mu_0 \frac{l_x l_y}{t} \text{ and } C = \epsilon_0 \epsilon \frac{(l_y - h)t}{d}, \quad (3.8)$$

respectively. Accordingly, the resonance frequency becomes

$$\omega_{LC} = \frac{c_0}{\sqrt{\epsilon l_x l_y}} \sqrt{\frac{d}{l_y - h}}. \quad (3.9)$$

For estimating the geometric dimensions of an SRR with an LC -resonance at a frequency of $\omega = 2\pi \times 200 \times 10^{12} \text{ s}^{-1}$ ($\approx 1.5 \mu\text{m}$ -wavelength), we consider the following SRR-geometry:

the total width is given by $l_x = l$, the total height by $l_y = l_x = l$, the width of the side wires by w , the height of the bottom wire by $h = w$, and the thickness by t . The required geometrical dimension calculated from Eq. (3.9) are: $l = 200$ nm and $w = 50$ nm. As result of the *RLC*-model, we note that we need SRRs of a few hundred nanometers in size to achieve are resonance wavelength in the range of 1.5 μm .

At the *LC*-resonance, SRRs exhibit a magnetic dipole moment which is given by the product of the current I and the area of the loop. An external magnetic field pointing along the magnetic dipole moment can couple to the magnetic dipole moment and excite the magnetic (*LC*-) resonance. Here, we show that for this excitation geometry (magnetic field is perpendicular to the plane of the SRR) an array of SRRs in the effective-medium limit can be a material for which $\mu \neq 1$ is possible. We restrict the discussion to the quasistatic limit, that is, we do not worry about retardations and assume that Faraday's induction law is valid. Along these lines, for a time-harmonic driving field, the voltage which drives the *RLC*-circuit is [19]

$$V(t) = -\frac{\partial\phi(t)}{\partial t} = -\mu_0 l^2 \frac{\partial H(t)}{\partial t}. \quad (3.10)$$

Here, $\phi(t)$ is the magnetic flux and $H(t) = H_0 \exp(-i\omega t) + cc.$ is the magnetic field of the incident plane wave. The current induced in the SRR reads

$$\begin{aligned} I(t) = I_0 \exp(-i\omega t) + cc. &= \frac{t\omega^2}{1/(LC) - i(R/L)\omega - \omega^2} H_0 \exp(-i\omega t) + cc. \\ &= \frac{t\omega^2}{\omega_{LC}^2 - i\gamma\omega - \omega^2} H_0 \exp(-i\omega t) + cc. \end{aligned} \quad (3.11)$$

Here, we substituted $\omega_{LC} = \sqrt{1/(LC)}$ and $\gamma = R/L$. Many SRRs arranged in an array then exhibit an overall magnetization

$$M(t) = \mu_0 f I(t) l^2 + cc. = \mu_0 f l^2 t \frac{\omega^2}{\omega_{LC}^2 - i\gamma\omega - \omega^2} H_0 \exp(-i\omega t) + cc., \quad (3.12)$$

with f being the filling fraction. Equations (3.3), (3.4), and (3.12) lead to the effective permeability of a magnetic metamaterial made of densely packed SRRs

$$\mu = 1 + f l^2 t \frac{\omega^2}{\omega_{LC}^2 - i\gamma\omega - \omega^2}. \quad (3.13)$$

We note that arrays of SRRs provide the opportunity to tailor the permeability. It can become even negative above the resonance frequency.

In a more sophisticated approach of Ref. [70] to calculate L and C of an SRR, the current distribution is not assumed to be laterally uniform over the SRR (still it is uniform perpendicular to the SRR). Consequently, the charges are not localized at the very end of the SRR but the charges are distributed over the side wires. Additionally, the SRR is not placed in vacuum but on a substrate which is modeled as a half space with refractive index n . In this approach, the inductance becomes

$$L \approx \frac{\mu_0}{2\pi} \{l_1 [\operatorname{arsinh}(2l_1/w) - 1] + l_2 [\phi(w/(2l_2)) - \phi(l_1/l_2)]\}, \quad (3.14)$$

where $l_1 = l_x - w$, $l_2 = l_y - h/2$, and

$$\begin{aligned} \phi(x) = & 0.054 \left[x(1+x^2)(19+x^2) - \sqrt{1+x^2}(1.3+x^2)(19+x^2) \right] \\ & + (0.96 + 0.73x^2) \operatorname{arsinh}(x^{-1}). \end{aligned}$$

The capacitance is given by

$$C \approx \frac{4\epsilon_0(1+n^2)l_2/\pi}{\psi(w/(2l_2)) - \psi(l_1/l_2)}, \quad (3.15)$$

where

$$\begin{aligned} \psi(x) = & 0.0027 \left[x(0.86+x^2)(16+x^2)(23+x^2) - \sqrt{1+x^2}(1.2+x^2)(14+x^2)(24+x^2) \right] \\ & + (0.95 + 0.76x^2) \operatorname{arsinh}(x^{-1}). \end{aligned}$$

The oscillation of the SRR is damped by two mechanisms: (i) Ohmic losses and (ii) radiation losses. The first contribution to the damping can be attributed to Ohm's law $R_{\text{Ohm}} = \sigma/(tw)$, where σ is the conductivity and (tw) is the cross section of the SRR. The second contribution is due to the radiation of energy – so-called radiation damping. In the approach of Ref. [70], the radiation resistance reads

$$R_{\text{rad}} \approx \frac{\pi}{3} \sqrt{\frac{\mu_0}{\epsilon_0}} \left[(1+n)(l_1/\lambda_0)^2 + 8(1+n^3)(l_1 l_2/\lambda_0^2)^2 \right]. \quad (3.16)$$

The entire resistance is then given by $R = R_{\text{rad}} + R_{\text{Ohm}}$.

When considering an individual SRR, the proper quantity to describe its optical properties is the extinction cross-section (see section 2.1.5). Here, we discuss the excitation of the magnetic resonance in an SRR by an external electric field, that is, the electric field is oriented orthogonal to the capacitor plates. From section 2.1.5, we know that the extinction cross-section is defined as the ratio of the extinguished power and the incident intensity. In the RLC -model, the extinguished power is – in the current excitation geometry – given by $P = U^2/R = d^2 \langle E^2 \rangle / (R_{\text{rad}} + R_{\text{Ohm}})$, with U being the electric potential between the two capacitor plates, d is the distance between the two plates of the capacitor and $\langle E^2 \rangle$ denotes the cycle average of the squared electric field. The incident intensity is $\langle E^2 \rangle / Z_0$, where Z_0 is the vacuum impedance. Thus, we obtain for the extinction cross-section

$$C_{\text{ext}} = \frac{Z_0}{R_{\text{rad}} + R_{\text{Ohm}}} d^2. \quad (3.17)$$

3.3.3 Excitation geometries

In this section, we discuss different excitation geometries, *i.e.*, the orientation of the wave vector and the corresponding electric and magnetic field vector to excite the magnetic resonance of an SRR. We already addressed in the previous section that the magnetic mode of the SRR exhibits both an electric and a magnetic dipole moment. Thus, the magnetic resonance can be excited with an external magnetic field and an external electric field. Again, materials

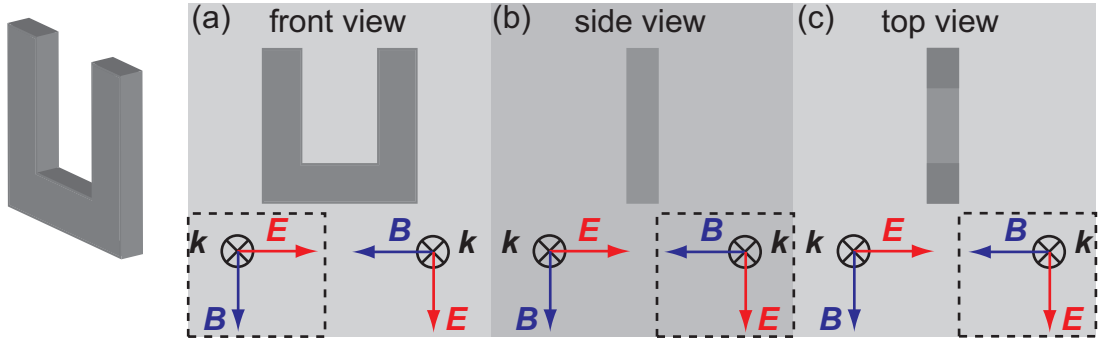


Figure 3.4: Different excitation geometries: (a) front view of an SRR; \mathbf{k} is perpendicular to the plane of the SRR. The magnetic resonance can only be excited when the electric field is oriented perpendicular to the side wires (left \mathbf{EBk} -configuration, indicated by the dashed box). (b) Side view and (c) top view; \mathbf{k} lies in the plane of the SRR. The magnetic resonance can only be excited for those configurations for which the magnetic field is oriented perpendicular to the plane of the SRR (right \mathbf{EBk} -configurations, indicated by the dashed boxes).

exhibiting this property are called bi-anisotropic [19].

The most common excitation geometry [38, 68, 71, 72] is the one sketched in Fig. 3.4(a). Here, the SRRs can be fabricated on a substrate by a 2D fabrication technique like electron-beam lithography (see section 4.1). The wave vector is oriented perpendicular to the plane of the SRR. In this configuration, the magnetic resonance can only be excited when the electric field is perpendicular to the side wires of the SRR. Again, we note that the corresponding magnetic dipole moment is oriented perpendicular to the incident magnetic field. Consequently, the permeability is unity.

The next configuration is sketched in Fig. 3.4(b): the incident light propagates along the bottom wire of the SRR. Here, the magnetic resonance can only be excited when the magnetic field is oriented perpendicular to the plane of the SRR. This configuration is often realized for so-called cut-wire, plate and wire pairs [63, 64, 73] representing slight modifications to the SRR design (see section 3.3.4).

In the third configuration [Fig. 3.4(c)], the light propagates along the side wires of the SRR. Similar to the previous configuration, the magnetic resonance can only be excited, when the magnetic field is oriented perpendicular to the plane of the SRR. In the optical regime, this configuration has been realized in Ref. [39].

In the latter two configurations, the magnetic field of the incident wave is oriented along the magnetic dipole moment. Thus, for these configurations the description of the optical properties requires a permeability different from one. Additionally, we note that retardation in the driving fields plays an important role, *i.e.*, parts of the SRR are driven by the exciting field with a different phase than other parts. When tilting the SRRs of the first configuration [Fig. 3.4(a)], we can achieve electric and magnetic field components similar to the other two configurations [Fig. 3.4(b) and (c)] [71, 72]. Again, retardation in the driving field is important.

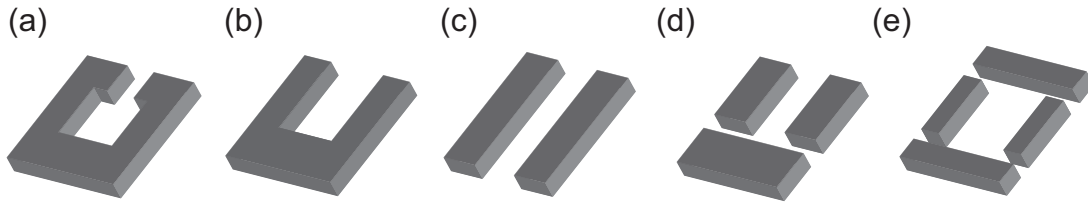


Figure 3.5: Different modifications of SRRs. (a) The original horse-shoe shaped SRR. (b) U-shaped SRR with one slit. (c), (d), and (e) SRRs with two, three, and four slits, respectively, in order to increase the resonance frequency with respect to the SRR with one slit.

3.3.4 Modifications of the split-ring resonator

The SRR is used in different modifications, some of which are shown in Figs. 3.5(a) - (e). In Figs. 3.5(b) - (e), the number of slits, *i.e.*, the number of capacitors is increased. In the *RLC*-model this leads to a decrease of the total capacitance [the different capacitors are connected in series, thus $C_{\text{tot}} = (\sum_i C_i^{-1})^{-1}$]. With Eq. (3.6), we find that for decreased C_{tot} the resonance frequency is increased.

The SRR with two slits in the configuration as shown in Fig. 3.6 is called cut-wire pair [73]. It can be seen as two metallic particles (= the cut wires) in close vicinity to each other. They are close enough to interact *via* their electromagnetic near fields. Then, the coupled system exhibits two eigenmodes: (i) a high-energy symmetric mode and (ii) a low-energy antisymmetric mode. The symmetric mode exhibits the well-known electric dipole moment whereas the antisymmetric mode also exhibits a magnetic dipole moment. The antisymmetric current distribution can be seen as part of the oscillating ring current generating a magnetic dipole moment. When scaling up both cut wires of the cut-wire pair along their short axes such that both axes have the same length, we obtain a magnetic response which is independent of the exciting polarization (we obtain plate pairs [73]). Further scaling up one axis to infinity leads to wire pairs with a high filling fraction when arranged periodically. Consequently, wire pairs possess relatively large values of μ [63, 64].

3.4 A photonic negative-index metamaterial

For a negative index of refraction, we need both negative ϵ and negative μ in an overlapping spectral range³. In the preceding two sections, we showed how permittivity and permeability can be tailored: from the diluted metal, we can obtain a negative ϵ and with magnetic atoms, we can achieve a negative μ . Combining both might lead to a negative-index metamaterial. Historically, the first negative-index metamaterial was composed of a periodic arrangement of SRRs as magnetic atoms and metallic wires acting as diluted metal [60]. The size of the unit cell was 5 mm and the refractive index was negative around a frequency of 10 GHz (≈ 3 cm-wavelength).

In 2005, the diluted metal consisting of stripes has been combined with plate pairs as de-

³The refractive index might become negative even if the real part of ϵ or μ are positive [21]. In this case, the drawback is that the negative refractive index is connected to higher losses [56].

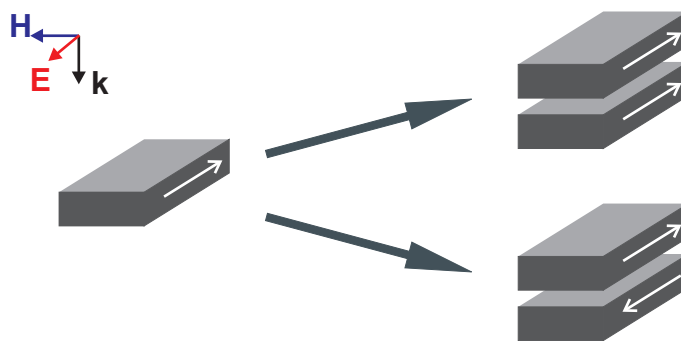


Figure 3.6: The formation of the symmetric and the antisymmetric mode in cut-wire pairs. We start from a single cut wire that acts as an antenna. If we bring another cut wire close to the first one they couple and two modes evolve: a symmetric and an antisymmetric mode (the corresponding currents are visualized by the white arrows). The antisymmetric mode exhibits a magnetic dipole moment that allows for an effective permeability $\mu \neq 1$. The required polarization and propagation direction of the incident plane wave is sketched on the left-hand side.

picted in Fig. 3.7. The combination results in the so-called fishnet structure that exhibits a negative refractive index in the telecommunication spectral range [39]. In Ref. [39], the period is 800 nm and the negative refractive index is observed at about 150 THz-frequency ($\approx 2 \mu\text{m}$ -wavelength). In the fishnet structure, the frequency dependence of the permeability resembles a Lorentz oscillator and the permittivity looks like the permittivity of a Drude metal [74]. Thus, the resonance frequency of the magnetic Lorentz oscillator and the plasma frequency of the diluted metal are good quantities to describe the optical properties of the fishnet. Both parameters can be adjusted by designing the dimensions of the plate pairs and the wires, respectively leading to the desired refractive index. The occurrence of a negative refractive index of the fishnet design has been proven experimentally by measuring the phase velocity [61] and also by measuring the angle of the refracted light [75].

Hitherto, the fishnet structure is the design with the lowest losses accompanying the negative refractive index in the telecommunication spectral range [62]. These low losses allow for transferring the negative refractive index to the visible range by further miniaturizing the design [76]. Even stacking several layers of the fishnet design does not destroy the negative refractive index allowing for a first step towards the realization of three-dimensional (3D) negative index metamaterials [75, 77].

Additionally, the fishnet structure shows other remarkable optical properties that are not directly connected to the negative refractive index: (i) the group velocity of the light becomes negative due to strong dispersion [61]. Here, the appearance of the negative group velocity coincides with the negative phase velocity. (ii) The unit cells of the fishnet couple laterally with each other leading to the formation of magnetization waves traveling along the surface of the fishnet [78].

The fishnet can be fabricated by 2D fabrication techniques like electron-beam lithography [61], focused-ion-beam milling [75], interference lithography [39], and nano-imprint lithography [79]. The latter two fabrication techniques even imply the possibility of fabrication on the cm^2 -scale.

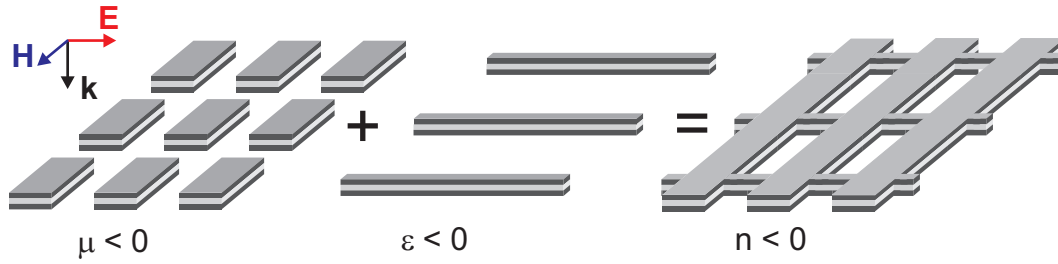


Figure 3.7: Fishnet structure providing a negative refractive index as a combination of plate pairs (with $\mu < 0$) and a diluted metal (with $\epsilon < 0$). The required excitation geometry is sketched on the left-hand side. Adapted from Ref. [74].

3.5 Optical phenomena in metamaterials

This section is dedicated to some of the astonishing optical phenomena metamaterials allow for that are not accessible in naturally occurring materials. The most intriguing aspect surely is the possibility to tailor permittivity and permeability independently from each other.

3.5.1 Magnetic Brewster angle

The polarization state of light reflected at a surface strongly depends on the reflectance angle; for the Brewster angle the reflected light is linearly polarized, even if the incoming light is unpolarized. In other words: for the Brewster angle, one linear polarization is completely transmitted; in usual materials ($\mu = 1$), it is the p -polarization as depicted in Fig. 3.8(a). The origin of the electric Brewster angle lies in the far-field radiation pattern of oscillating electric dipoles: there is no power radiated along the dipole axis [see Eq. (2.35)]. Thus, there is no reflection when the direction of the reflected wave vector is aligned along the electric dipole moment [22]. The (common) electric Brewster angle occurs only for p -polarized incident light.

Clearly, the occurrence of the electric Brewster angle is formally described by the Fresnel equations (2.17a) - (2.17b). For the new class of materials, metamaterials with a magnetic response, we additionally need the permeability to describe their optical properties. In this more general case, the Fresnel equations read (with the same nomenclature as in section 2.1.4) [20]

$$r_s(k_x, k_y) = \frac{\mu_2 k_{z1} - \mu_1 k_{z2}}{\mu_2 k_{z1} + \mu_1 k_{z2}}, \quad r_p(k_x, k_y) = \frac{\epsilon_2 k_{z1} - \epsilon_1 k_{z2}}{\epsilon_2 k_{z1} + \epsilon_1 k_{z2}}, \quad (3.18a)$$

$$t_s(k_x, k_y) = \frac{2\mu_2 k_{z1}}{\mu_2 k_{z1} + \mu_1 k_{z2}}, \quad t_p(k_x, k_y) = \frac{2\epsilon_2 k_{z1}}{k_{z1} + k_{z2}} \sqrt{\frac{\mu_2 \epsilon_1}{\mu_1 \epsilon_2}}. \quad (3.18b)$$

We show in Fig. 3.8(a) [(b)] the resulting reflectance as a function of the angle of incidence for a system consisting of two half spaces with different permittivities (permeabilities) but the same permeabilities (permittivities). In each case, we observe the electric (magnetic) Brewster angle for which the reflection of p -(s -)polarized light is completely suppressed.

For a permeability different from one, oscillating magnetic dipoles are required that are

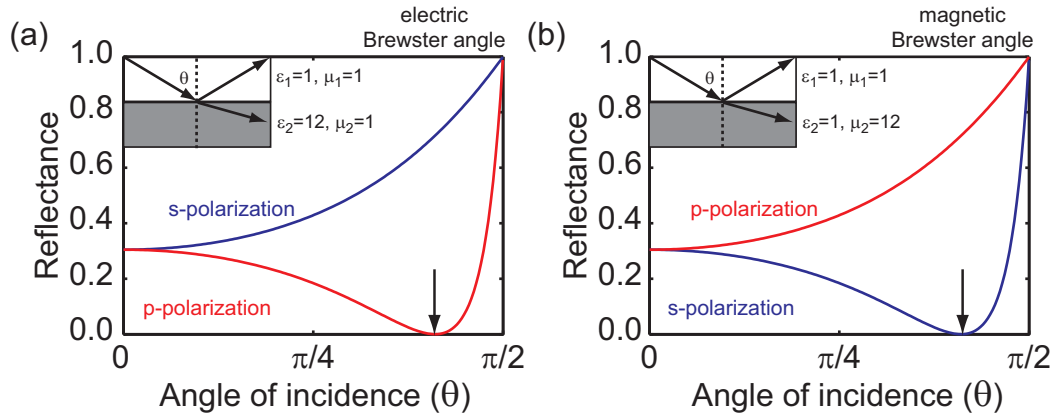


Figure 3.8: (a) Usual reflectance from an interface separating two half spaces with the same permeabilities ($\mu_1 = \mu_2 = 1$) but different permittivities ($\epsilon_1 = 1$ and $\epsilon_2 = 12$). (b) Same as (a) but $\epsilon_1 = \epsilon_2 = 1$, $\mu_1 = 1$ and $\mu_2 = 12$. In each case, we observe an angle (black arrow) for which the reflection of one polarization is completely suppressed – the so-called Brewster angle.

driven by the magnetic field \mathbf{H} . The radiation field of an oscillating magnetic dipole with dipole moment \mathbf{m} can be derived from the radiation field of an oscillating electric dipole with dipole moment \mathbf{p} given by Eq. (2.35) by the following substitution [20]

$$[\mathbf{E}, \mathbf{H}, \mu_0\mu, \epsilon_0\epsilon, \mathbf{p}] \longmapsto [\mathbf{H}, -\mathbf{E}, \epsilon_0\epsilon, \mu_0\mu, \mu\mathbf{m}]. \quad (3.19)$$

Thus, similar to electric dipoles, there is no radiation of energy from magnetic dipoles along the magnetic dipole moment vector \mathbf{m} . In analogy to the electric dipole moment, this explains the existence of the magnetic Brewster angle for materials with $\mu \neq 1$. In contrast to the electric Brewster angle, the magnetic Brewster angle occurs only for *s*-polarized incident light since the magnetic dipoles are driven only by magnetic field, which is perpendicular to the electric field. In the general case, that is, $\epsilon \neq 1$ and $\mu \neq 1$, we find a Brewster angle for *s*- and *p*-polarized light.

3.5.2 Magnetic surface waves

In this section, we discuss surface waves that propagate along the interface between vacuum and a metamaterial described by the effective material parameters $\epsilon(\omega)$ and $\mu(\omega)$.

From section 2.1.7, we know that the dispersion relation of surface plasmon polaritons, *i.e.*, surface waves, for which the only transverse electric field component is perpendicular to the surface (here, the xy -plane), is given by Eq. (2.45). The generalization to metamaterials with $\mu(\omega) \neq 1$ reads [80, 81]

$$k_x^2 = \frac{\epsilon(\omega)^2 - \epsilon(\omega)\mu(\omega)\omega^2}{\epsilon(\omega)^2 - 1} \frac{\omega^2}{c_0^2}. \quad (3.20)$$

For the z -component of the wave vector, we find

$$k_z^2 = \left(\frac{\omega}{c_0}\right)^2 - k_x^2 < 0, \quad (3.21)$$

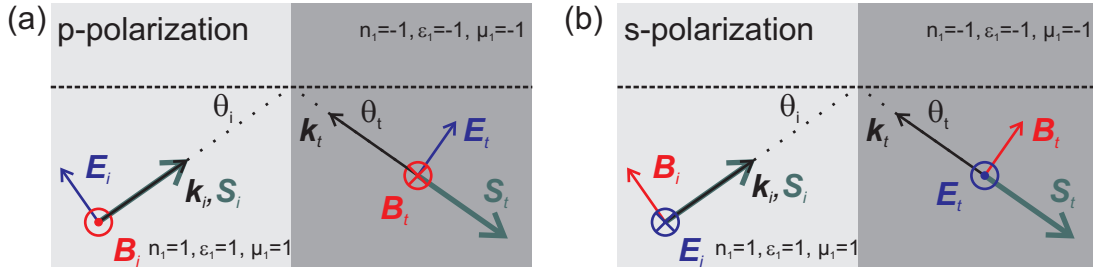


Figure 3.9: Refraction of (a) p -polarized and (b) s -polarized light at an interface separating two half spaces with $\epsilon = \mu = 1$ and $\epsilon = \mu = -1$, respectively.

which leads to an exponential increase or an exponential decay of the wave into the $\pm z$ -direction (normal to the interface); here, the boundary conditions require the wave to decay into the $\pm z$ -direction.

In contrast to ordinary materials, for which only such surface waves exist that can be excited by p -polarized light, metamaterials with $\mu(\omega) \neq 1$ support surface waves with the electric field vector lying in the plane of the surface. Thus, in metamaterials with $\mu(\omega) \neq 1$ also surface waves can be excited by s -polarized light. For these surface waves, the dispersion relation reads [80, 81]

$$k_x^2 = \frac{\mu(\omega)^2 - \epsilon(\omega)\mu(\omega)}{\mu(\omega)^2 - 1} \frac{\omega^2}{c_0^2}. \quad (3.22)$$

3.5.3 Negative refractive index

In this section, we sketch two effects that occur in media with a refractive index of $n = -1$ resulting from $\epsilon = \mu = -1$.

Negative refraction The situation discussed, is sketched in Fig. 3.9(a) [(b)]: an incident s - (p -) polarized light beam impinges under an angle θ_i at an interface separating two half spaces with $\epsilon_1 = 1, \mu_1 = 1$ and $\epsilon_2 = -1, \mu_2 = -1$.

Light impinging from air onto a material will only be reflected, if the impedance $Z = Z_0 \sqrt{\frac{\mu}{\epsilon}}$ of the material is different from the vacuum impedance $Z_0 \approx 377\Omega$. Since in our case, the ratio $\frac{\mu}{\epsilon}$ is unity on both sides of the interface, there is no reflected wave. Along the lines of section 2.1.4, we find that for s - (p -) polarized light, the electric (magnetic) field changes its sign and the magnetic (electric) field is mirrored at the plane of the interface. From the relative orientation of the fields, we can calculate (i) the wave vector *via* $\mathbf{k} = \omega \mathbf{E} \times \mathbf{B}$ and (ii) the Poynting vector $\mathbf{S} = \frac{1}{2} \text{Re}(\mathbf{E} \times \mathbf{H}^*)$ in the medium. We find that the light is refracted to the “wrong” side of the interface normal corresponding to Snell’s law with a negative refractive index. Additionally, wave and Poynting vector are aligned antiparallel to each other, leading to a phenomenon called backward waves [29], *i.e.*, the phase velocity points into the opposite direction of the energy transport.

Perfect lens phenomenon We can utilize a negative refractive index material as a planar lens as shown in Fig. 3.10 [3]. In Ref. [5], it has been shown that this kind of lens, in princi-

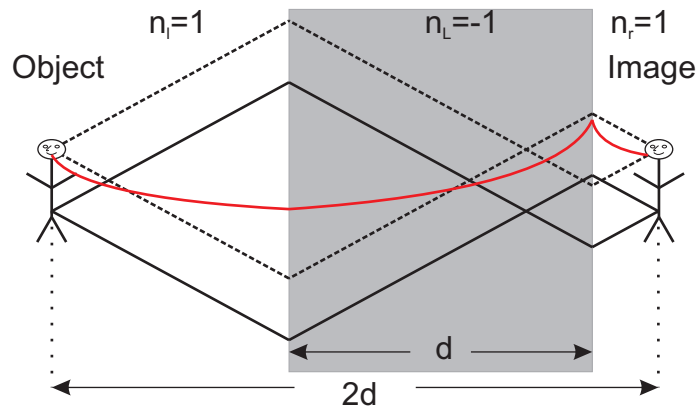


Figure 3.10: Imaging by a slab of thickness d with $n = -1$. The solid and dashed lines depict rays that are emitted by the object. The image is generated at a distance from the object of twice the thickness of the slab leading to a vanishing optical path length. The red line shows the behavior of the evanescent modes.

ple, allows for imaging without limitations regarding the resolution – even sub-wavelength objects can be resolved. Such objects emit light consisting of propagating (the wave vector is real) and evanescent modes (the wave vector is imaginary). The evanescent modes do not contribute to the far fields. Thus, they can not be used for imaging by conventional lenses leading to an information loss: the image is blurred.

In the region of $n = -1$ (shaded region in Fig. 3.10), we observe a phenomenon that can be interpreted as exponential growth of modes which are evanescent in the region where $n = 1$ (sketched as red lines in Fig. 3.10). We find that at the position of the image, the magnitude of the evanescent modes is the same as at the position of the object. Thus, no information is lost and the image resembles the object perfectly. The underlying mechanism is the following: the fields (the propagating and evanescent modes) interacting with the surface of the lens generate surface waves like those discussed in section 3.5.2. As already pointed out, also growing modes are covered by Eq. (3.21) and here, the boundary conditions (with the object in close proximity to the slab) require growing modes into the propagation direction. It is important to note that the Kramers-Kronig relations require losses for a refractive index different from one [82–84]. Thus, if $\text{Re}(n) = -1$, we must have $\text{Im}(n) > 0$. The losses can be very small, but even for small losses the resolution of the image decreases rapidly [58].

3.5.4 Transformation optics

The principles of transformation optics [7, 8] can be explained by geometrical optics: we assume that the wavelength of the light is much smaller than the objects it interacts with. In this approximation, electromagnetic waves are treated as rays traveling from a point A to a point B . Between these two points, we assume a spatial refractive index distribution $n(\mathbf{r})$. The path the light travels is given by Fermat's principle, which states that the light always travels along the shortest optical path between A and B [55]⁴. Fermat's principle can be

⁴In general, light travels along the path, for which the travel time becomes an extremum or a saddle point. Usually, it is a minimum.

written as variational principle

$$\delta \int_A^B n(\mathbf{r}) ds = 0, \quad (3.23)$$

where $\int_A^B n(\mathbf{r}) ds$ is the optical path length, ds is the differential element of length along the path, and δ denotes the variation. Knowing this, we can envision a spatial refractive index distribution that bends light in a desired way.

The spatial distribution of the refractive index can be translated to a transformation of space: in an arbitrary coordinate system, Fermat's principle states that light always travels along geodesics. For example, when we transform the space such that a point (*e.g.* the origin) is transformed onto the surface of a sphere around that point, light can not enter the inner of the sphere. Thus, we can not see an object that might be placed within the sphere – the object is cloaked [7, 8]. This is the basic idea of the electromagnetic cloaking of objects, *i.e.*, making them invisible for electromagnetic radiation of a specific spectral range.

Chapter 4

Experimental methods I: fabrication

In this chapter, we describe different lithography techniques, which are used for the fabrication of metallic nanostructures. With this, our focus lies on electron-beam lithography since all nanostructures investigated in this thesis have been fabricated by this technique. It is a versatile fabrication technique, whose resolution is superior to, for instance, optical lithography. Additionally, we describe three alternative fabrication techniques in this chapter: focused-ion-beam, laser-interference, and nano-imprint lithography.

4.1 Electron-beam lithography

In electron-beam lithography, we employ the superior resolution capabilities of a focused electron beam. Impinging onto a thin (≈ 200 nm) electron-beam-resist layer, the electrons modify the resist. In our case, the resist is a polymer, precisely, polymethyl methacrylate (PMMA)¹. For the positive tone resist PMMA, the exposed parts can be selectively dissolved in a chemical – the so-called developer. What remains is used as a template for post-processing, that is, we evaporate thin layers of material and subsequently perform the lift-off. In this section, we also address our sample-preparation and post-processing technology. The entire process (preparation, lithography and post-processing) is sketched in Fig. 4.1. Except for details, sample preparation and the post-processing procedure are very similar for the other fabrication techniques presented in sections 4.2 - 4.4.

4.1.1 Sample preparation

The substrate used is either polished Suprasil² or a semiconductor. Clearly, the substrates have to be polished since their surface roughness must be well below the desired feature size. Additionally, for optical experiments, we need substrates that are transparent in the relevant spectral range. Furthermore, since we have to avoid charging during the exposure with electrons, we need conductive substrates. Thus, if the substrate itself, like Suprasil,

¹PMMA 950K A4 (4%-solution in anisole), MicroChem Corp., Newton (USA)

²Suprasil is a high-purity quartz glass. A slab of 2 mm-thickness has more than 90% transmittance between 0.2 μm and 2.5 μm wavelengths [86].

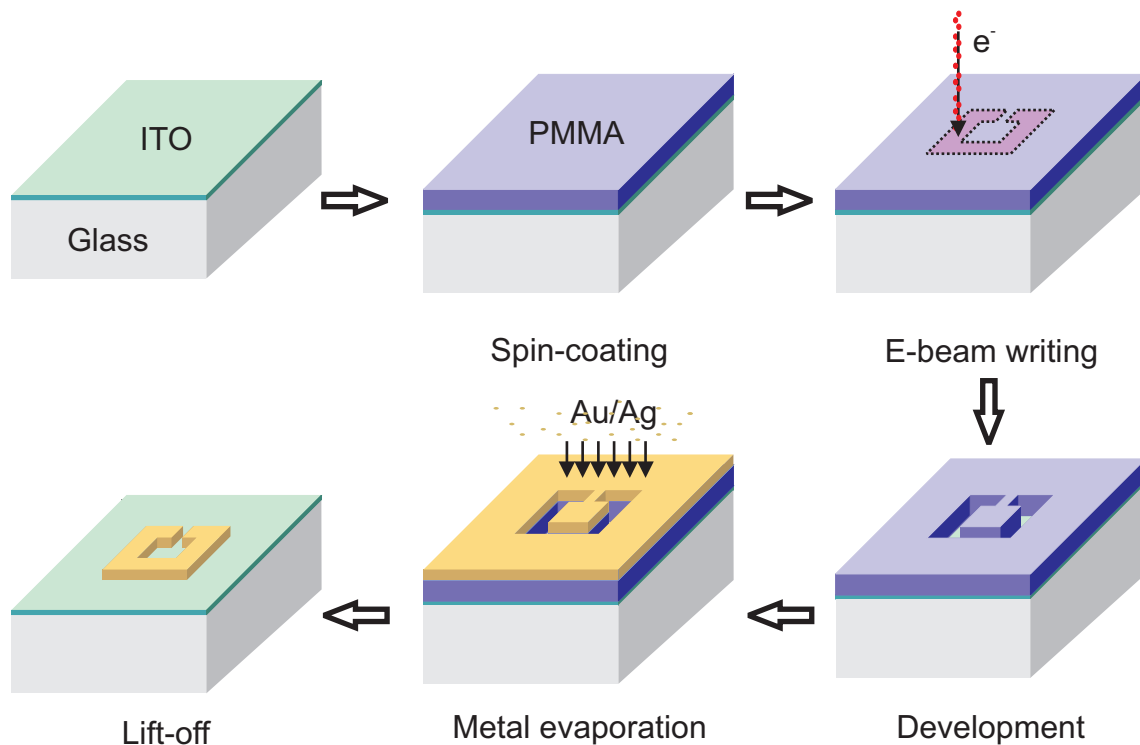


Figure 4.1: Sketch of the entire electron-beam lithography process as explained in detail in the main text: we start with a clean, conductive ITO-covered glass substrate that is spin-coated with the electron-beam sensitive resist PMMA. The focused electron beam modifies the resist making it soluble in the developer, that is, the exposed parts of the PMMA are etched away. After the development, we evaporate layers of dielectrics and/or metals. The lift-off procedure removes the PMMA and the desired nanostructure remains. Adapted from Ref. [85].

is not conductive, we evaporate a 5 nm-thin layer of indium tin oxide (ITO) which is both conductive and transparent in the optical spectral range [87]: it allows for electron-beam lithography *and* it does not disturb our optical measurements.

Cleaning the substrates We clean the substrate two-fold to assure that we always start the lithography process with a very clean substrate. This makes the entire process reproducible. The first step is the chemical etching of all organic residues off the substrates in a 1 : 1-mixture of sulfuric acid (H_2SO_4) and hydrogen peroxide (H_2O_2) at a temperature of $120^\circ C$ for thirty minutes. This mixture is also known as Piranha solution. After taking the substrate out of the Piranha solution, it is rinsed in distilled water and subsequently blown dry with nitrogen. Before going to the second cleaning step, we check if the substrates are specular with no residues. The clean substrates (no residues) can be used right away for lithography, the others are cleaned by mechanically polishing them with acetone soaked lens-cleaning papers until no residues are left.

Covering with indium tin oxide In the next step, we evaporate a 5 nm-thin ITO-layer in an electron-beam evaporation chamber in an oxygen atmosphere with a partial pressure of

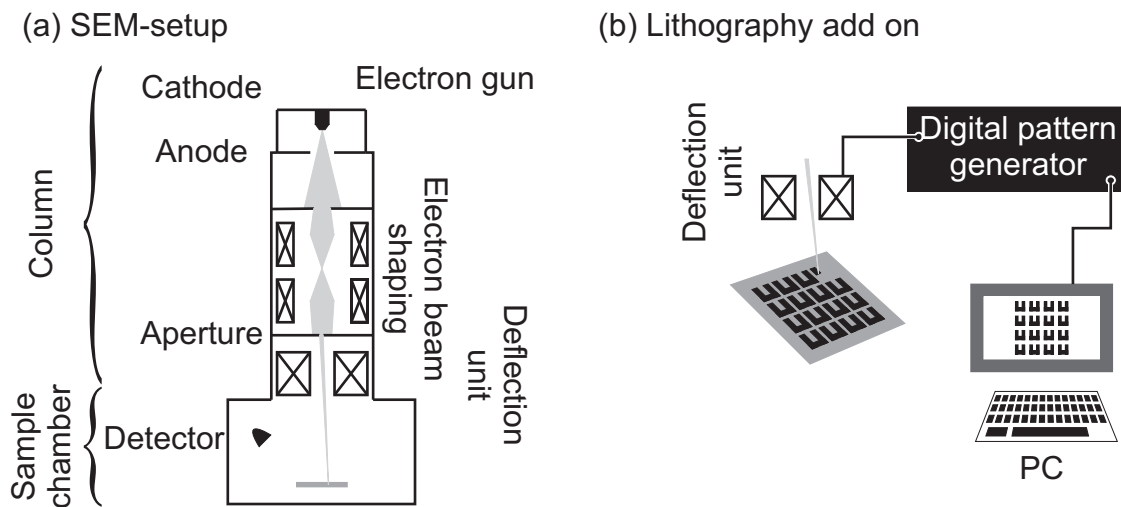


Figure 4.2: (a) Sketch of an SEM consisting of the column and the sample chamber. The trajectory of the electron beam is visualized by the shaded areas. For lithography purposes the SEM is equipped with a digital pattern generator connected to a computer as shown in (b). The desired design is defined *via* the design software e_LINE.

$p_{\text{O}_2} = 1.2 \times 10^{-5}$ mbar. After evaporation, the ITO-layer looks grayish and not transparent at all. Thus, an annealing procedure is required which is performed at a temperature of 400°C for six hours under ambient air pressure. To avoid cracks in the substrate or the ITO-layer, we apply a temperature ramp of 5°C min^{-1} for both heating and cooling. After annealing, the ITO-layer is transparent and conductive. This step is only required for insulating substrates.

Spin-coating and developing the electron-beam resist The resist is spin-coated on the substrate by two subsequent spin steps: (i) three seconds at 300 rpm to disperse the resist over the substrate and (ii) 90 seconds at 4000 rpm resulting in a final PMMA-layer thickness of about 200 nm. Finally, the resist is baked at 165°C for 45 minutes under ambient pressure to remove the PMMA solvent.

For PMMA, the exposed regions are selectively etched by the developer [1 : 3-mixture of MIBK (methyl isobutyl ketone) and IPA (isopropyl alcohol)]. We develop the exposed PMMA under ambient conditions for three to ten seconds (depending on the actual structure design).

4.1.2 Lithography

Experimental setup The electron-beam lithography is carried out by a commercial scanning-electron microscope (SEM) that is specially equipped and only used for electron-beam lithography. We use RAITH e_LINE³ that similar to ordinary SEMs consists of two main components as sketched in Fig. 4.2(a): the column where the electron beam is generated, accelerated, shaped and focused onto the sample and the sample chamber containing the stage with the sample and the detectors delivering the information for imaging.

³Raith GmbH, Dortmund (Germany)

The column is a Zeiss GEMINI⁴ column: the electron beam is generated at the very top – in the so-called electron gun. It consists of an electron source, which is a field-emission source made of a heated ZrO/W-tip supplying high and stable currents. Both attributes are crucial for high-resolution electron-beam lithography. After generation, the electrons are accelerated by an adjustable acceleration voltage between cathode and anode. An arrangement of magnetostatic and electrostatic lenses and an aperture focus the electron beam on the sample surface.

The electron beam is scanned over the sample surface by the deflection unit. When the electron impinges onto the sample, it generates secondary electrons that are collected by two types of detectors: one detector is placed off the beam axis as shown in Fig. 4.2(a) – the so-called SE2-detector. The other detector is placed inside the column [not shown in Fig. 4.2(a)] – the so-called In-Lens detector. The detector signal is proportional to the number of electrons hitting the detector. Together with the position information of the electron beam on the surface from the deflection unit, we obtain an image of the sample surface. The image resolution can be below one nanometer [88]. For the SEM used here, the manufacturer claims 1.7 nm resolution at an acceleration voltage of 15 kV.

In electron microscopes used for lithography, the deflection unit can be controlled externally by the so-called digital pattern generator as depicted in Fig. 4.2(b). The electron beam is deflected such that it traces the desired design. Additionally, an amperemeter is added (not shown) that measures the electron-beam current. Furthermore, the lithography SEM used is equipped with an interferometer-controlled stage allowing for movements with a precision of 2 nm, a position repeatability below 40 nm, and a total travel range of 100 mm × 100 mm (usually, SEM stages provide much less precision, position repeatability, and travel range). For designing the structure, we use a computer aided design software (e_LINE software tool), which is provided with RAITH e_LINE. The structure is defined by geometrical shapes composed of areas, that is, polygons or disks, and lines. The designed structure is discretized, *i.e.*, divided into square sections of 1.6 nm edge length (the so-called step size) and then sent to the digital pattern generator.

When exposing area design elements [see left-hand side of Fig. 4.3(a)], the electron beam meanders over the designed area, leading to well-defined rectangles with sharp corners [see left-hand side of Fig. 4.3(b)]. In contrast, for line design elements [see right-hand side of Fig. 4.3(a)], the electron beam moves once along the designed line, that is, the dose is deposited only along this line. Thus, the width of the exposed area completely relies on the proximity effect (see below) causing roundish corners [shown on the right-hand side of Fig. 4.3(b)]. The exposure doses for lines and areas are defined by a relative dose factor and by the line and area dwell times, respectively. The relative dose factor depends on the design itself and on the deposited dose in the vicinity of the object. For example, structures that are densely packed in a periodic lattice require less relative doses than those which are strongly diluted – this effect is called proximity effect. The proximity effect has a major impact on the quality of the structure. Thus, for each structure the relative dose has to be adjusted individually in order to precompensate the proximity effect.

⁴Carl Zeiss SMT AG, Oberkochen (Germany)

The dwell times depend on the resist sensitivity, the step size, and the current of the electron beam. The resist sensitivity depends on the acceleration voltage (we use 30 kV) and the resist. For the area design elements, we use $400 \mu\text{C cm}^{-2}$ and for the line design elements 6000 pC cm^{-1} as resist sensitivity for PMMA at 30 kV acceleration voltage. The step size is set to 1.6 nm. Before every exposure, we measure the current, which is usually about 40 pA, 90 pA, and 4000 pA for different aperture sizes, namely 10 μm , 20 μm and 120 μm , respectively. The lithography is performed at a working distance of about 12 mm with a magnification of 1000 \times . With these column settings, the electron beam can be deflected such that it can scan areas (the so-called write fields) of $100 \mu\text{m} \times 100 \mu\text{m}$ in size.

Resolution The resolution of electron-beam lithography is mainly limited by three effects:

- (i) The size and shape of the electron beam on the resist surface: the size has to be as small as allowed by hardware restrictions and the shape should be as close to circular as possible. Both are manually adjusted through the user by a procedure called contamination-spot-burning. Here, we direct the beam on a position of the resist surface for several seconds. This leads to a spatially confined contamination on the resist surface visible as a bright spot in the SEM image. The electromagnetic lenses are adjusted such that the spot is circular and as small as possible.
- (ii) Proximity effect [89]: inside the resist and the substrate the electron beam is scattered and generates secondary electrons which also expose regions of the resist that are not struck by the electron beam in the first place. The extent of the proximity effect depends on the acceleration voltage, the resist, and the substrate material used. The acceleration voltage of 30 kV has proven to minimize the proximity effect for the acceleration voltages available.
- (iii) Intrinsic resolution of the resist: for the resist PMMA used, the supplier claims a resolution of smaller than 100 nm. This is pessimistic: in this work, we have fabricated structures with feature sizes well below 20 nm and in Ref. [90], feature sizes of 5 nm in PMMA have been reported.

4.1.3 Post-processing: from the template to the final nanostructure

In general, the polymer templates fabricated by electron-beam lithography do not show extraordinary optical properties. Consequently, for the final metamaterials, we cover the polymer template on the substrate with metal (or a metal-dielectric composite) and subsequently remove the layer in the so-called lift-off procedure.

We deposit the metal layer by electron-beam evaporation. Similar to the deposition of ITO, an accelerated electron beam heats the material (here a metal like gold or silver) such that it starts evaporating. The entire process takes place under vacuum conditions, at a pressure of about 5×10^{-7} mbar. The layer thicknesses for metamaterial fabrication usually vary between about 20 nm and 200 nm.

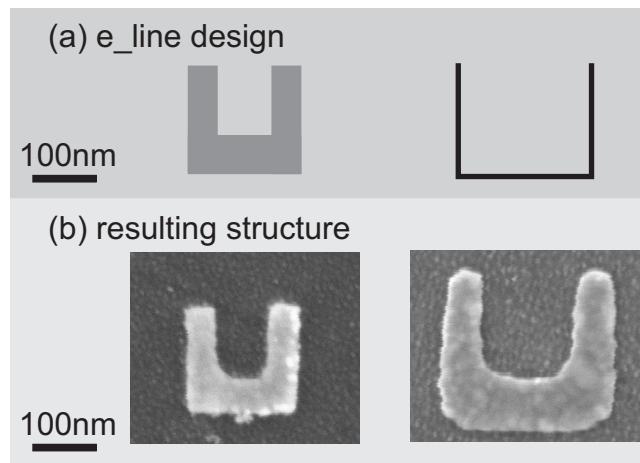


Figure 4.3: (a) Two split-ring resonators as designed in the e_LINE-software tool. Left: the design elements are areas. Right: the design elements are lines. (b) The corresponding scanning-electron micrographs of the resulting structures made of 25 nm thick gold. For those structures designed with area design elements, the corners are sharper than for the line elements.

After metal deposition, we remove the polymer template in a hot (60 °C) acetone bath. When the metal layer shrivels (this happens after about two minutes), we apply ultrasonic vibrations for about 30 s to completely remove the parts of the metal layer that are connected to the template. This is a critical step since the ultrasonic bath has enough power to remove the entire metal layer off the substrate or even to break the substrate itself.

4.1.4 Fabrication of complementary split-ring resonators

For fabricating SRRs, the design is illustrated in Fig. 4.4(a) – it consists of three rectangular area design elements. After the development (the development time is eight seconds), the template consists of SRR-shaped holes in a PMMA layer. The evaporation of gold and the subsequent lift-off lead to gold SRRs on the substrate.

The fabrication of complementary SRRs (CSRRs) turns out to be more difficult. Complementary SRRs can be thought of as SRRs for which the metal in the sample plane is replaced by air and *vice versa* (see section 6.1). Here, the template consists of PMMA SRRs on the substrate. Two problems occur: (i) the PMMA SRRs detach from the substrate during development and (ii) the lift-off does not work properly caused due to some PMMA SRRs being enclosed by the gold such that the PMMA can not be dissolved in the hot acetone bath and remain on the substrate. We could overcome these difficulties by reducing the development time to three seconds. Additionally, we embed a stepwise dose gradient in the design file as illustrated in Fig. 4.4. The dose gradient starts at the unit cell boundaries with a relative dose of 0.6 and goes up to 0.8 in five equidistant steps. A drawback of this design is the long exposure time: since the dose gradient is realized by many rectangular area design elements, the overall exposure time goes up to six hours for a single $100\ \mu\text{m} \times 100\ \mu\text{m}$ -write field. We have tried different realizations of the dose gradient, but the one illustrated in Fig. 4.4(b) leads to the best results.

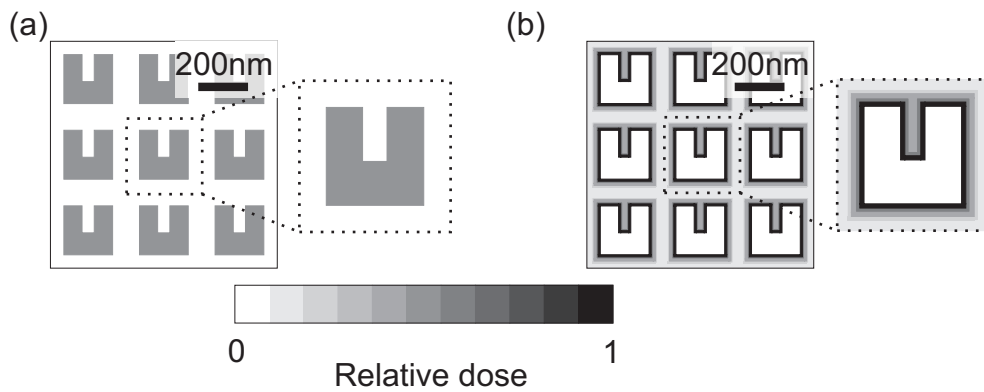


Figure 4.4: Designed dose deposition for the fabrication of (a) SRRs and (b) CSRRs. For the fabrication of CSRRs, we apply a dose gradient. The insets show the corresponding unit cells of the design.

The write-field area is set to $100\ \mu\text{m} \times 100\ \mu\text{m}$, the acceleration voltage to 30 kV, and the aperture size to $20\ \mu\text{m}$. The current from the electron beam is about 90 pA.

4.1.5 Fabrication of isolated split-ring resonators

Investigating isolated SRRs and pairs of SRRs by means of the spatial modulation technique presented in section 5.3 requires on the one hand the structure itself and on the other hand large (about $20\ \mu\text{m} \times 20\ \mu\text{m}$ in size) gold rectangles – so-called knife-edges for both locating the isolated structure and measuring the dimensions of the Gaussian beam (see section 5.3.5). The isolated structures, that is, SRRs and pairs of SRRs (see sections 7.1 and 7.2) are designed in the same way as the periodic SRR arrays. Here, the reduced proximity effect leads to a higher relative dose being about 2.2. Also for the isolated structures, the write-field area is set to $100\ \mu\text{m} \times 100\ \mu\text{m}$, the acceleration voltage is 30 kV, and the aperture size is $10\ \mu\text{m}$. The typical current of the electron beam is about 36 pA.

For exposing the knife-edges, we choose the same write-field area and acceleration voltage as for the isolated structures. In order to speed up the exposure process, we choose the $120\ \mu\text{m}$ -aperture leading to a current of 4000 pA and we adapt the step size to 19 nm. A relative area dose of 1.2 is sufficient for decent knife-edges.

4.1.6 Fabrication of split-ring resonators on ultra thin substrates

Our EELS experiments (see chapter 8) require substrates which are transparent for fast electrons. Therefore, the substrate has to be as thin as possible. Here, we use Si_3N_4 -membranes⁵ that are only 30 nm thin, which is sufficient for meaningful EELS experiments.

The membranes are usually fabricated by covering a silicon wafer with a thin Si_3N_4 -layer. Subsequently, the wafer is etched from the rear side with potassium hydroxide (KOH) in a specific region. The Si_3N_4 -layer acts as a stopper of the etching process. What remains is a window made of a 30 nm-thin layer Si_3N_4 of a specific size (in our case $100\ \mu\text{m} \times 100\ \mu\text{m}$ or

⁵SiRN-MFA3-TEM-200-0.1-30, Silson Ltd., Northampton (UK)

50 $\mu\text{m} \times 50 \mu\text{m}$) carried by a silicon frame of – in our case – 200 μm thickness. The frames are octagonal with a maximum corner-to-corner distance of 3.05 mm to fit into the standardized sample holders of transmission-electron microscopes (TEMs). The window is placed in the middle of the octagon. We can use the membranes for electron-beam lithography. However, we have to keep in mind that they are very fragile.

There are several steps in the fabrication process, which we have to modify for using Si_3N_4 -membranes as substrates:

- The membranes are sufficiently conductive. Thus, we do not need to evaporate ITO. Nevertheless, we have fabricated photonic atoms on membranes with and without a 5 nm-thin ITO-layer.
- For spin-coating the resist, the substrates are usually fixed by a vacuum chuck. Clearly, this kind of chuck can not be used for the thin membranes: it would rupture the membrane. Consequently, we use a home-made chuck that mechanically fixes the silicon frame. The spin-coating parameters are the same as for the other substrates.
- Before starting the exposure, we have to locate the membrane. This is done by moving the electron beam into the vicinity of the membrane. Subsequently, an image is taken by scanning the electron beam once (in order to minimize the deposited dose) over the sample to locate the membrane.
- The relative dose is approximately three times higher than for the SRR arrays on usual substrates due to the reduced proximity effect by the absence of back-scattered electrons.
- The lift-off is done in a cold acetone bath for three hours. The ultrasonic bath can not be used.

4.2 Focused-ion-beam lithography

Focused-ion-beam milling allows for removing material in very confined areas – the typical feature size is smaller than 100 nm [91]. The apparatus used is very similar to an SEM, but here, instead of the electron beam an ion beam (usually Ga^+ -ions) is accelerated and focused onto the surface of the sample. Since the Ga^+ -ions are much heavier and larger than electrons, they do not penetrate the sample but remove atoms from the surface. After losing their kinetic energy, Ga^+ -ions remain in the crystal matrix, forming local impurities. Additionally, parts of the removed material redeposit at the surface of the sample.

Focused-ion-beam lithography exploits the high spatial control of focused-ion-beam milling for patterning layers of material directly. The electronics used is the same as in electron-beam lithography. Along these lines, several photonic metamaterials have been fabricated [68, 75]. Unfortunately, when patterning metals like gold [68] or silver [75], the optical quality suffers from Ga^+ -ions that penetrate the metal lattice and serve as additional scattering centers for the conduction electrons leading to higher damping and increased losses. In contrast to

electron-beam lithography, no post-processing like evaporation of metal layers and lift-off is required.

4.3 Laser-interference lithography

In laser-interference lithography, two or more laser beams interfere leading to a standing wave pattern [92]. The intensity variation takes place in a photo sensitive material, the so-called photo resist, which is chemically altered in the regions of high intensity. After exposure, the photo resist is developed and forms a template for post-processing.

For a one-dimensionally (1D) periodic intensity variation (resulting in stripes in the photo resist), two interfering beams are required, whereas three interfering beams lead to a periodic 2D intensity pattern. Both single and multiple application of two-beam interference have been used for the fabrication of planar metamaterial arrays [39, 64, 93]. In Ref. [64], also three-beam interference lithography has been applied for the fabrication of metamaterial slabs.

By the interference of four or more beams also 3D intensity variations can be realized leading to a 3D structured template; with appropriate post-processing techniques, this might be a possibility for realizing 3D metamaterials.

The major drawback of this technique is the limited design freedom of the unit cell. This drawback can partially be overcome by a huge effort either in the fabrication procedure (a combination of several exposures, reactive ion etching and shadow evaporation) or by applying multiple-beam exposures, that, however, are very sensitive to mechanical vibrations. The major advantage is the possibility to fabricate metamaterials at low costs and on a cm^2 -scale.

4.4 Nano-imprint lithography

Nano-imprint lithography is a technique in which an imprint resist is mechanically deformed [94]. It has been used for fabricating the fishnet structure in Ref. [79].

As in electron-beam and laser-interference lithography, the patterned resist serves as template for post-processing. For the deformation of the resist, a patterned stamp – also called mold – is required. Thus, first of all, the mold has to be fabricated, which is done by electron-beam or optical lithography. The mold is pressed into the resist causing a deformation of the resist. Before removing the mold, the resist has to be mechanically stable which can be achieved in two ways:

- (i) When the pressure of the mold is applied onto the resist, the resist is heated up above its glass transition temperature. The pattern of the mold is transferred to the resist. By cooling down, the resist becomes mechanically stable and the mold can be pulled out [94].
- (ii) The resist is liquid in the first place but after exposing with ultraviolet light, it solidifies and the mold can be removed [95].

After removing the mold, resist remains on the substrate that has to be removed by reactive-ion etching. Like interference lithography, nano-imprint lithography allows for patterning areas of macroscopic scale. For this purpose, sophisticated machines are required that assure the same pressure over the entire substrate.

Chapter 5

Experimental methods II: characterization

In this chapter, we introduce the experimental methods (including the corresponding analysis of the raw data) we use for investigating the linear and nonlinear optical properties of metamaterial arrays and isolated photonic atoms.

We start with the description of the setups we employ for the linear and nonlinear optical characterization of metamaterial arrays. Then, we present the spatial modulation technique we use for the linear optical characterization of isolated photonic atoms. Finally, we describe the EELS apparatus.

5.1 Linear optical characterization of metamaterial arrays

For the characterization of the linear optical properties of metamaterial arrays, we use a commercial Fourier-transform-infrared spectrometer (FTIR) with a tungsten halogen light source¹ attached to an optical microscope². The optical microscope serves to localize the small samples and allows for measuring transmittance and reflectance spectra in the range of $0.4\ \mu\text{m}$ to $5\ \mu\text{m}$ wavelength. Clearly, for covering such a spectral range different detectors and optical components are required. Thus, the spectral range of the FTIR is split into two parts:

- (i) $0.4\ \mu\text{m}$ - $1.2\ \mu\text{m}$: quartz beam splitter and silicon diode detector
- (ii) $0.9\ \mu\text{m}$ - $5\ \mu\text{m}$: calcium-fluoride beam splitter and liquid-nitrogen cooled indium-antimonide diode detector

For both spectral regions, we use a thallium bromo-iodide polarizer to obtain linearly polarized light.

The incident light is focused on the sample by a reflective Cassegrain lens (magnification: $36\times$, $\text{NA} = 0.5$). The light is collected by an identical Cassegrain lens and imaged onto

¹Bruker Equinox 55, Bruker Optik GmbH (Germany)

²Bruker Hyperion 1000, Bruker Optik GmbH (Germany)

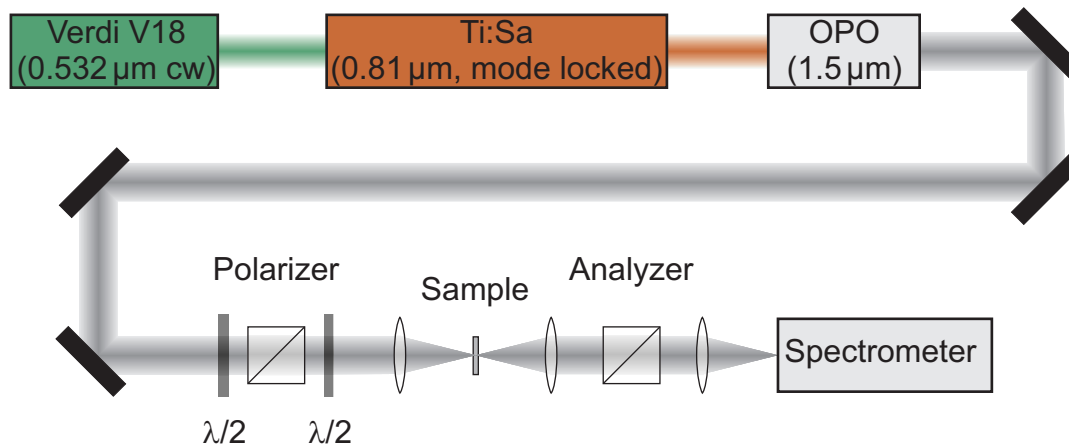


Figure 5.1: Home-built setup for measuring SHG and THG intensities from metamaterial arrays.

a plane where we can place apertures of different sizes that allow for selectively measuring transmittance and reflectance spectra of small areas (from $8\ \mu\text{m}$ to $100\ \mu\text{m}$ in diameter) of the sample.

The sample is placed perpendicular to the optical axis. However, due to the Cassegrain optics the incident light impinges under angles between 15 degrees to 30 degrees onto the sample. Thus, spectra under strict normal incidence can not be measured easily. Nevertheless, for most samples assuming normal incidence leads to a good agreement with numerical results.

5.2 Nonlinear optical characterization of metamaterial arrays

For the nonlinear optical characterization of metamaterial arrays, we use the setup, sketched in Fig 5.1. The light source is a commercial optical parametric oscillator (OPO)³, which is adjusted such that it emits pulses at a center wavelength of $1.5\ \mu\text{m}$ with a pulse duration of 170 fs. The repetition rate is 81 MHz and the emitted power is set to 90 mW, which is equivalent to 6.8×10^{17} photons per second at 0.826 eV energy.

The OPO is pumped by a titanium sapphire (Ti:Sa) laser⁴ emitting pulses at a center wavelength of $0.81\ \mu\text{m}$ with a pulse duration of 120 fs. The repetition rate is 81 MHz and the emitted power is 2.1 W. The Ti:Sa in turn is pumped by a diode-pumped continuous-wave frequency-doubled solid state (Nd:Vanadate) laser⁵ emitting 11 W power at $0.532\ \mu\text{m}$ -wavelength.

The power impinging from the OPO onto the sample is adjusted by a combination of a half-wave plate and a polarizer as depicted in Fig 5.1. Its polarization can be adjusted by a second half-wave plate. The linearly polarized pulses from the OPO are focused onto the sample by a boro-silicate lens ($f = 100\ \text{mm}$) resulting in a focus radius of $w_0 = 30\ \mu\text{m}$ and a Rayleigh

³OPAL, SpectraPhysics Inc. (USA), now: Newport Inc.

⁴Tsunami, SpectraPhysics Inc. (USA), now: Newport Inc.

⁵VerdiV18, Coherent (USA)

length of $z_R = 1800 \mu\text{m}$ (see section 2.5) as measured by a knife-edge technique [96]. We estimate the peak intensity in the focus to be $4 \times 10^7 \text{ W cm}^{-2}$ and the peak electric field strength to be $2 \times 10^7 \text{ V m}^{-1}$.

The light emitted by the sample into the forward direction is collected by a second identical lens and imaged onto the entrance slit of a 0.25 m grating spectrometer⁶ connected to a liquid-nitrogen cooled silicon charge-coupled-device (CCD) camera⁷. The grating spectrometer serves as a dispersive filter for discriminating the fundamental wavelength from the SHG and THG wavelengths.

We estimate that for SHG (THG) the number of photons is roughly a factor of 3 (8) higher than the integral number of counts given by the CCD camera due to the quantum efficiency of the CCD camera and losses in the optical path.

5.3 Linear optical characterization of isolated photonic atoms by means of a spatial modulation technique

The linear optical properties of isolated metallic nanostructures can be measured by various techniques, like

- (i) Attenuated-total-internal-reflection spectroscopy [97]: a beam undergoes total internal reflection at an interface between a high- and a low-refractive-index medium. If the angle of incidence is larger than the so-called critical angle (see section 2.1.4), no light is transmitted through this interface. However, non-radiating evanescent fields leak into the low-index medium. These non-radiating fields can become radiative when they interact, for instance, with metallic nanoparticles. Thus, the measured intensity is proportional to the scattering cross-section. Unfortunately, this technique does not provide information about the absorption cross-section and it provides only qualitative information about the scattering cross-section.
- (ii) Dark-field spectroscopy [98]: dark-field imaging is a well-established technique in (light and electron) microscopy to enhance the contrast of microscope images. Here, the incoming light is sent through an aperture, for instance a ring, and focused onto the sample. The transmitted or reflected light is then sent through the inverse aperture, for instance a circular hole. Thus, the image is essentially black when no scattering on the sample occurs. The light scattered, for example, by a metallic nanoparticle is detected and analyzed. By this technique, similar to attenuated-total-internal-reflection spectroscopy, we gather only qualitative information about the scattering cross-section.
- (iii) Transmission of strongly focused laser beams: a laser beam is strongly focused by a solid immersion lens such that the extinction cross-section covers a considerable part of the focus area. This technique has been applied for measuring the optical properties

⁶Chromex 250i, Chromex Inc., Albuquerque (USA), now: Bruker Optik GmbH

⁷LN CCD-1340/400-EHR, Princeton Instruments, Trenton (USA)

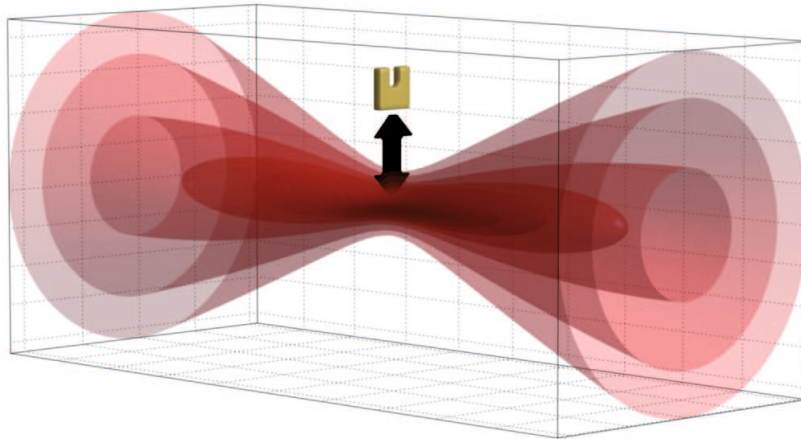


Figure 5.2: Illustration of the modulation spectroscopy technique: A small particle, here an SRR, is placed in the focal plane of a Gaussian beam. The iso-intensity contours of the Gaussian beam are visualized by the red lobes. Either the SRR or the Gaussian beam is spatially modulated. The modulation leads to a modulated signal that is analyzed by a lock-in technique.

of single molecules [99], single quantum dots, and single gold spheres being several nanometers in diameter [100].

Unfortunately, both attenuated-total-internal-reflection and dark-field spectroscopy do not provide quantitative information about the scattering strength. Nevertheless, they are fast and efficient in measuring the resonance position and the resonance width of nanoparticles. The method described in Ref. [99] is not suitable for spectroscopy on our photonic atoms: due to the high numerical aperture, the illumination in the focus will vary substantially over the area covered by the photonic atom and also the exciting fields are not necessarily transverse.

Spatial modulation spectroscopy In this work, we apply a spatial modulation technique [101, 102] to obtain quantitative information about the absolute extinction cross-section of isolated photonic atoms. We focus a laser beam onto a sample which is then periodically modulated in and out of the focus (alternatively, we modulate the focus over the sample) as sketched in Fig. 5.2. The modulation results in a modulated transmitted intensity that is analyzed by a lock-in technique. The data from the lock-in amplifier together with quantitative experimental knowledge of the width w_0 of the Gaussian focus (see section 2.5) and the spatial modulation amplitude then allow to infer the absolute extinction cross-section and its spectral dependence $C_{\text{ext}}(\lambda)$ directly from an experiment. Modulation techniques are known for being very sensitive and for very effectively increasing the signal-to-noise ratio. For instance, the so-called frequency modulation technique has been utilized as a sensitive tool for investigating optical properties of molecules and atoms [103].

The spatial modulation technique has been presented for the first time in Ref. [101] by Arbouet *et al.*. In this work, the authors have used a continuous-wave laser allowing for measuring the absolute extinction cross-section at a fixed wavelength ($0.532 \mu\text{m}$). In Ref. [102], the same group has extended the setup by using a supercontinuum light source allowing for

spectroscopy on isolated nanoparticles.

5.3.1 A small particle in a Gaussian focus

In this section, we derive the relation between the relative transmitted power ($\Delta T/T$), that is, the quantity supplied by the lock-in amplifier, and the extinction cross-section [104, 105]. Thus, we first address the question, how a small particle in a Gaussian focus alters the transmitted power. We provide all details of the calculations in appendix B.1.

A Gaussian beam is defined by the quantities given in section 2.5: the width w_0 , the Rayleigh length z_R , the Gouy phase $\varphi_G(z)$, and the wave front curvature $R(z)$. To express the power P_0 of the Gaussian beam by these quantities, we additionally need to know the electric field in the far-field region, that is, at $z \gg z_R$. We assume that the divergence of the beam is very small, *i.e.*, the numerical aperture of the beam NA_B is much smaller than one ($\text{NA}_B \ll 1$). In this case, we find for the Gouy phase $\varphi_G \approx \pi/2$, for the width $w(z) \approx \frac{w_0}{z_R}z$, for the curvature radius of the wave fronts $R(z) \approx z$, and for the opening angle $\theta = \rho/z$ (remember, $\rho = \sqrt{x^2 + y^2}$, where x and y denote Cartesian coordinates). The electric field in the far field then reads

$$\mathbf{E}_i(\theta, z) \approx \mathbf{E}_0 \frac{z_R}{iz} \exp\left(-\frac{\theta^2}{\text{NA}_B^2}\right) \exp\left[ikz\left(1 + \frac{\theta^2}{2}\right)\right]. \quad (5.1)$$

In the far field, the Gaussian beam resembles a spherical wave very well, as we already discussed in section 2.5. Thus, we switch to spherical coordinates with r , θ , φ and assume $z \approx r$ and $\theta^2/2 \ll 1$ from $\text{NA}_B \ll 1$. For the far-field distribution, we obtain

$$\mathbf{E}_i(\theta, r) \approx \mathbf{u}_{xz} E_0 \frac{z_R}{ir} \exp\left(-\frac{\theta^2}{\text{NA}_B^2}\right) \exp(ikr). \quad (5.2)$$

Here, $r = \sqrt{x^2 + y^2 + z^2}$ is the radial coordinate and \mathbf{u}_{xz} determines the direction of the electric far field; we assume that the beam is x -polarized in the focus and consequently in the far field the polarization is given by $\mathbf{u}_{xz} = \cos\theta\mathbf{u}_x + \sin\theta\mathbf{u}_z$. For the detection of the transmitted power, we use a combination of an objective lens and a diode detector. The numerical aperture NA_D of this combination is assumed to be larger than the numerical aperture of the beam NA_B but still smaller than one, in short $\text{NA}_B \ll \text{NA}_D \ll 1$. For the experiment, this means that the beam should not completely fill the entrance aperture of the microscope objective lens. The detected power of the Gaussian beam in terms of the beam parameters reads

$$\begin{aligned} P_0 &= \int_{\theta < \text{NA}_D} d\Omega r^2 \frac{1}{2} \text{Re}(\mathbf{E}_i \times \mathbf{H}_i^*) \cdot \mathbf{u}_r \\ &\approx \frac{\pi z_R^2 E_0^2}{4\mu_0 c} (\text{NA}_B)^2, \end{aligned} \quad (5.3)$$

where we used $\mathbf{H}_i = \frac{\mathbf{u}_r \times \mathbf{E}_i}{\mu_0 c}$ and $\sin\theta \approx \theta$. Additionally, we assume that the electric field decays very fast along θ allowing for increasing the upper boundary of the integral to infinity.

In analogy to the treatment of the interaction of a plane wave with a small particle in section 2.1.5, we calculate the power reaching the detector when a particle is placed in the Gaussian focus

$$P_{\text{part}} = \int_{\theta < \text{NA}_D} d\Omega r^2 \frac{1}{2} \text{Re} [(\mathbf{E}_i + \mathbf{E}_s) \times (\mathbf{H}_i + \mathbf{H}_s)^*] \cdot \mathbf{u}_r, \quad (5.4)$$

where E_s is given by Eq. (2.22). For the signal drop being the power extinguished from the beam, we find

$$\begin{aligned} \Delta P &= P_0 - P_{\text{part}} \\ &= - \int_{\theta < \text{NA}_D} d\Omega r^2 \frac{1}{2} \text{Re} (\mathbf{E}_i \times \mathbf{H}_s^* + \mathbf{E}_s \times \mathbf{H}_i^* + \mathbf{E}_s \times \mathbf{H}_s^*) \cdot \mathbf{u}_r. \end{aligned} \quad (5.5)$$

In the following, we neglect the term $\mathbf{E}_s \times \mathbf{H}_s^*$ since we assume the scattered field \mathbf{E}_s to be small compared to \mathbf{E}_i . With \mathbf{E}_s given by Eq. (2.22) and \mathbf{E}_i by Eq. (5.1), the extinguished power reads

$$\Delta P = \frac{z_R E_0^2}{k c \mu_0} \int_{\theta < \text{NA}_D} d\Omega \exp\left(-\frac{\theta^2}{\text{NA}_B^2}\right) \text{Re} [\mathbf{X}(\theta, \varphi) \cdot \mathbf{u}_{xz}]. \quad (5.6)$$

For dipole scattering, the radiated power varies little with the angle. Thus, we can evaluate the vector-scattering amplitude in forward direction and assume that it is constant, *i.e.*, $\text{Re} [\mathbf{X}(\theta, \varphi) \cdot \mathbf{u}_x] = \text{Re} [\mathbf{X}(\theta = 0) \cdot \mathbf{u}_x] = \text{const.}$. Analogous to Eq. (5.3), we find

$$\begin{aligned} \Delta P &\approx 2\pi \frac{z_R E_0^2}{k c \mu_0} \text{Re} [\mathbf{X}(\theta = 0) \cdot \mathbf{u}_x] \int_{\theta < \text{NA}_D} d\theta \exp\left(-\frac{\theta^2}{\text{NA}_B^2}\right) \\ &\approx \frac{z_R E_0^2}{k c \mu_0} \pi \text{NA}_B^2 \text{Re} [\mathbf{X}(\theta = 0) \cdot \mathbf{u}_x]. \end{aligned} \quad (5.7)$$

As already discussed, we do not measure the signal drop ΔP but the relative signal drop

$$\frac{\Delta P}{P_0} = \frac{4}{k z_R} \text{Re} [\mathbf{X}(\theta = 0) \cdot \mathbf{u}_x]. \quad (5.8)$$

Similar to the extinction cross-section in the Optical Theorem (see section 2.1.5), the signal drop is directly proportional to the real part of the projected vector-scattering amplitude. Precisely, the Optical Theorem reads $C_{\text{ext}} = \frac{4\pi}{k^2} \text{Re} [\mathbf{X}(\theta = 0) \cdot \mathbf{u}_x]$. Thus, we can write the extinction cross-section in terms of the relative signal drop

$$C_{\text{ext}} = \frac{\pi w_0^2}{2} \frac{\Delta P}{P_0}. \quad (5.9)$$

Equation (5.9) allows for deducing the absolute value of the extinction cross-section from the measured quantity, which is the relative signal drop caused by a small particle in the focal spot of a Gaussian beam.

5.3.2 A small particle outside a Gaussian focus

We learned in the previous section that the extinction cross-section can be calculated from the relative signal drop caused by a small scatterer. We have to keep in mind that this signal drop can only be obtained when the scatterer is moved from the focal spot to a position far away from the focal spot where no field is present. In our spatial modulation technique, we sinusoidally move the particle along one axis (equivalently, we move the beam). The signal is then analyzed by a lock-in technique, that is, we record the signal all the time and essentially Fourier transform the recorded signal. Additionally, we perform a 2D scan in the focal plane and measure at each pixel the signal from the lock-in amplifier. Thus, in the following, we calculate the signal drop when the particle is located within the focal plane but not in the focus, that is, at $\rho = R$ and $z = 0$. Again, we provide all details in appendix B.2.

With the particle somewhere in the focal plane, there are two mechanisms leading to a modification of the extinguished power given by Eq. (5.7):

- (i) The electric field strength exciting the particle is modified according to Eq. (5.2). The corresponding correction factor reads

$$m_1(R) = \exp \left[- \left(\frac{R}{w_0} \right)^2 \right]. \quad (5.10)$$

- (ii) The detected power results from the far-field interference of the scattered and the incident wave. Clearly, the interference is affected by a phase difference $\Delta\phi$ between scattered and incident wave. Thus, the interference pattern strongly depends on the position of the small particle. The phase difference reads $\Delta\phi = kR \sin \theta \cos \varphi \approx kR\theta \cos \varphi$. For the correction factor, we find

$$\begin{aligned} m_2(R) &= \frac{2}{\pi \text{NA}_B} \int_0^\infty \theta \exp \left[- (\theta/\text{NA}_B)^2 \right] d\theta \int_0^\pi \cos(kR\theta \cos \varphi) d\varphi \\ &= 2 \int_0^\infty \alpha \exp(-\alpha^2) J_0(kR\alpha \text{NA}_B) d\alpha, \end{aligned} \quad (5.11)$$

where $J_0(x) = \frac{1}{\pi} \int_0^\pi \cos(x \cos \varphi) d\varphi$ is the Bessel function of the first kind and zeroth order [41] and $\alpha = \frac{\theta}{\text{NA}_B}$. Expressing J_0 in a Taylor series yields

$$m_2(R) = \exp \left[- \left(\frac{R}{w_0} \right)^2 \right] = m_1(R). \quad (5.12)$$

In summary, we find for the modified extinguished power

$$\Delta P_m = m_1(R)m_2(R)\Delta P = \exp \left[-2 \left(\frac{R}{w_0} \right)^2 \right] \Delta P. \quad (5.13)$$

As a consistency check, we find that the prefactor becomes 1 for $R = 0$. Essentially, Eq. (5.13) shows that the off-axis signal drop is proportional to the lateral (Gaussian) intensity profile.

5.3.3 Connection to the experiment

In the experiment, the detected modulated power is converted by the combination of the detector system (diode detector and objective lens) and the low-noise current pre-amplifier into a modulated voltage $U[x, y(t)]$, here, x and y denote the position of the scatterer in the focal plane. We modulate the sample (or equivalently the beam) along the y -axis. The modulation is harmonic around a central position y , the frequency is ν , and the amplitude a_0 . Thus, we obtain for the detected voltage $U[x, y + a_0 \cos(2\pi\nu t)]$, where t denotes the time. In the following, we use $\omega = 2\pi\nu$.

In this section, we discuss how to deduce the extinction cross-section from the experimental data [104, 105]. We know from Eq. (5.13), that the signal drop is Gaussian when moving the particle in the focal plane. Thus, also the voltage $U(x, y)$ from the detector system is Gaussian

$$U[x, y(t)] = U_0 \left\{ 1 - \sigma \exp \left[-2/w_0^2 (x^2 + [y + a_0 \cos(\omega t)]^2) \right] \right\}, \quad (5.14)$$

where U_0 is the detector signal generated by the undisturbed Gaussian beam [see Eq. (5.3)], $\sigma = \Delta U/U_0 = \Delta P/P_0 \ll 1$ is related through Eq. (5.9) to the extinction cross-section. Here, we already introduced the spatial modulation $a_0 \cos(\omega t)$ along the y -axis.

In order to enhance the sensitivity and to reduce the noise, we use a lock-in amplifier, that essentially yields the Fourier transformation of the input voltage $U[x, y(t)]$. Additionally, we have to take into account that the output voltage of the lock-in amplifier is not the amplitude of the modulated input voltage, but its root-mean-square divided by the sensitivity U_{Sens} of the lock-in amplifier and multiplied by 10 V. We account for this modification by the prefactor $F = \frac{10 \text{ V}}{\sqrt{2} U_{\text{Sens}}}$. Thus, the output voltage of the lock-in amplifier reads

$$\begin{aligned} U_{\text{LI}}(x, y) &= F \frac{\omega}{\pi} \int_0^{2\pi/\omega} U[x, y + a_0 \cos(\omega t)] \cos(\omega t) dt \\ &= F \frac{1}{\pi} \int_0^{2\pi} U[x, y + a_0 \cos(\beta)] \cos(\beta) d\beta. \end{aligned} \quad (5.15)$$

The lock-in-amplifier output voltage $U_{\text{LI}}(x, y)$ is depicted in Fig. 5.3(a). The chosen parameters correspond to our experimental parameters used with the Gaussian focus located at $x, y = 0$. A maximum and a minimum appear symmetric to the $y = 0$ -axis. At $x = y = 0$, the lock-in signal is zero since the small particle does not lead to a power modulation at the modulation frequency but at twice the modulation frequency. Thus, if we change the lock-in frequency from ω to 2ω , we obtain a maximum at the origin.

In the following, we discuss how we deduce the extinction cross-section from the experimental data, which are numerically reproduced in Fig. 5.3(a). With the Fourier transformation of the input voltage [see Eq. (5.14)] $\tilde{U}(x, k) = 1/\sqrt{2\pi} \int_{-\infty}^{\infty} \exp(-iky) U(x, y) dy$ and the Bessel function of the first kind and first order $J_1(x) = -i/\pi \int_0^\pi \exp(ix \cos \varphi) \cos(\varphi) d\varphi$ [41], we

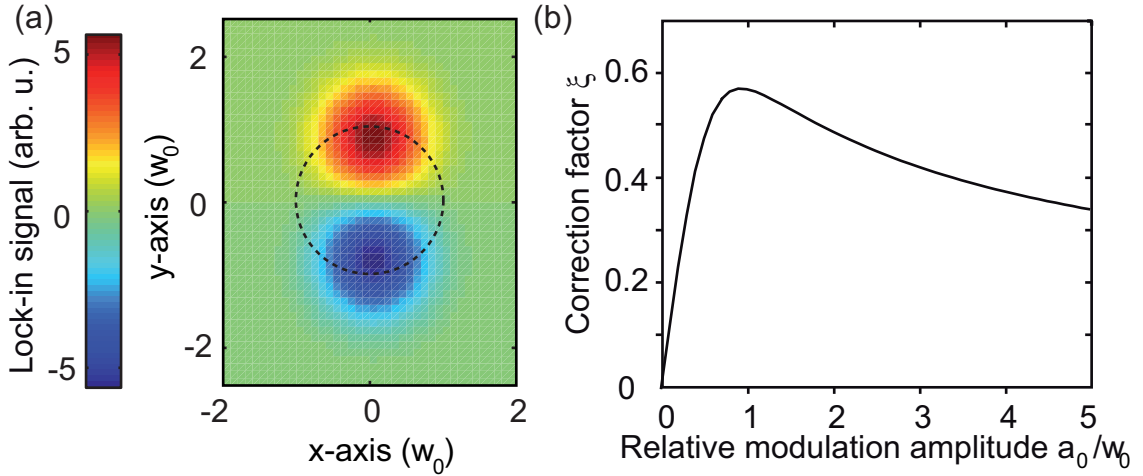


Figure 5.3: (a) Lock-in signal plotted as a function of the small particle's position. The dotted circle corresponds to the beam waist of the Gaussian focus. (b) Correction factor ξ plotted over the relative modulation amplitude.

can rewrite Eq. (5.15)

$$\begin{aligned}
 U_{\text{LI}}(x, y) &= F \frac{1}{\pi\sqrt{2\pi}} \int_0^{2\pi} \cos \beta d\beta \int_{-\infty}^{\infty} \tilde{U}(x, k) \exp [ik (y + a_0 \cos \beta)] dk \\
 &= F \sqrt{\frac{2}{\pi}} \int_{-\infty}^{\infty} \exp(iyk) \tilde{U}(x, k) J_1(ka_0) dk.
 \end{aligned} \tag{5.16}$$

In combination with the Fourier transform $\tilde{U}(x, k)$ of Eq. (5.14), Eq. (5.16) allows for an analytical relation between the output voltage of the lock-in amplifier and the signal drop. $\tilde{U}(x, k)$ explicitly reads

$$\begin{aligned}
 \tilde{U}(x, k) &= -\frac{U_0 \sigma \exp(-2x^2/w_0^2)}{\sqrt{2\pi}} \int_{-\infty}^{\infty} \exp(-2y^2/w_0^2) \exp(-iky) dy \\
 &= -\frac{1}{2} U_0 \sigma \exp(-2x^2/w_0^2) w_0 \exp(-k^2/8w_0^2).
 \end{aligned} \tag{5.17}$$

With Eqs. (5.16) and (5.17) and with $\sigma = \Delta U/U_0$, we obtain

$$U_{\text{LI}}(x, y) = F \Delta U \exp(-2x^2/w_0^2) \underbrace{\frac{w_0 i}{\sqrt{2\pi}} \int_{-\infty}^{\infty} \exp(-k^2/8w_0^2) \exp(iky) J_1(ka_0) dk}_{=\kappa(y, a_0/w_0)}. \tag{5.18}$$

Here, we define the modification factor $\kappa(y, a_0/w_0)$.

Equation (5.18) connects the signal from the lock-in amplifier with the signal drop. Thus, it allows us to deduce the extinction cross-section from the experimental data (that is, the relative differential signal $\text{RDS}(x, y) = \frac{U_{\text{LI}}(x, y)}{U_0 F}$) if we know the exact location of the small particle with respect to the Gaussian beam. Thus, in the experiment, we perform a 2D scan over the sample in order to find the maximum of the relative differential signal $\text{max}_{2\text{D}} [\text{RDS}(x, y)]$,

which is related to extinction cross-section by

$$C_{\text{ext}} = \frac{\pi w_0^2 \max_{2\text{D}} [\text{RDS}(x, y)]}{2 \xi(a_0/w_0)}. \quad (5.19)$$

Here, $\xi(a_0/w_0) = \max_y [\kappa(y, a_0/w_0)]$ is the factor correcting for the application of the lock-in technique in combination with the Gaussian intensity profile and the sinusoidal modulation. It also accounts for using the maximum of the $\text{RDS}(x, y)$ to determine the extinction cross-section instead of any other point in the 2D scan.

The correction factor $\xi(a_0/w_0)$ is plotted in Fig. 5.3(b) as a function of the relative modulation amplitude a_0/w_0 . For $a_0/w_0 \ll 1$, the correction factor $\xi(a_0/w_0)$ increases linearly, approaching a maximum of $\xi \approx 0.58$ for $a_0/w_0 \approx 0.9$ and decreases thereafter. We observe a maximum in the RDS for a given extinction cross-section, since for larger and larger modulation amplitudes, the time the small particle is located in the Gaussian focus becomes shorter and shorter with respect to the period of the modulation. Thus, for both zero and infinite modulation amplitude, we expect zero output voltage from the lock-in amplifier.

To summarize: in order to obtain the extinction-cross-section spectrum, for each wavelength (i) we determine the correction factor $\xi(a_0/w_0)$ by measuring the width w_0 of the Gaussian beam in the focus (the modulation amplitude a_0 is usually fixed) and (ii) we determine the maximum of the 2D map of the measured RDS data [illustrated in Fig. 5.3(a)]. In detail, finding the maximum is done by fitting the measured data to Eq. (5.18).

Finally, we point out that the spatial modulation technique allows for measuring extinction-cross-section spectra $C_{\text{ext}}(\lambda)$, if we know the radius of the Gaussian beam waist w_0 and the spatial modulation amplitude a_0 . Furthermore, we have to ensure that the small particle is always located in the focal plane.

5.3.4 Experimental setup

The experimental modulation setup is shown in Fig. 5.4. As light source, we use a photonic-crystal-fiber based super continuum laser⁸ with an overall output power of 2 W, which is distributed in the wavelength range from 0.45 μm to 2.2 μm . The output facet of the laser fiber is imaged onto the entrance slit of a monochromator⁹. In order not to destroy the entrance slit, we lower the beam power by a factor of five by means of using a reflection from a tilted glass surface. The monochromator is set to a resolution of about 1 nm-wavelength at a center wavelength of 1.5 μm . The exit of the monochromator is connected to a single-mode fiber¹⁰ serving as spatial filter. Thus, the light from the fiber resembles a TEM_{00} -mode [55]. After the fiber, the power is usually about 100 nW. The light from the single-mode fiber is collimated by a plano-convex lens ($f = 25$ mm). We choose a specific linear polarization by a polarizer. Subsequently, the light beam is reflected by a piezo-electric mirror¹¹ through

⁸Femtopower 1060 Supercontinuum Source SC 450, Fianium Ltd., Southampton (UK)

⁹SpectraPro-2150i, Acton Research Corp., Acton (USA)

¹⁰1060-XP Single-Mode Fiber, Nufern Corp., East Granby (USA)

¹¹S-224 High-Speed Miniature Piezo Tilt Mirror, Physik Instrumente (PI) GmbH & Co. KG, Karlsruhe / Palmbach (Germany)

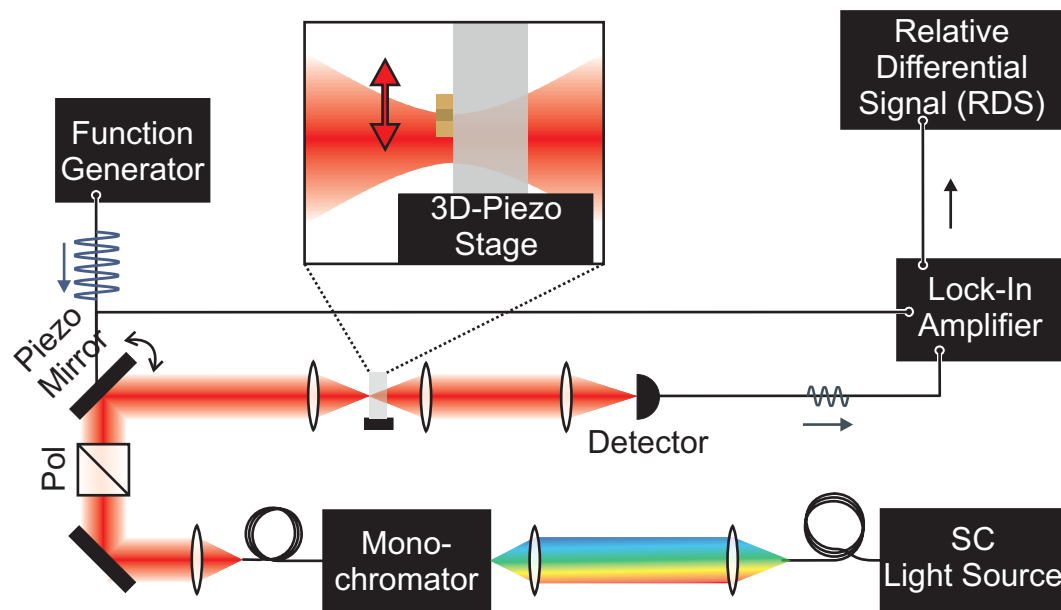


Figure 5.4: Scheme of the experimental modulation setup.

an objective lens¹² which focuses the beam onto the sample surface. The position of the sample is computer controlled by a 3D piezo-stage¹³. The light is collected by an identical objective lens and imaged onto a detector. The detector is either a room-temperature germanium diode¹⁴ or a room-temperature indium gallium arsenide diode¹⁵ for the spectral range between 1.0 μm and 1.6 μm wavelengths. The detector is connected to a low-noise current pre-amplifier¹⁶ whose amplification is set to 100 nA/V and 10 $\mu\text{A}/\text{V}$ for 120 Hz and 4000 Hz modulation frequency in order to circumvent the low-pass filter of the amplifier.

The tilt angle of the piezo-electric mirror is controlled by a function generator¹⁷ that applies a modulation voltage of 15 V which is superimposed on the offset voltage of 50 V. The slight tilt of the beam alters the position of the focus on the sample surface [55] by 1.5 μm resulting in a modulated detected signal (in an earlier version of the experimental setup, we have modulated the sample by a piezoelectric transducer [105]). The modulated signal is analyzed by a lock-in amplifier¹⁸. The lock-in integration time is set to 100 ms and 30 ms for 120 Hz and 4000 Hz, respectively. These times have been chosen after several test experiments. With the position information from the piezo-stage, we obtain a 2D map of the position-resolved RDS. It turned out that a settling time at each pixel of about $2.5 \times$ integration time is sufficient for obtaining reproducible results. The 2D map is then further analyzed as discussed in the previous sections.

¹²Zeiss Achroplan LD 20 \times KO, NA = 0.4, Carl Zeiss MicroImaging GmbH, Jena (Germany)

¹³P-563.3CD PIMarsTM Nanopositioning Stage, Physik Instrumente (PI) GmbH & Co. KG, Karlsruhe / Palmbach (Germany)

¹⁴J16-5SP-R03M, Teledyne Judson Technologies LLC, Montgomeryville (USA)

¹⁵J22-5I-R02M, Teledyne Judson Technologies LLC, Montgomeryville (USA)

¹⁶SR570 Low-Noise Current Pre-Amplifier, Stanford Research Systems Inc., Sunnyvale (USA)

¹⁷33120A 15MHz Function/Arbitrary Waveform Generator, Hewlett-Packard Co., Palo Alto (USA)

¹⁸SR830 DSP Lock-In Amplifier, Stanford Research Systems Inc., Sunnyvale (USA)

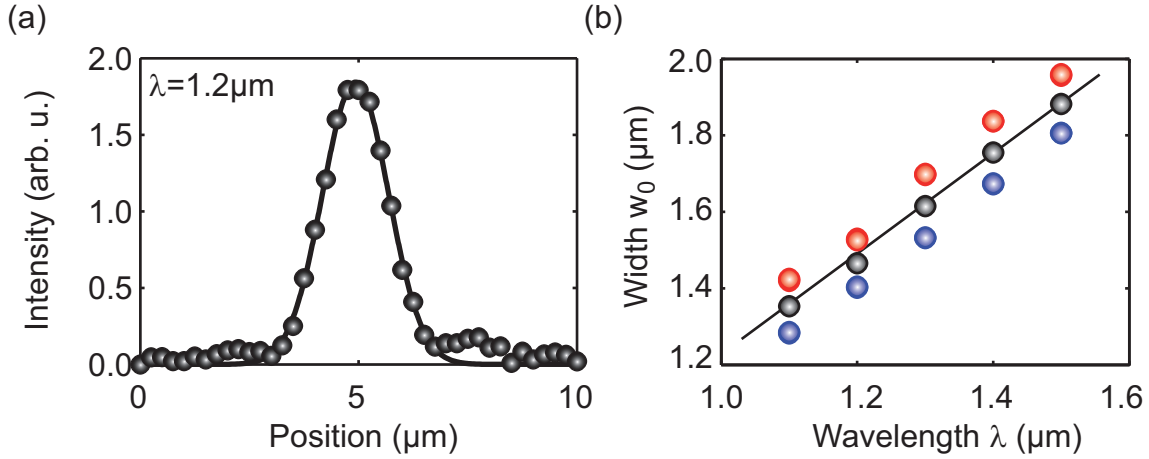


Figure 5.5: (a) Measured spatial intensity distribution of the Gaussian beam for a wavelength of $\lambda = 1.2 \mu\text{m}$ at $z = z_0$. The dots are deduced from measured intensities, whereas the solid line is the Gaussian fit [see Eq.(2.106)] to the data. (b) Width (w_0) of the Gaussian beam for different wavelengths measured in two directions. There is a difference between the width measure in x -(blue) and y -(red) direction. For analyzing the data, we use the mean value (black). The dots stem from measurements like the one shown in (a). Note that each red and blue dot in (b) displays two measured focus widths. The black solid curve is a linear fit to the measured data we use for calculating the extinction cross-section from the measured RDS.

The width w_0 of a Gaussian beam for $1.2 \mu\text{m}$ -wavelength measured by the knife-edge technique is depicted in Fig. 5.5(a): the dots are derived from measured intensities. The black solid curve is a Gaussian fit to the measured data. Clearly, the width of the Gaussian beam is a function of the wavelength. For larger wavelengths, we expect larger widths for the same numerical aperture. This behavior is also found in our experiment as illustrated in Fig. 5.5(b): we measure different widths in the x - and the y -direction (blue and red curve, respectively). For the analysis discussed in section 5.3.3 we take a linear fit (black solid curve) to the mean values (black dots). Examples of resulting sets of raw data are shown in Fig. 5.6. As expected from Refs. [101, 102] and our analysis presented in section 5.3.3, we find a maximum and a minimum in the differential transmittance signal. For these data, the modulation amplitude has been fixed at $a_0 = 3 \mu\text{m}$. The 2D scan on the right-hand side is measured at resonance of an SRR (see section 7.1) whereas the 2D scan on the left-hand side is measured in the tail of the resonance giving an impression of the occurring noise in the data.

5.3.5 Sample design

In order to locate the photonic atom [size: $\approx (100 \times 100) \text{ nm}^2 = 10^4 \text{ nm}^2$] on the Suprasil substrate [size: $\approx (1 \times 1) \text{ cm}^2 = 10^{14} \text{ nm}^2$], we have developed a special sample design, see Fig. 5.7(a). It does not only allow for locating the photonic atom but also for experimentally determining the focus position z_0 and the Gaussian beam waist w_0 with the help of the knife-edge technique. That is, we perform lateral scans of a knife-edge [in our case a metallic rectangle, see Fig. 5.7(a)] through the Gaussian beam. The lateral scans are carried out along the x - or y -axis at a fixed longitudinal position z . The recorded intensity resembles an error

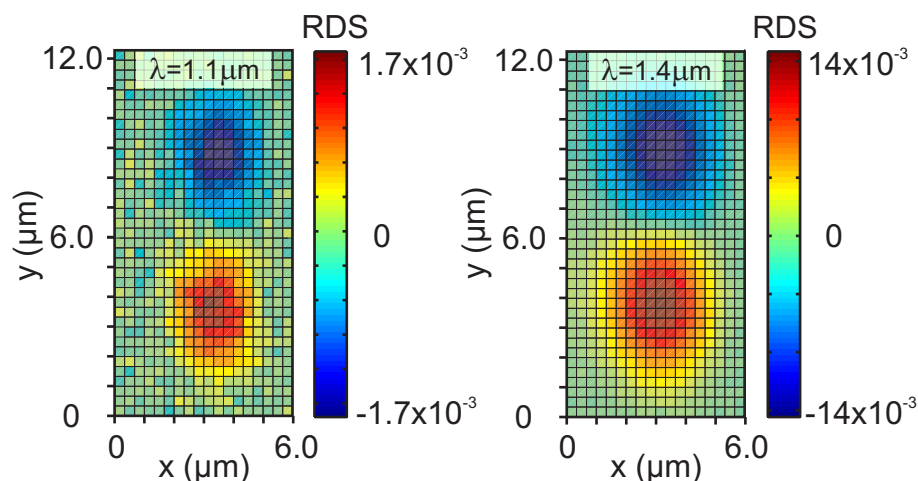


Figure 5.6: Two typical sets of raw data of the measured RDS. Left-hand side: off-resonant excitation [$C_{\text{ext}}(\lambda = 1.1 \mu\text{m}) = 0.03 \mu\text{m}^2$]. Right-hand side: resonant excitation [$C_{\text{ext}}(\lambda = 1.4 \mu\text{m}) = 0.29 \mu\text{m}^2$].

function from which we determine the beam waist $w(z)$. This procedure is carried out at several z -positions supplying quantitative information about the beam waist in the focus w_0 , the Rayleigh length z_R , and the focus position z_0 . w_0 is required for the determination of the absolute value of the extinction cross-section as discussed in section 5.3.3 and z_0 is required for ensuring that the particle is located in the focal plane. Our knife-edges are large enough (about $25 \mu\text{m} \times 25 \mu\text{m}$) for being visible by a simple imaging add-on attached to the setup shown in Fig. 5.4 (the imaging add-on is not shown). The photonic atoms which we want to locate on the sample are situated at a known position with respect to the corners of the rectangles.

5.4 Electron-energy-loss spectroscopy of isolated photonic atoms

Electron-energy-loss spectroscopy (see section 2.4) utilizes high-energy electrons (the kinetic energy is 100 keV) for probing electronic and optical properties at the nanometer scale. Some of the electrons that interact with the specimen are inelastically scattered by exciting phonons and plasmons or by inducing electronic transitions like interband transitions in solids. In this work, we use EELS for mapping particle plasmons on isolated lithographically defined metallic nanostructures. Related work on self assembled metallic nanostructures has been reported very recently in Refs. [49, 106–108].

In this section, we introduce the setup we use for EELS. Furthermore, we present the applied numerical analysis of the raw data, which is required due to the sub-optimal energetic resolution of conventional EELS. Experiments and numerical analysis have been carried out by our collaborators G. Boudarham, M. Kociak, and C. Colliex in the group of O. Stéphan in Paris, France.

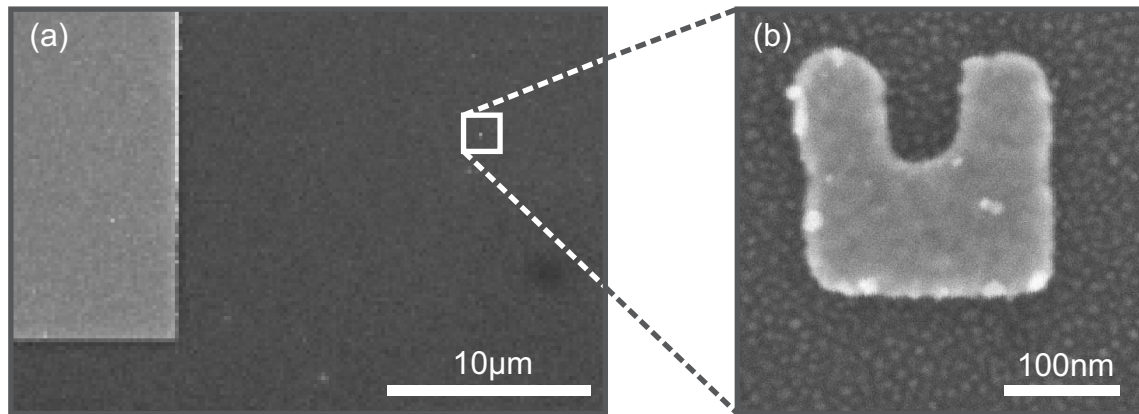


Figure 5.7: Electron micrographs of a typical sample depicting (a) the knife-edges and (b) a zoom-in to the SRR located at a known distance from the knife-edges.

5.4.1 Experimental setup

In our EELS experiments, we use a VG-HB501 scanning-transmission-electron microscope (STEM)¹⁹ equipped with home-made scanning and detection electronics. The STEM is capable of focusing the electron beam below 1 nm in diameter that functions as a probe of the same size. Such a small probe provides superior spatial resolution in comparison to all optical methods, as for instance scanning near-field microscopy [109] or stimulated emission depletion microscopy [110]. For completeness, we list another electron-microscope-based spectroscopy method: cathodoluminescence spectroscopy [111]. Here, similar to EELS, fast electrons excite modes in the system. The luminescence of the radiating excited modes is detected and analyzed by means of an optical spectrometer and an attached detector.

In EELS, we aim for detecting inelastic scattering events: the electrons passing through the specimen lose a small fraction of their energy. This energy is converted into excitations of the constituting atoms and molecules – in our case we aim for collective excitations of the free-electron gas (particle plasmons) in isolated metallic photonic atoms.

Since the electrons have to pass through the specimen, its thickness has to be well below 1 μm . Thus, we can not fabricate the photonic atoms on a usual substrate whose thickness is between 100 μm and 1 mm. For our experiments, we use so-called Si_3N_4 -membranes whose thickness is about 30 nm. Accordingly, we had to modify our electron-beam-lithography based fabrication technique as explained in detail in section 4.1.6.

In the experimental setup, illustrated in Fig. 5.8, we use a conventional STEM. The electrons are generated in a cold field-emission tungsten gun (CFEG) allowing for an energy uncertainty of the electron beam of about $\Delta E_0 = 0.35 \text{ eV}$ at a mean kinetic energy of $E_0 = 100 \text{ keV}$ without any further filtering by means of an electron monochromator. The energetic width is mainly governed by those electrons that have not, or not in a measurable fashion inelastically interacted with the sample. This leads to the so-called zero-loss peak (ZLP) of the same width in the electron-energy-loss spectrum. An elaborated numerical analysis of the recorded spectra allows to achieve an energy resolution down to $\Delta E_0 = 0.2 \text{ eV}$ [49].

¹⁹VG-HB501, VG Microscopes Ltd., East Grinstead (UK), now Thermo Scientific

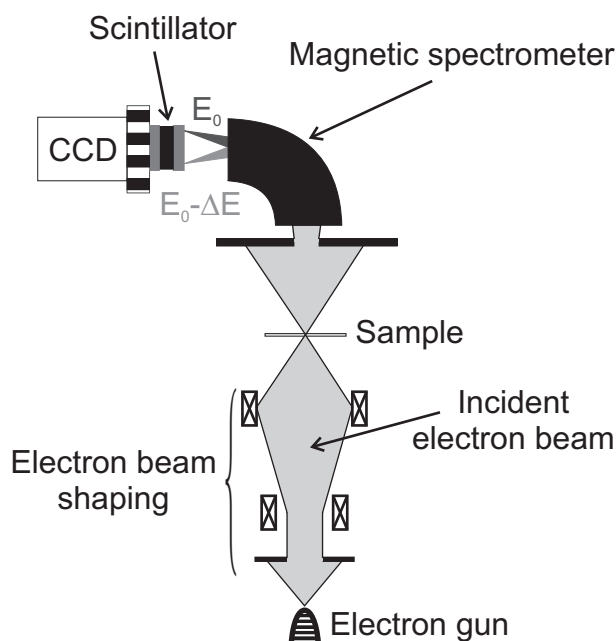


Figure 5.8: Experimental setup for electron-energy-loss spectroscopy.

An important feature of the CFEG is its high brightness (current per unit area and unit solid angle) compared to other gun types allowing for reasonably short measurement times. The electron beam is tightly focused onto the sample by electromagnetic lenses with a beam convergence half angle set to about 7.5 mrad. With these settings, we scan the electron beam over the specimen. Subsequently, the electrons are collected within a half angle limited to 6 mrad by using a 600 μm -aperture. The electrons are energetically discriminated after passing through the sample by means of an electron spectrometer²⁰ providing a maximum dispersion of 0.05 eV per channel. After the electron spectrometer, the electrons impinge onto a scintillator. The luminescence is recorded by a CCD camera with 1340×100 pixels. The position of the electrons on the CCD camera is directly related to their kinetic energy. Scanning the electron beam over the sample results in a 2D plot of the electron-energy-loss probability for a specific electron-energy loss ΔE . The probability is related to the electromagnetic local density of states as discussed in section 2.4. For each lateral position of the electron beam, we obtain an entire electron-energy-loss spectrum leading to a so-called data cube [112] with two dimensions carrying the spatial information and the third dimension carrying the spectral information. Out of this huge amount of data, we focus on slices through the data cube (meaning 2D plots of a particular electron-energy loss ΔE) where we observe resonances in the energy-loss spectrum.

Some remarks regarding the EELS experiment

- Spatial resolution: we typically set the spatial resolution (the step size) to 6 nm. This is larger than the probe but still small enough to resolve all features of the particle

²⁰Gatan 666, Gatan Inc., Warrendale (USA)

plasmon oscillating at frequencies in the near-infrared to visible spectral range. Furthermore, it allows for reasonable measurement times (see below).

- Acquisition time: the acquisition time is 2 ms per position – without readout time. The acquisition time per position is chosen in order to minimize artifacts caused by the power supply, mainly due to variations in the acceleration voltage. Thus, the acquisition time per position needs to be much smaller than the period of the *ac*-power supply. Here, the frequency is 50 Hz corresponding to a period of 20 ms. For each position, we acquire 50 spectra in order to increase the dynamic range of the collected data. In total, the time needed for acquiring one entire data cube is about 15 min. Within this time span, the spatial drift is negligible.
- Deposited dose: the current of the STEM is typically 50 pA. Assuming a 2D scan with 32×32 positions, 2 ms-acquisition time per position, and 50 spectra per position, the number of electrons impinging onto the sample is on the order of 10^{10} .

5.4.2 Numerical analysis of the experimental data

Our goal is to map particle plasmons with resonance energies of about 1 eV or even below. Unfortunately, the corresponding energy loss is just a little bit larger than the energetic width of the incident electron beam with $\Delta E_0 = 0.35$ eV. Additionally, only about one out of 10000 electrons excites a particle plasmon [113]. This leads to the uncomfortable situation in which the ZLP masks the low-energy part of the loss spectrum that is associated with the excitation of particle plasmons. Our way out of this dilemma is the application of a sophisticated numerical analysis to the measured raw data [49]. Other groups used electron monochromators to reduce the width of the ZLP down to 0.1 eV [107, 108].

When we measure the spectrum $S(E)$ of a physical system with a detector system exhibiting a non-perfect response function $R(E)$ (also called kernel or point-spread function), the measured signal $M(E)$ is the convolution of $S(E)$ and $R(E)$. Explicitly, we obtain

$$M(E) = \int_{-\infty}^{\infty} S(\varepsilon)R(\varepsilon - E)d\varepsilon = S(E) * R(E), \quad (5.20)$$

where $*$ denotes the convolution. In EELS, $M(E)$ is the measured loss spectrum, $R(E)$ is the ZLP recorded far away from the photonic atom (here, also the response function of the detector system is included). $S(E)$ is the physical data recorded by an ideal detector system (we would directly record $S(E)$ if the response function $R(E)$ were the Dirac-delta distribution). In order to obtain $S(E)$, one deconvolves the recorded data $M(E)$ with the ZLP as kernel. This is usually done by Fourier transforming, rearranging, and back-Fourier transforming Eq. (5.20). Unfortunately, in our case noise $N(E)$ plays a great role, thus we have to extend Eq. (5.20), leading to

$$M(E) = S(E) * R(E) + N(E). \quad (5.21)$$

The usual deconvolution procedure through applying Fourier transformation treats the desired signal $S(E)$ and the noise $N(E)$ equally and thus leads to sub-optimal performance

when the noise is substantial [114]. This is the case when, for instance, the desired part of the loss spectrum is dominated by the ZLP. Then, the noise is basically the detector noise. In our case we can estimate the signal-to-noise ratio from the assumption that one electron out of 10000 excites one particle plasmon and that the dynamic range of the detector is 16 bits (2^{16}) [113]. The expected signal is then six counts and assuming Poisson statistics, the expected signal-to-noise ratio is $\sqrt{6} = 2.4$. This is partially overcome by measuring each spectrum 50 times. Nevertheless, the noise remains substantial. Thus, in EELS a deconvolution algorithm based on maximum likelihood, the so-called Richardson-Lucy-deconvolution (RL) algorithm has proven to be the method of choice for obtaining meaningful physical results [115–117]. For Poisson-distributed noise in the raw data, the RL algorithm converges to the maximum likelihood solution. An important attribute of the RL algorithm is that the restored signal is robust against small errors in the response function (the ZLP). Nevertheless, when applying the RL deconvolution, we have to keep in mind that prominent features in the loss spectrum lead to so-called satellite or wing peaks [114, 118]. Such a prominent feature is the ZLP. Additionally, the RL deconvolution is not unconditionally stable, *i.e.*, noise amplification results in oscillatory artifacts after a large number of iterations. This behavior requires great care in monitoring the procedure and also it has to be terminated manually. The termination decision is based on the profound knowledge of the user and systematic convergence studies. Finally, we compare our results with physical arguments.

The experimentally determined response function $R(E)$ (the ZLP) measured far away from the investigated photonic atom is shown in Fig. 5.9(a). The upper two spectra in Fig. 5.9(b) show the loss spectra of the electron beam after passing through the specimen at a specific location. In the energy loss range $0 \text{ eV} < \Delta E < 5 \text{ eV}$, we expect the occurrence of particle plasmon. Obviously, the signal is strongly dominated by the ZLP. After applying the RL algorithm (terminated after 50 iterations), we obtain the lower loss spectrum shown in Fig. 5.9(b). Here, we nicely observe three different modes (the energetic positions are indicated by the dashed lines) occurring at $\Delta E \approx 1.6 \text{ eV}$, $\Delta E \approx 3.1 \text{ eV}$, and $\Delta E \approx 3.7 \text{ eV}$. In order to obtain a 2D map of the electron-energy-loss probability at specific energy loss, we scan over the sample, take the loss spectrum at each position and apply the above discussed numerical analysis. We fit a Gaussian to each observed peak in the loss spectrum. The amplitude of the fitted Gaussian function is then color coded into a 2D map.

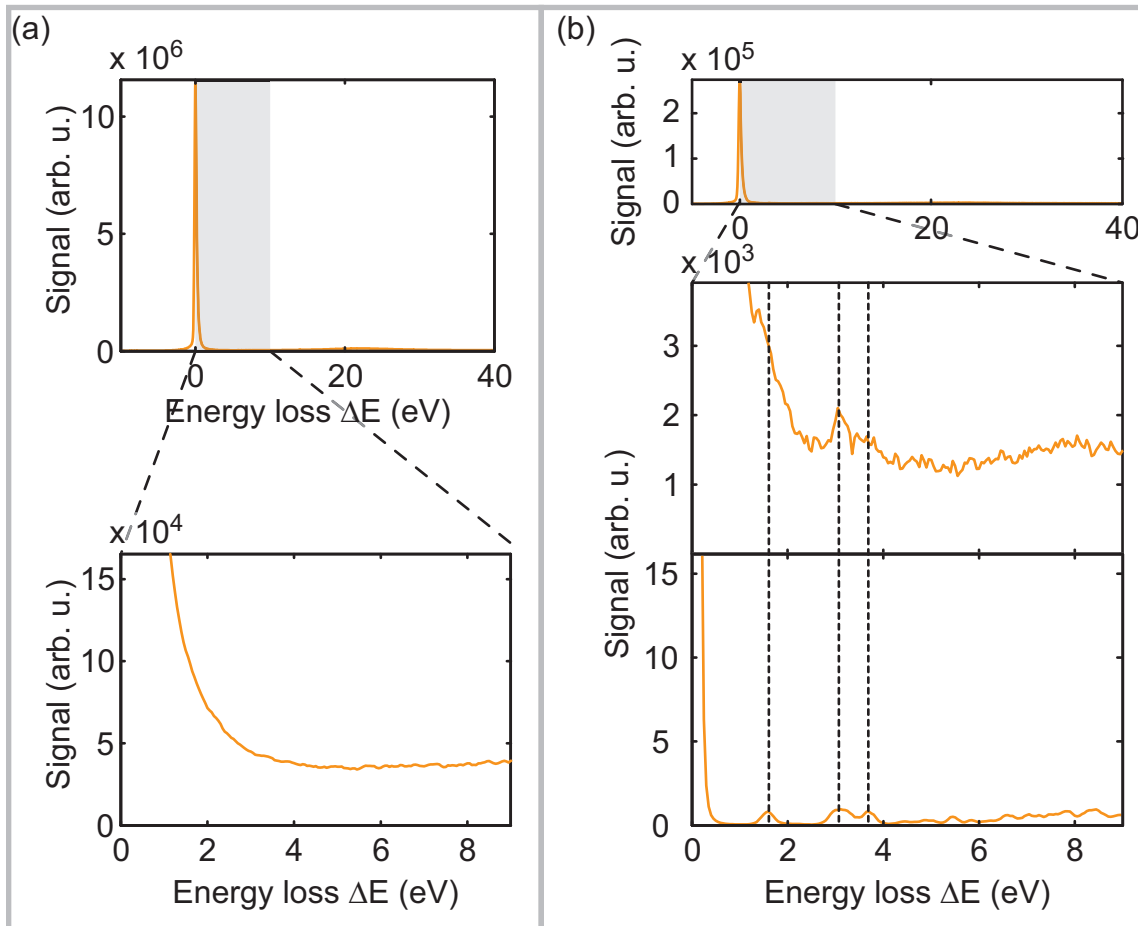


Figure 5.9: (a) Measured zero-loss peak used as response function for deconvolution. The upper spectrum shows the entire ZLP, whereas the lower spectrum shows a zoom-in to the region $0\text{ eV} < \Delta E < 9\text{ eV}$. (b) Experimentally determined loss spectrum measured at a specific location of an SRR. The upper two loss spectra is the EELS signal without numerical post-processing, whereas the lower spectrum is obtained after deconvolution of the original data shown in the upper two loss spectra by the RL algorithm terminated after 50 iterations.

Chapter 6

Nonlinear optical experiments on metamaterial arrays

In the first publication of Pendry *et al.* [4] in which the SRR was set in context with its magnetic dipole moment at elevated frequencies, the authors pointed out that enhanced nonlinear phenomena might be observable due to high electric near fields between the two ends of the SRR.

Hitherto, the nonlinear optical properties of metamaterials in the telecommunication spectral range have hardly been studied on the basis of experiments [16–18, 119]. However, there is a large number of recent theoretical publications addressing the nonlinear optical properties of metamaterials. Most of the work in this context assumes a linear dispersion, for instance a negative refractive index [120] and/or the “new” possibility that there is not only the usual electric-dipole contribution P_{NL} to the nonlinear source term but also a magnetic-dipole contribution M_{NL} [121–123]. Unfortunately, to the best of our knowledge there are only very few publications which rely on a microscopic formulation of the problem [47, 124].

From the experimental side, there is considerable work done on the nonlinear optical properties of metallic nanoparticles. In Refs. [125–127], the investigated metallic nanoparticles are arranged periodically with an interparticle distance being considerably smaller than the exciting wavelength. For instance, in Ref. [125] the wavelength of the exciting light is a factor of 2.5 larger than the periodicity of the investigated nanoparticle array. First systematic investigations of the nonlinear optical properties of SRR arrays are reported in Ref. [16]. As discussed in section 3.3, SRRs are in essence almost closed loops of a metal wire that can be viewed as sub-wavelength electromagnets into which the incident light field induces a resonantly oscillating circular electrical current, leading to a local magnetic field (magnetic dipole moment) perpendicular to the SRR plane.

From Ref. [16], we can learn about the relative SHG intensities from three distinct resonances of SRR arrays (the naming is consistent with the definition in section 3.3.1): (i) the magnetic (fundamental) resonance, (ii) the vertical electric (first-order) resonance, and (iii) the horizontal electric (second-order) resonance. It turns out that the SHG from the magnetic resonance exceeds the SHG of the other resonances by a factor of at least 20. The qualitative results are in accordance to a numerical treatment of the SHG along the lines of

section 2.2.4. In Ref. [16], the dominating second-harmonic source term has been assumed to be the magnetic part of the Lorentz-force density of Eq. (2.83), that is, only the term proportional to $\dot{\mathbf{j}}^{(1)} \times \mathbf{B}^{(1)}$ has been considered for the numerical treatment. Furthermore, the relative SHG strength in these experiments has been closely related to the strength of the out-of-plane magnetic dipole moment of the studied SRRs.

In Refs. [17, 18], further experiments on arrays of resonant (centrosymmetric) bars and (non-centrosymmetric) “T”-structures have been carried out. The measured SHG from the magnetic resonance of the SRR arrays exceeds the SHG from all other resonant nanoparticles by at least a factor of 100. Furthermore, also the THG of these nanoparticle arrays has been measured in the same publication: the THG from the magnetic resonance exceeds the THG from all other resonances and nanoparticles.

The experimental setup used in both publications is similar to the one described in section 5.2. Thus, the exciting wavelength is $1.5 \mu\text{m}$. In order to investigate all resonances of the SRR mentioned above, so-called lithographical tuning has been performed. That is, the SRR design has to be adjusted such that the desired resonance is spectrally situated at $\lambda = 1.5 \mu\text{m}$.

In this chapter, we discuss SHG experiments similar to those in Refs. [16–18] on planar arrays of complementary SRRs (CSRR) [128], that is, the metal in the sample plane is replaced by air and *vice versa*. We compare the experimental results with microscopic numerical calculations based on the hydro-dynamic description of the optical properties of metals (see section 2.2.4 and Ref. [47]). The numerical calculations allow for determining the dominant second-order nonlinear source term [see Eq. (2.83)] by a switch-on switch-off analysis. Our collaborators Y. Zeng, W. Hoyer, and J. Liu in the groups of S. W. Koch and J. V. Moloney in Marburg and Tucson, respectively, have carried out the numerical calculations.

Additionally, we report on our THG experiments on the same structure providing very different results regarding the relative signal strengths.

6.1 Second-harmonic generation on complementary splitting resonators

Following the generalized version of Babinet’s principle [2, 129, 130] for an infinitesimally thin perfect conductor, the inverse planar structure shows the same linear optical spectra provided that reflectance is replaced by transmittance and *vice versa* and provided that the incident polarization is rotated by 90 degrees. At the same time, electric fields are replaced by magnetic fields and *vice versa*; precisely, the transformation $\mathbf{E} \rightarrow -c\mathbf{B}$ is carried out.

We point out that the symmetry of the SRRs and CSRRs is identical but the near fields change dramatically.

6.1.1 Experimental results

Our experimental results are illustrated in Figs. 6.1 and 6.2. The first rows in Fig. 6.1(a) and (b) show the scanning-electron micrographs of the investigated SRR- and CSRR-arrays.

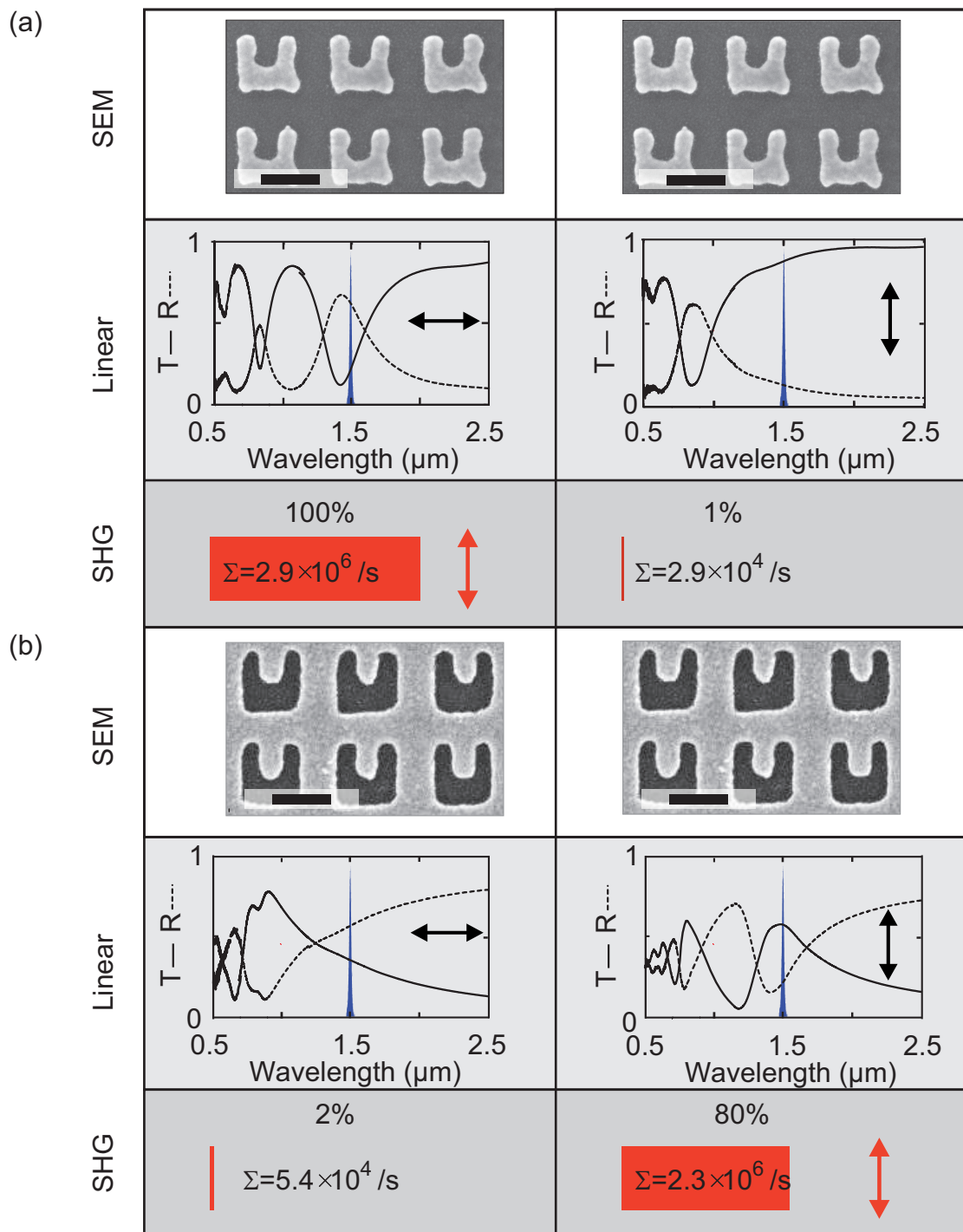


Figure 6.1: First rows: Scanning-electron micrographs of the investigated (a) SRRs and (b) CSRRs (scale bars correspond to 200 nm). Second rows: corresponding linear transmittance (solid line) and reflectance (dashed line) spectra. The respective polarization is indicated by the black arrows. Third rows: relative (with respect to SHG from SRRs for horizontal excitation) and absolute (in integral number of counts per second, Σ) SHG signals. The incident polarization is given by the black arrows from the second rows, the SHG polarization is given by the respective red arrows.

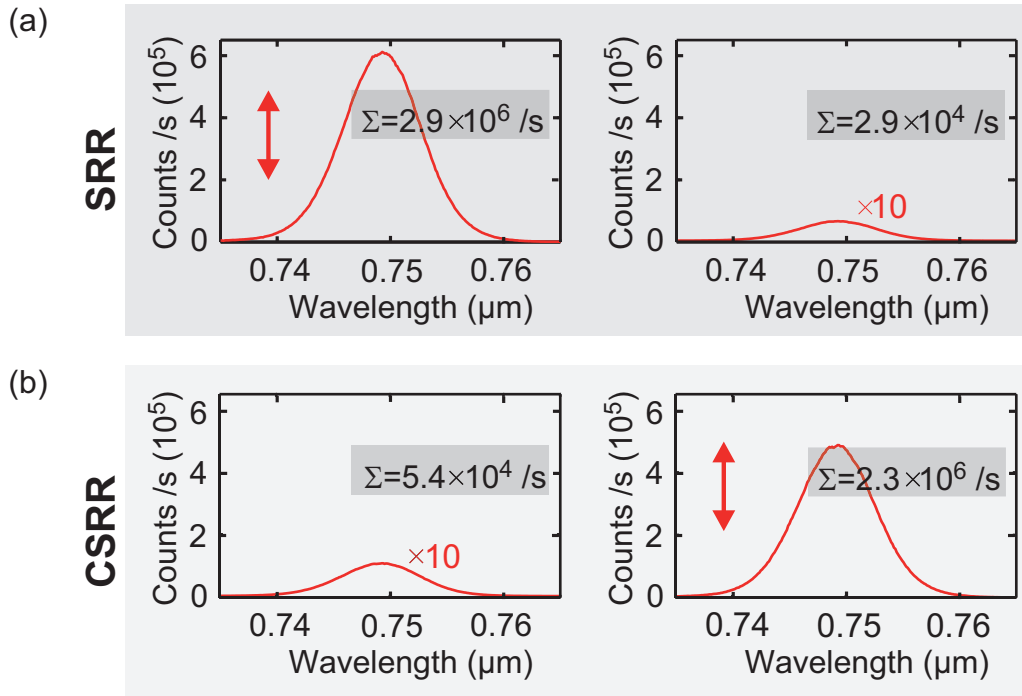


Figure 6.2: Measured SHG spectra of SRRs (a) and CSRRs (b) for horizontally polarized (left) and vertically polarized excitation (right). The measured SHG spectra nicely follow the Gaussian shape of the incident pulse centered around $\lambda = 0.75\mu\text{m}$.

The linear transmittance (solid curves) and reflectance (dashed curves) spectra shown in row two nicely demonstrate Babinet's principle, *i.e.*, transmittance and reflectance change roles when the polarization (indicated as black arrows) is rotated by 90 degrees and the structure is replaced by its complementary structure. The spectrum of the exciting pulse is depicted as blue-shaded area in each linear spectrum clarifying that the excitation is quasi-monochromatic. Finally, the relative (in percent) and absolute SHG signals (integral number of counts per second Σ , in the red bars) are given in the corresponding third rows. As expected, the SHG signal is maximal when the SRRs (CSRRs) are resonantly excited by horizontally (vertically) polarized light. The polarization of the SHG is depicted by red arrows (where the SHG intensity allows for polarization measurements). Since both SRRs and CSRRs have the same symmetry, the SHG polarization points into the same direction, although the exciting pulses are orthogonally polarized.

In Fig. 6.2, the measured SHG spectra are shown, revealing that the SHG spectra closely follow Gaussian shape of the exciting pulse. The area under these curves corresponds to the integral number of counts per second. From the bare substrate, we did not measure any SHG signal.

The number of counts per second can directly be related to the SHG power conversion efficiency (as stated in section 5.2, we estimate that the number of emitted SHG photons is roughly 3 times higher than the measured integral number of counts). For instance, $\Sigma = 2.9 \times 10^6 \text{ s}^{-1}$ corresponds to an absolute SHG power conversion efficiency of $\eta = 3 \times 10^{-11}$ (also consistent with Refs. [17, 18]). The SHG signal strength from the CSRR array is com-

parable to that of the SRR array. These results have been reproduced several times by interchanging the SRR and the CSRR samples back and forth and by repeating the experiment. Following Babinet's principle, the CSRRs exhibit no out-of-plane magnetic dipole moment under these conditions, yet, they lead to comparable SHG signals. This observation leads us to conclude that there is generally no correlation between SHG efficiency and the out-of-plane magnetic dipole moment. This correlation exists for all of the previous experiments presented in Refs. [16, 17], yet it is wrong in general.

6.1.2 Numerical results

To further clarify the nature of the SHG signal emerging from these metallic metamaterials, we compare the experiments with a recently developed microscopic theory [47]. Here, the nonlinear response is exclusively based on the metal classical electron gas as sketched in section 2.2.4. In short: the velocity of individual electrons is translated *via* a velocity field $\mathbf{v}(\mathbf{r}, t)$ into a current-density field $\mathbf{j}(\mathbf{r}, t)$ which is then put as source term into Maxwell's equations. In close analogy to hydro-dynamics, the total time derivative in Newton's second law leads to an additional convective contribution (we refer to section 2.2.4 and Ref. [46]). It has been found that this convective contribution dominates the SHG response of SRRs [47]. Here, we apply the same approach to CSRRs. Equation (2.82) is solved numerically together with Maxwell's equations by a finite-difference time-domain approach [131]. We use literature parameters for the gold plasma frequency ($\omega_{\text{pl}} = 2\pi \times 2.176 \times 10^{15} \text{ s}^{-1}$) and the collision frequency ($\gamma = 2\pi \times 1.031 \times 10^{13} \text{ s}^{-1}$) [71]. The lateral geometrical SRR and CSRR parameters are indicated as insets in Fig. 6.3, the gold thickness is 25 nm. The structures are located on a glass substrate ($\epsilon = 2.25$), coated with a 5-nm thin ITO layer ($\epsilon = 3.8$). We use a peak incident electric field of the 170-fs Gaussian pulses centered around 1.5 μm wavelength of $E_0 = 2 \times 10^7 \text{ V/m}$. These parameters allow for calculating not only the relative but also the absolute SHG power conversion efficiencies η without any adjustable parameters. Results are shown in Fig. 6.3, which can directly be compared with the experiment in Fig. 6.1. Obviously, the overall agreement with experiment is very good – especially if one considers the experimental uncertainties in determining E_0 (E_0 results from determining the focus diameter, the power at the sample, and the pulse duration).

By artificially switching on and off the different nonlinear source terms for SRRs (CSRRs), we find that the convective term accounts for about 68% (81%) of the SHG source current density $\mathbf{j}_{2\omega}^{(2)}$. The corresponding source term based on the magnetic part of the Lorentz force [16] shows a similar qualitative behavior but accounts for only about 2% (2%) of the SHG source current density.

6.2 Third-harmonic generation from complementary split-ring resonators

In analogy to our SHG experiments, we have performed THG experiments on SRR and CSRR arrays, too. Our results are depicted in Fig. 6.4. Again the magnetic resonance of the

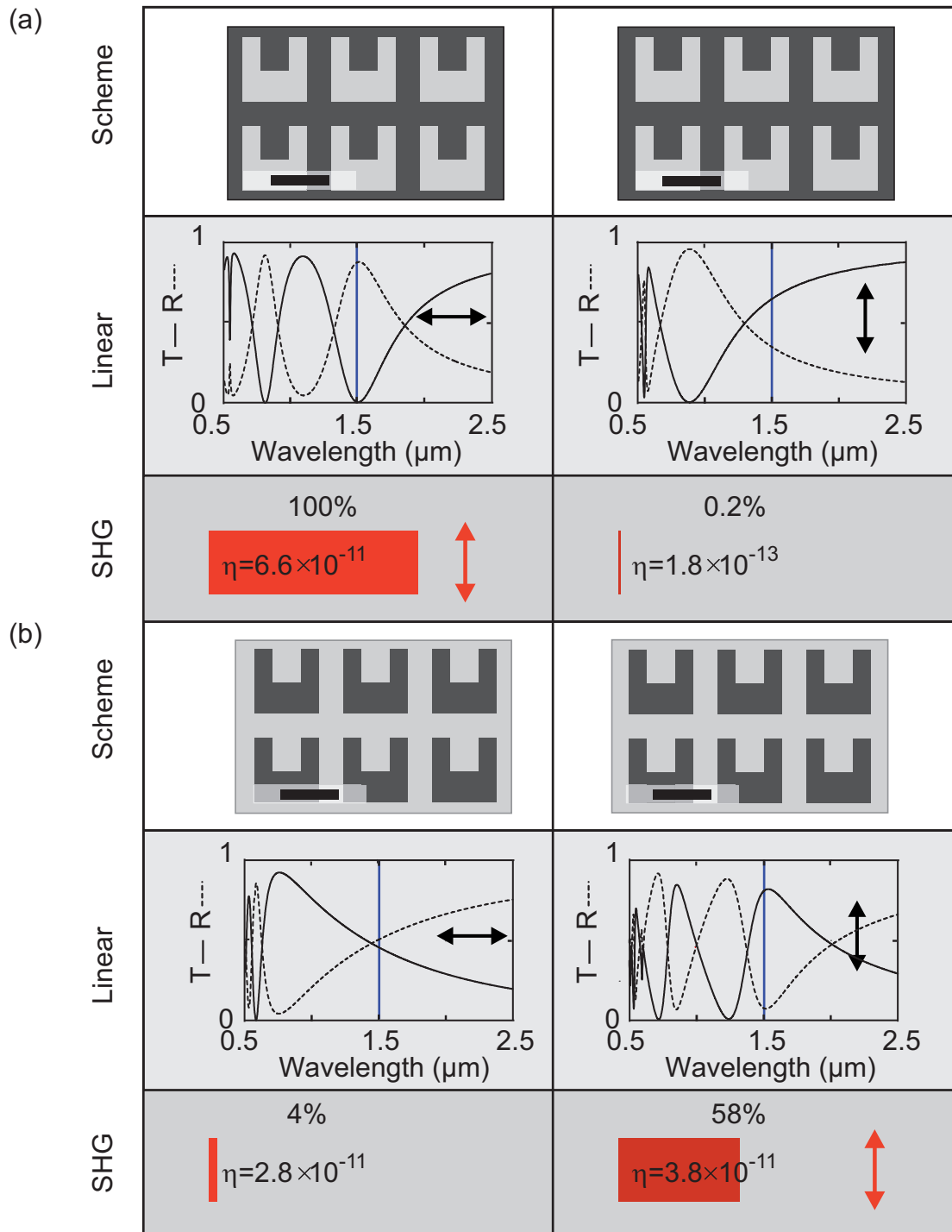


Figure 6.3: Theoretical results for (a) SRRs and (b) CSRRs that can directly be compared to the experimental results shown in Fig. 6.1. Instead of the integral number of counts per second, we quote the absolute power conversion efficiencies η . The scale bars in the schemes of the investigated structures correspond to 200 nm.

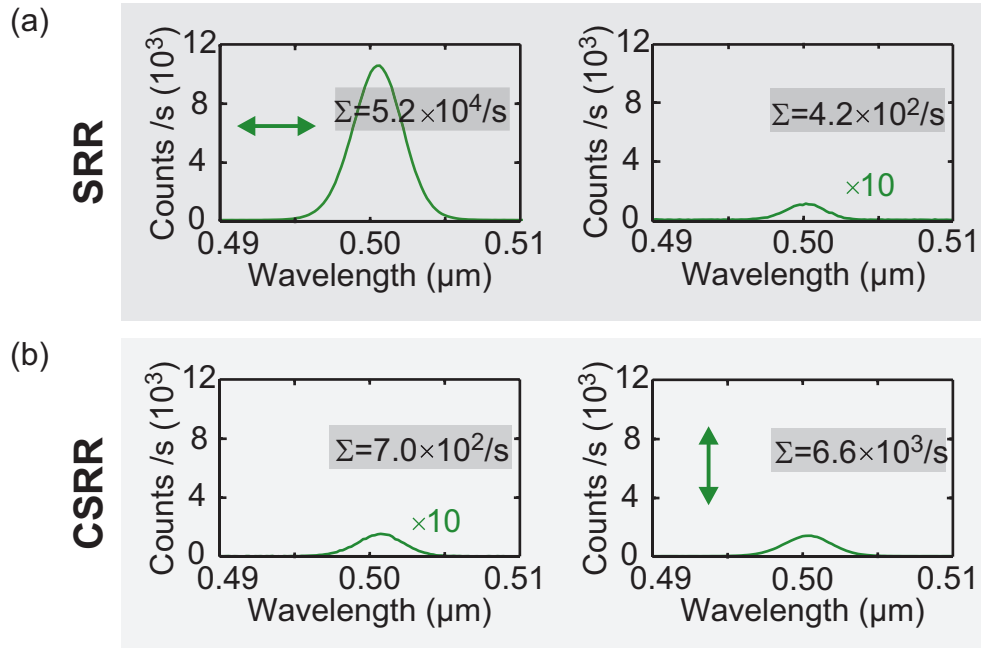


Figure 6.4: Measured THG spectra of SRRs (a) and CSRRs (b) for horizontally polarized (left) and vertically polarized incident light (right). The measured spectra nicely reveal the Gaussian shape centered around $\lambda = 0.5 \mu\text{m}$ of the incident pulse.

SRR array shows the largest THG signal. For both SRRs and CSRRs, the THG is polarized like the incident laser pulses. In contrast to the SHG signal (we have measured approximately the same SHG signal from SRRs and CSRRs), the THG signal from the SRRs' magnetic resonance is a factor of eight larger than the THG from CSRRs' corresponding resonance. In relative numbers: (i) SRRs: 100% (magnetic resonance) and (ii) CSRRs: 13% (fundamental resonance). The non-resonant excitations lead to 0.8% and 1.5% relative THG-signal for SRRs and CSRRs, respectively. For $\Sigma = 5.2 \times 10^4$ integral counts per second, we estimate $\eta = 1.8 \times 10^{-12}$ as THG power conversion efficiency.

Thus, the THG behavior is clearly distinct from the SHG behavior, likely due to different origins of the harmonics. Indeed, in previous work on other metamaterial structures [17, 18], SHG and THG have also behaved rather differently. Unfortunately, corresponding numerical calculations do not fit properly to the experimental results. This can have different reasons:

- The THG from the bare substrate (*i.e.*, ITO + Suprasil) is not negligible. We measured 340 integral counts per second (corresponding to about 0.4% of the THG signal from the SRRs). Thus, the THG might also be resonantly enhanced by the combination of SRRs/CSRRs and the substrate.
- The electronic polarization might not be the dominant THG source. Effects like saturated atomic absorption or even thermal effects might play an important role [44].

6.3 Conclusion

In conclusion, we have presented a comparative study of SHG from arrays of CSRRs and SRRs, both excited under normal incidence at their fundamental resonance. SRRs and CSRRs show comparable SHG, which is much larger than the SHG from any other structure that have been investigated so far in this context, meaning in Refs. [16, 17]. Our experimental results have been analyzed at the level of the hydro-dynamic theory of metals (see section 2.2.4) showing that the convective contribution dominates the second-order nonlinear response. Even the measured absolute SHG conversion efficiencies are in good agreement with the numerical calculations. Still, the exact microscopic mechanism is currently under controversial debate [47, 132, 133].

Our study on THG from SRRs and CSRRs together with the results from Refs. [17, 18] suggest that different mechanisms come into play than for SHG in metallic nanostructures.

Regarding possible applications, the CSRRs are advantageous in that they reveal a transmittance maximum at the fundamental resonance rather than a minimum for the SRRs. This larger transmittance potentially allows for stacking several layers along the propagation direction of light [134], thereby further enhancing the SHG conversion efficiency.

Chapter 7

Linear optical experiments on isolated photonic atoms

The optical properties of metamaterials are mainly determined by the properties of their individual building blocks. Still, interaction effects between these individual building blocks are known to play a crucial role [78, 135, 136]. Thus, with respect to studies on metamaterial arrays it is clearly favorable to investigate the individual optical properties of photonic atoms, when they are isolated from other photonic atoms. If, for instance, SRRs are arranged in a periodic fashion, effects like far-field and near-field coupling might alter their individual optical properties and even dominate the optical properties of the metamaterial [137–139]. In this chapter, we report on our experimental and theoretical work on isolated SRRs [140] and on the interaction effects in symmetric SRR dimers in different geometries and distances. We measure the absolute extinction-cross-section spectrum, which neither attenuated-total-internal-reflection spectroscopy [97] nor dark-field spectroscopy [98] are capable of.

7.1 Optical properties of isolated split-ring resonators

For measuring the optical properties of isolated SRRs, we make use of the spatial modulation technique we have presented in detail in section 5.3. Here, the modulation is realized by a one-dimensional piezoelectric transducer that periodically moves the entire sample. The modulation amplitude is set to $a_0 = 3\ \mu\text{m}$ and the modulation frequency is set to 120 Hz. The 2D scans ($6\ \mu\text{m} \times 12\ \mu\text{m}$) are performed by means of a three-dimensional piezoelectric transducer stage; the lateral step size is set to 330 nm. The SRRs on the substrate have at least $25\ \mu\text{m}$ distance to the next object, be it the “neighboring” SRR or a knife-edge for finding and characterizing the Gaussian focus. Thus, we do not expect any influence of the environment on the investigated SRR. Here, the dimensions of the SRR are [as defined in Fig. 3.3(b)]: $l_x = 213\ \text{nm}$, $l_y = 210\ \text{nm}$, $w = 73\ \text{nm}$, $h = 118\ \text{nm}$, and $t = 25\ \text{nm}$. These dimensions have been used for the numerical calculations that are based on an in-house finite-difference time-domain (FDTD) code employing a total-field scattered-field approach and perfectly matched layers [131]. The code has been developed and the calculations are carried out by our collaborators M. König and J. Niegemann in the group of K. Busch.

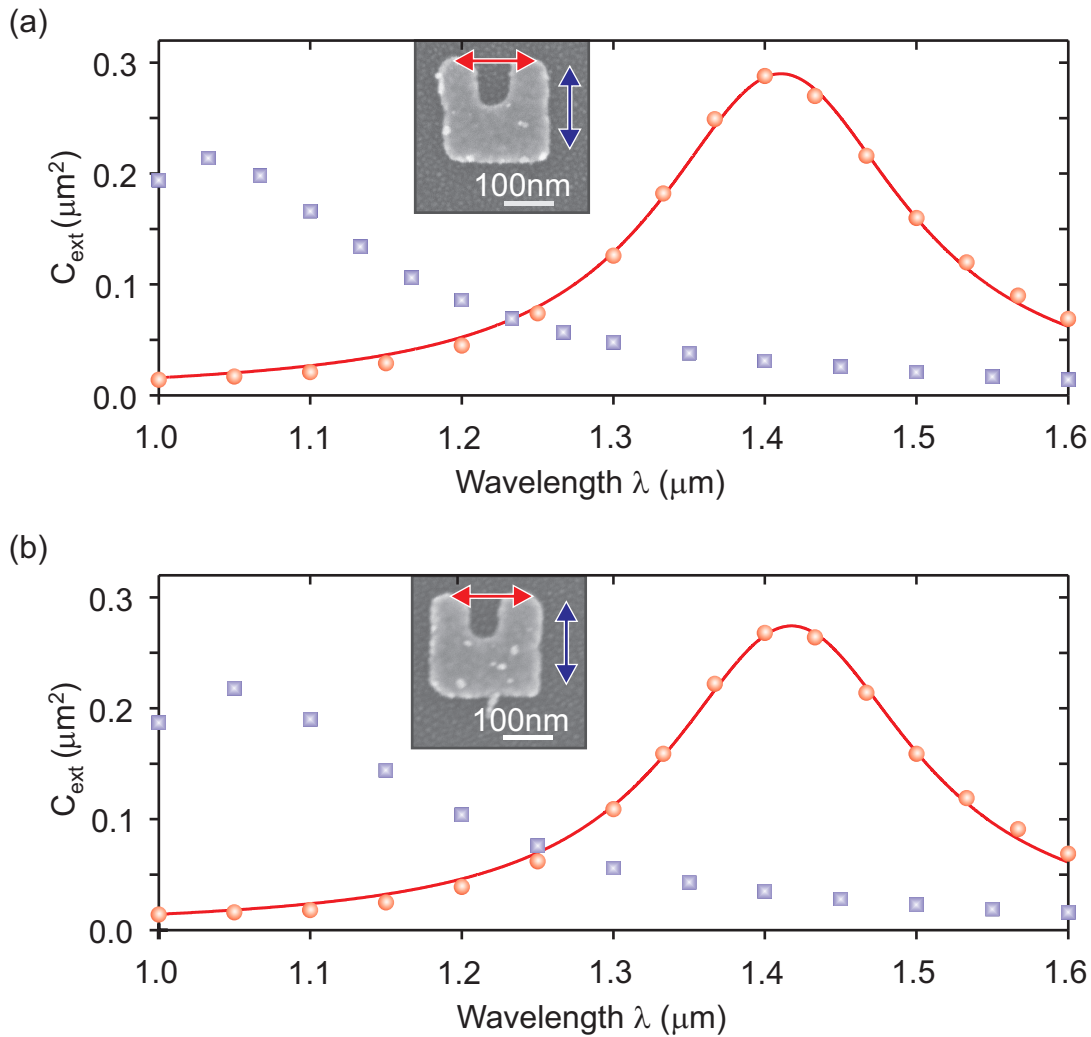


Figure 7.1: (a) Measured absolute extinction-cross-section spectrum $C_{\text{ext}}(\lambda)$ of an individual SRR. The two different polarization configurations are illustrated by the insets. (b) As (a) for a different but similar SRR. The red solid curves are fits using an intuitive RLC circuit model.

For horizontally incident linear polarization in Fig. 7.1(a), the measured extinction cross-section of this individual SRR [the SEM image is shown as inset in Fig. 7.1(a)] reveals a pronounced spectral maximum at around 1.4 μm -wavelength. Arrays of closely similar SRRs have previously been investigated and this resonance has been attributed to the magnetic-dipole mode (see also section 3.3). The spectral position is also in good agreement with complete numerical solutions of the vector Maxwell equations (see below). To further support this interpretation, we also depict in Fig. 7.1(a) the extinction-cross-section spectrum for the orthogonally incident linear polarization of light. The resonance around 1.4 μm disappears as expected from the results on arrays. In essence, the incident electric field can no longer couple to the capacitor formed by the two vertical arms of the SRR. Together with the inductor given by the incomplete single winding of a coil, this capacitor forms a resonant LC -circuit – a tiny electromagnet with a magnetic-dipole moment perpendicular to its plane. As stated earlier, this resonance is the fundamental plasmonic mode of the SRR.

Figure 7.1(b) summarizes results for a sample different from but closely similar to that in Fig. 7.1(a). The cross-section spectra in (a) and (b) agree regarding their shape as well as regarding their peak value.

The maximum value of $C_{\text{ext}} = 0.29 \mu\text{m}^2$ can be translated into $0.15 \times \lambda^2$ at the resonance wavelength $\lambda_0 = 1.4 \mu\text{m}$. Alternatively, this result can be expressed as $C_{\text{ext}} = 8 \times A_{\text{SRR}}$ with the geometric area of the SRR $A_{\text{SRR}} = 0.038 \mu\text{m}^2$ that we have directly deduced from the electron micrograph [see insets of Fig. 7.1(a)].

As usual, the extinction cross-section is the sum of the absorption cross-section and the scattering cross-section, that is, $C_{\text{ext}} = C_{\text{abs}} + C_{\text{scatt}}$. To theoretically analyze the relative strengths for our conditions, we have performed numerical calculations using the SRR geometrical parameters from the experiment [the exact geometry is shown in the inset of Fig. 7.2(a)] and literature free-electron Drude-model parameters for the gold [27]. We include the glass substrate as a dielectric half space with refractive index $n = 1.5$. The curves in Fig. 7.2(a) show corresponding results. The calculated absolute extinction cross-section (solid curve) nicely agrees with the measured one (symbols). About one third of the peak extinction cross-section is due to absorption (dashed curve), two thirds are due to scattering (dotted curve).

It is interesting to ask whether the extinction cross-section is a property of the SRR alone or whether it is influenced by its dielectric surrounding. Figure 7.2(b) shows the extinction cross-section for SRRs identical to the half-space geometry in Fig. 7.2(a), but embedded in different homogeneous dielectric environments. It becomes obvious that all curves in (b) are different from C_{ext} in (a), which means that the actual electromagnetic density of states of the half-space geometry significantly influences the coupling of the SRR to the light field. Resulting effects are as large as 30 % in the peak extinction cross-section. In general, this result implies that comparing measured cross-sections of metallic nanoparticles on glass substrates (a very common geometry in experiments) with calculations of such particles in a fictitious effective homogeneous medium is somewhat questionable.

While these microscopic calculations nicely agree with the experiments and have also given important additional insights, they do not really provide us with an intuitive understanding. Hence, we would like to connect the extinction cross-section of an individual SRR to the frequently used electric-circuit model (compare section 3.3). We shortly recall: in addition to the already mentioned capacitance C and inductance L of the SRR, an effective serial resistance R should be considered. This resistance comprises an Ohmic contribution due to loss in the metal, R_{Ohm} , as well as a contribution due to electromagnetic radiation, the radiation resistance R_{rad} . Kirchhoff's voltage law immediately allows to compute the current I induced by the voltage drop Ed via the horizontally polarized incident electric field E in the capacitor gap with width d . For the resonance wavelength λ_0 and in the limit for which the extinction cross-section is much smaller than the Gaussian focus area, we can use Eq. (3.17): $C_{\text{ext}} = \frac{Z_0}{R_{\text{rad}} + R_{\text{Ohm}}} d^2$. d^2 is about one ninth of the geometric area of our SRRs. Hence, effective resistances R much smaller than the vacuum impedance of $Z_0 = 376.7 \Omega$ lead to cross-sections that exceed the geometrical area. From a fit to the experimental data shown in Fig. 7.1(a) and with $d = 65 \text{ nm}$ from the electron micrograph shown in the inset of Fig. 7.1(a), we obtain an effective SRR resistance of $R = 5.5 \Omega$. This value is reason-

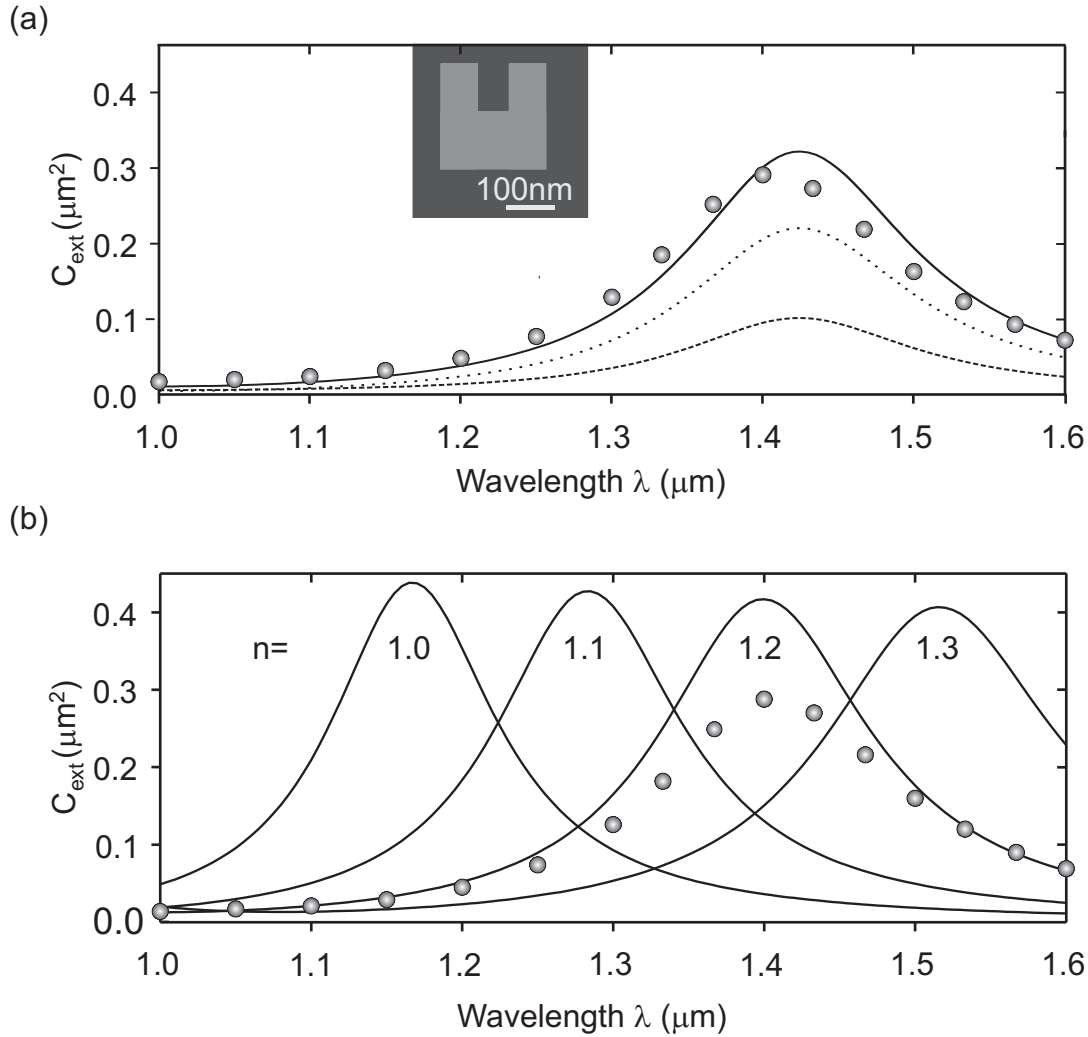


Figure 7.2: (a) The SRR is located on a glass substrate, the incident linear polarization is horizontal. Shown are the extinction cross-section C_{ext} (solid), the absorption cross-section (dashed), and the scattering cross-section (dotted) spectra. (b) C_{ext} for the identical SRR, but embedded in a (fictitious) homogeneous medium with refractive index n as indicated. The symbols in (a) and (b) are the experimental data from Fig. 7.1(a), which are reproduced here for comparison.

ably close to recent theoretical estimates of the SRR radiation resistance in a homogeneous dielectric environment [70]. From this formula [see Eq. (3.16)], we estimate for our parameters a radiation resistance $R_{\text{rad}} = 10 \Omega$. We further estimate $R_{\text{Ohm}} = 4 \Omega$. The relative magnitude of these values is qualitatively consistent with our above microscopic discussion on absorption and scattering. The dependence of C_{ext} versus frequency clearly resembles a Lorentzian line shape. Fitting this Lorentzian to the experimental data [see red solid curve in Fig. 7.1(a)] provides us with the effective SRR capacitance $C = 19 \text{ aF}$ and the effective SRR inductance $L = 30 \text{ fH}$.

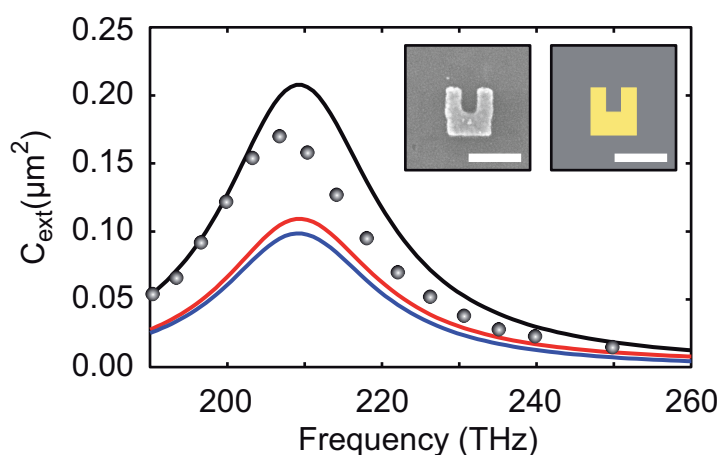


Figure 7.3: Measured (dots) and calculated (black curve) extinction cross-section of a single SRR for normal incidence and horizontal polarization. The corresponding calculated absorption-cross-section and scattering-cross-section spectra are represented by the red and blue curve, respectively. The insets show a scanning electron micrograph of the single SRR and the geometry assumed in our calculations, respectively. The scale bars are 200 nm.

7.2 Interaction effects in split-ring-resonator dimers

In arrays of photonic atoms, the total electromagnetic field acting on each photonic atom is the superposition of the incident light field and the scattered fields of all other photonic atoms. Thus, the optical properties of photonic metamaterials are governed by the interplay of two contributions: (i) the optical response of the individual photonic atoms resulting from the direct excitation with the incident light field and (ii) the mutual electromagnetic couplings of the photonic atoms mediated by the scattered fields. The latter can be decomposed into the elementary, that is, pair-wise, interactions of the photonic atoms, which depend on the relative separation and relative orientation of the two corresponding photonic atoms. In this section, we report on our work on the interaction between such pairs of SRRs – in analogy to pairs of atoms, we call them SRR dimers.

The importance of coupling effects in photonic metamaterials has been demonstrated in several experiments. For example, coupling between stacked layers of SRRs results in spectral splitting of the fundamental magnetic mode [134, 141] and lateral coupling in low-symmetry 2D SRR arrays leads to a modification of the polarization eigenstates [139]. Another manifestation of interaction effects in metamaterials is the formation of magneto-inductive waves observed at microwave [135, 142] and near-infrared frequencies [78]. Near-field and far-field coupling effects have also been predicted theoretically and observed experimentally in the context of plasmonic particles [137, 138, 143–145].

In this section, we report on our experimental and theoretical studies on the lateral electromagnetic coupling of SRRs. For this purpose, two SRRs forming a dimer can be considered as a model system which can be utilized for systematic studies of the elementary coupling effects in 2D magnetic metamaterials. The uncoupled system corresponds to two infinitely separated SRRs. Thus, the spectrum of a single SRR multiplied by a factor of two can serve as a reference. By comparing the extinction-cross-section spectrum of the SRR dimer with

this reference, we can directly infer the influence of the mutual electromagnetic interaction on the spectral position of the resonance as well as the corresponding quality factor and the peak value of the extinction cross-section. Investigations of the coupling mechanism of two SRRs for a different excitation geometry and for microwave frequencies have been reported in Ref. [136].

Figure 7.3 shows the measured and numerically calculated extinction-cross-section spectrum of an isolated SRR that has the same design as the SRRs of the investigated dimers. Our numerical calculations reveal that for this SRR-design, the absorption and scattering cross-sections contribute to about equal parts to the extinction cross-section. The doubled extinction-cross-section spectrum serves as reference.

As experimental setup, we use the spatial modulation setup discussed in section 5.3. A piezoelectric tilt mirror mounted in front of the first microscope objective lens is utilized to periodically modulate the lateral position of the Gaussian beam in the sample plane in one direction with an amplitude of about $a_0 = 1.5 \mu\text{m}$ at a frequency of 4000 Hz. Additionally, we perform a 2D lateral scan ($7 \mu\text{m} \times 5 \mu\text{m}$) of the sample by means of a three-dimensional piezoelectric transducer stage; the lateral step size is set to 200 nm.

The microscopic numerical calculations are based on an in-house discontinuous-Galerkin time-domain (DGTD) code employing a total-field scattered-field approach and perfectly matched layers [146–148]. The code has been developed and the calculations have been carried out by our collaborators M. König, J. Stannigel, and J. Niegemann in the group of K. Busch.

7.2.1 The dipole-dipole interaction model

Before we address the experimental results for SRR dimers, we discuss the anticipated coupling effects in terms of an intuitive dipole-dipole interaction model. In analogy to electric dipole-dipole coupling in plasmonic dimers [137, 138, 143–145], we substitute each SRR by *two* dipoles as sketched in Fig. 7.4(a): (i) an electric dipole oriented parallel to the incident light polarization and (ii) a magnetic dipole oriented perpendicular to the SRR. To account for the actual electric and magnetic near-field distribution [see Figs. 7.4(b) and (c)], we position the magnetic dipole in the center of the SRR while the electric dipole is located between the two ends of the SRR. For small separations, that is, $d \ll \lambda/4$, retardation effects can be neglected. In this case, the interaction between equally oriented dipoles (meaning the dipoles oscillate in phase) – be it electric or magnetic – yields an increase (decrease) of the resonance frequency for a transverse (longitudinal) arrangement as illustrated in Fig 7.5. Clearly, for opposing orientation of the dipoles (that is, the dipoles oscillate with a π -phase shift) results in a decrease (increase) of the resonance frequency for a transverse (longitudinal) arrangement.

Due to the symmetry of the investigated system, consisting of the SRR dimer *and* the incident plane wave, the electric dipoles always oscillate in phase. In contrast, the magnetic dipoles either oscillate in phase or with a π -phase shift. These modes are the radiating modes, that is, they possess an electric dipole moment that radiates into the far field. The other mode for which the two electric dipoles oscillate with a π -phase shift, does not possess an elec-

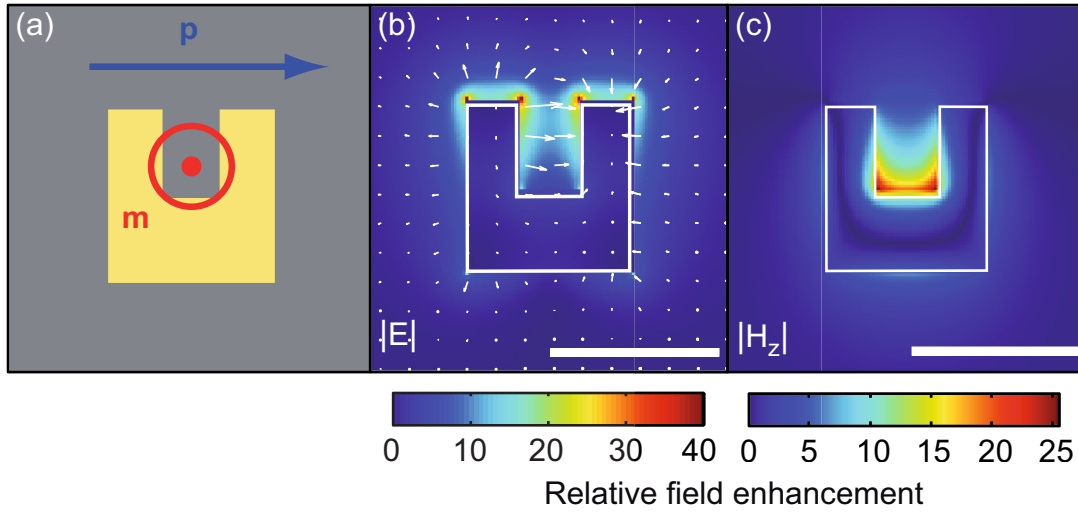


Figure 7.4: (a) Equivalent dipole model for an SRR. The blue (red) arrow corresponds to the electric (magnetic) dipole moment. (b) Calculated absolute value of the electric near field for the plane intersecting the middle of the SRR at the resonance frequency ($f_{\text{res}} = 210$ THz). The white arrows depict the direction of the electric near field. (c) Calculated absolute value of the z-component of the magnetic near field at the resonance frequency ($f_{\text{res}} = 210$ THz). The scale bars in (b) and (c) are 200 nm.

tric dipole moment and does not radiate into the far field – this mode is called dark mode. Exciting this mode requires breaking the symmetry either by altering one of the SRRs or by oblique incidence of the plane wave.

Additionally, the coupling of each SRR to the radiation field will be altered by the presence of the second SRR. It acts as an antenna, which transfers some of the SRR's electromagnetic near field to the far field. This results in an increase of the line width and a related decrease of the peak value of C_{ext} . In other words, we expect that the extinction cross-section of the SRR dimer is smaller than the combined extinction cross-section of two uncoupled SRRs. Due to the antenna effect, we also anticipate that the scattering cross-section becomes more important at the expense of the absorption cross-section for decreasing separation of the two SRRs.

The relative strength of the electric dipole-dipole interaction and magnetic dipole-dipole interaction obviously depends on the exact electromagnetic near-field distribution. Thus, our dipole-dipole model can not make corresponding *a priori* predictions. However, it allows for intuitive *a posteriori* interpretations of the resulting spectral shifts. For quantitative results, we have to refer to our rigorous numerical calculations (see below). Finally, we want to emphasize that the dipole-dipole interaction model has to be considered as a first approximation since several aspects of the SRR-SRR interaction can not be covered within its framework, for example, the finite extent of the SRRs or coupling of higher order multipoles. Again, these aspects are taken fully into account in our rigorous numerical calculations (see below). For larger separations ($d \gtrsim \lambda/4$), retardation effects become important resulting in periodic modulations of the resonance frequency and the quality factor, respectively, of the dimer's

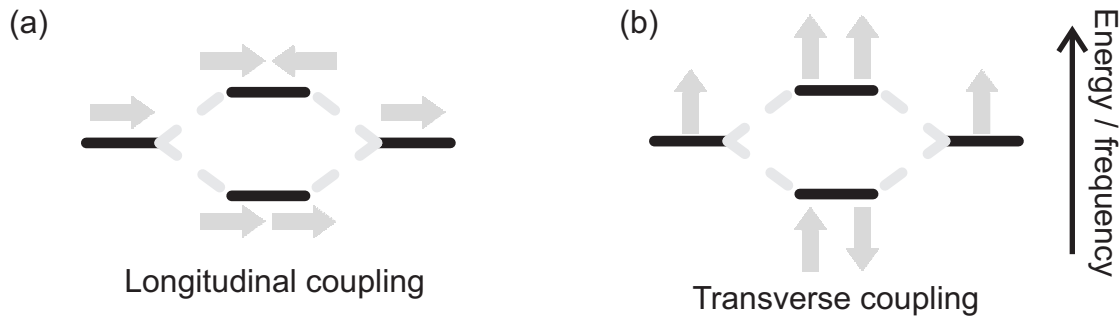


Figure 7.5: (a) [(b)] Illustration of the expected qualitative energy shifts that correspond to shifts of the resonance frequency due to longitudinal (transverse) near-field dipole-dipole coupling. The dipole orientations are indicated as gray arrows.

coupled mode [137, 138]. This behavior can be qualitatively explained by a model system consisting of two electric dipoles with distance d in analogy to the discrete-dipole approximation [149]. Consequently, the electric field at the position of one of the two dipoles is the superposition of the incident plane wave and the field scattered by the other dipole. In this analytical model, one finds that the radiated power is an oscillating function of the distance of the two dipoles.

7.2.2 Investigated SRR dimer configurations

The four different SRR dimer configurations investigated here are shown in Fig. 7.6(a). In the side-by-side configuration and the on-top configuration, the two SRRs have the same orientation and the vertical wires and the bottom wires, respectively, are aligned flush. These two configurations are directly related to a usual 2D SRR array and probe the coupling along the two primitive lattice vectors of the array [see red and blue boxes in Fig. 7.6(a) and (b), respectively]. In the gap-to-gap configuration and the back-to-back configuration, the vertical wires are aligned flush and the two gaps and the two bottom wires, respectively, face each other. These configurations have been chosen because we find particularly strong (weak) SRR-SRR coupling for the gap-to-gap (back-to-back) configuration. We vary the separation of the two SRRs between ~ 30 nm and ~ 230 nm. These separations are comparable to those of nearest neighbors in typical 2D SRR arrays. SRR dimers with larger separations have not been fabricated since our measurement technique requires that the total extent of the dimer is small compared to the wavelength of the incident light.

The intended studies require the fabrication of high quality samples in which the shape and size of the SRRs in the different dimers is kept constant. Thus, we have taken great care during the lithography process to adjust the dose for each SRR dimer to guarantee minimal geometric deviations. This is demonstrated in Fig. 7.7, which depicts scanning-electron micrographs of all investigated SRR dimers for separations ranging from 225 nm to 30 nm. Here, it becomes obvious that the dimensions of all investigated SRRs are closely similar. In our optical experiments, we found a small difference between single SRRs fabricated as shown in the electron micrograph of Fig. 7.3 and single SRRs fabricated up-side-down: the

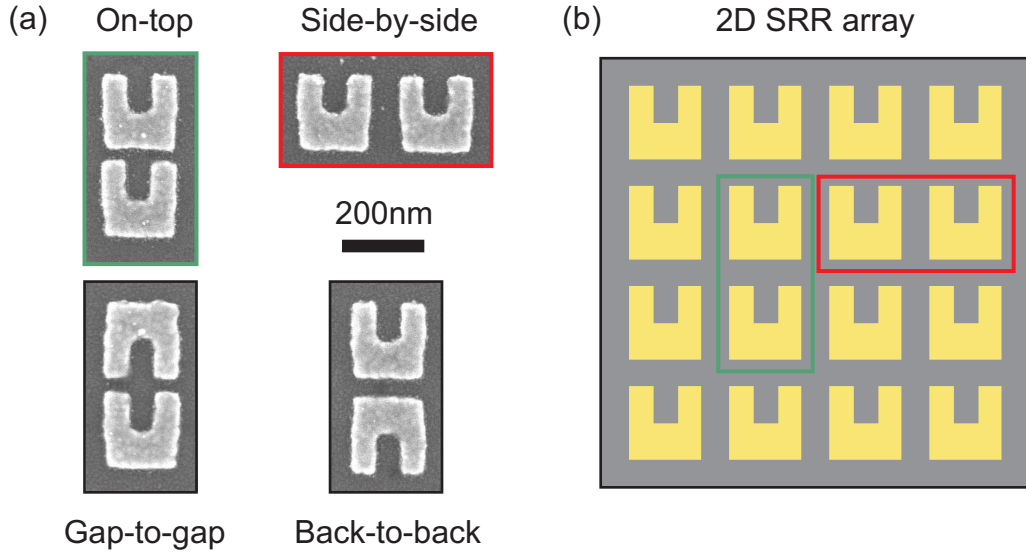


Figure 7.6: (a) The different SRR configurations under investigation. (b) The on-top and the side-by-side configurations are directly related to the nearest-neighbor arrangement in SRR arrays as indicated by the colors.

difference in the peak value of the extinction-cross-section spectrum is $0.005 \mu\text{m}^2$ and the difference in the spectral position of the peak is 5 THz.

7.2.3 Experimental and numerical results

The measured extinction cross-sections for the four dimer configurations are presented in Fig. 7.8(a)-(d) as circles. In addition to the spectra of the dimers, we have depicted in each case the spectrum of the same single SRR multiplied by a factor of two as a reference. The solid curves are Lorentzian fits to the experimental data. From these fits, we derive the resonance frequency f_{res} , the peak value of the extinction-cross-section spectrum C_{ext} , and the quality factor Q defined as $Q = f_{\text{res}}/\Delta f_{\text{res}}$, where Δf_{res} is the full width at half maximum of the resonance peak.

Side-by-side configuration In Fig. 7.8(a), the measured extinction-cross-section spectra for the side-by-side configuration are depicted for separations ranging from $d = 50 \text{ nm}$ to $d = 225 \text{ nm}$. For decreasing separation, the resonance frequency of the dimer's coupled mode gradually shifts to lower frequencies and the corresponding quality factor degrades. Furthermore, we find that the reference's peak value of C_{ext} exceeds that of all dimers in this configuration. For the smallest separation ($d = 50 \text{ nm}$), the frequency shift is about 6% of f_{res} of the reference. The quality factor decreases from $Q = 8.7$ (reference) to $Q = 5.5$ ($d = 50 \text{ nm}$) and the peak value of C_{ext} decreases from $C_{\text{ext}} = 0.34 \mu\text{m}^2$ (reference) to $C_{\text{ext}} = 0.3 \mu\text{m}^2$ ($d = 50 \text{ nm}$). The red shift of the resonance for the side-by-side configuration can be understood in terms of the dipole-dipole interaction model. For symmetry reasons, the incident light field can only excite a symmetric mode of the dimer in which the two electric dipoles and the two magnetic dipoles are oscillating in phase. The electric dipoles are

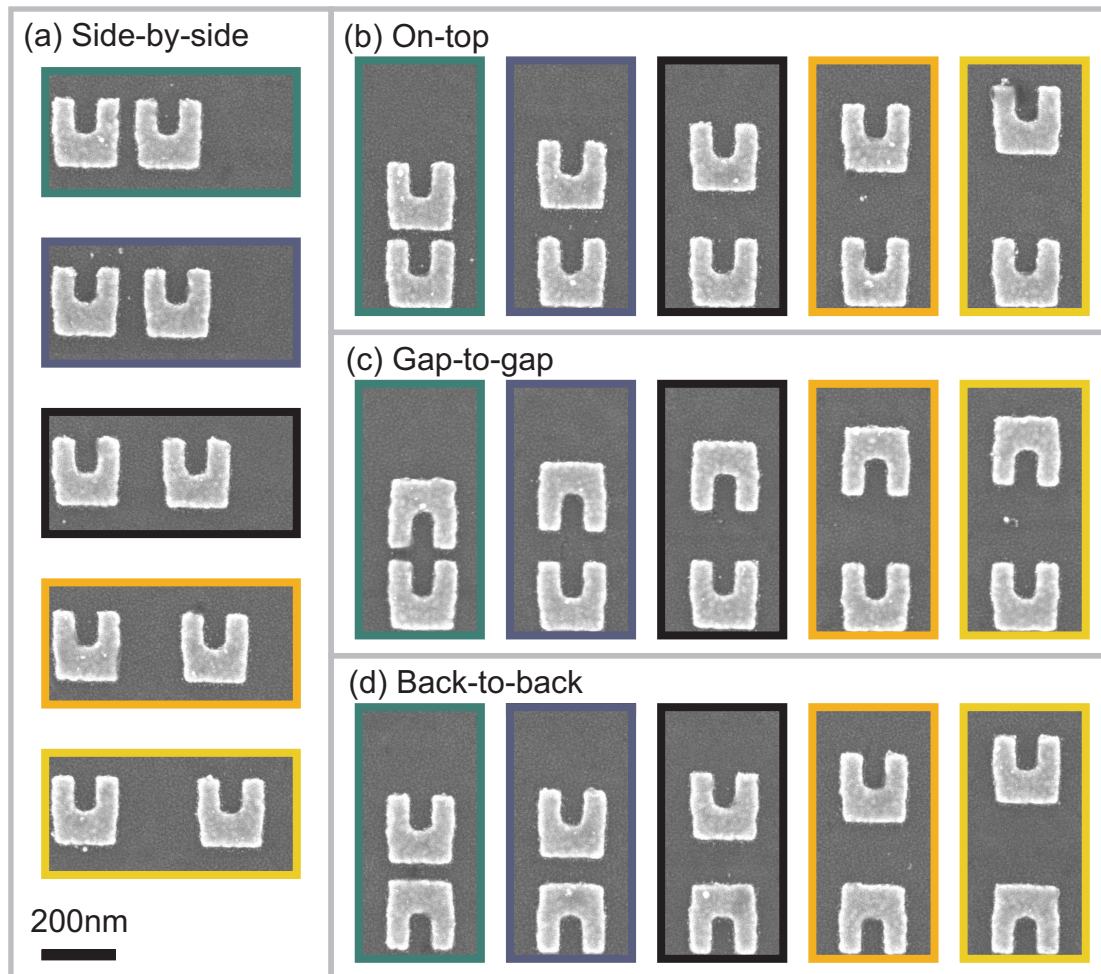


Figure 7.7: Scanning-electron micrographs of all studied SRR dimers. The colors of the boundaries of the electron micrographs correspond to the internal dimer distances, which are given explicitly in Figs. 7.8 and 7.9 with the same color code. All micrographs are displayed with the same magnification.

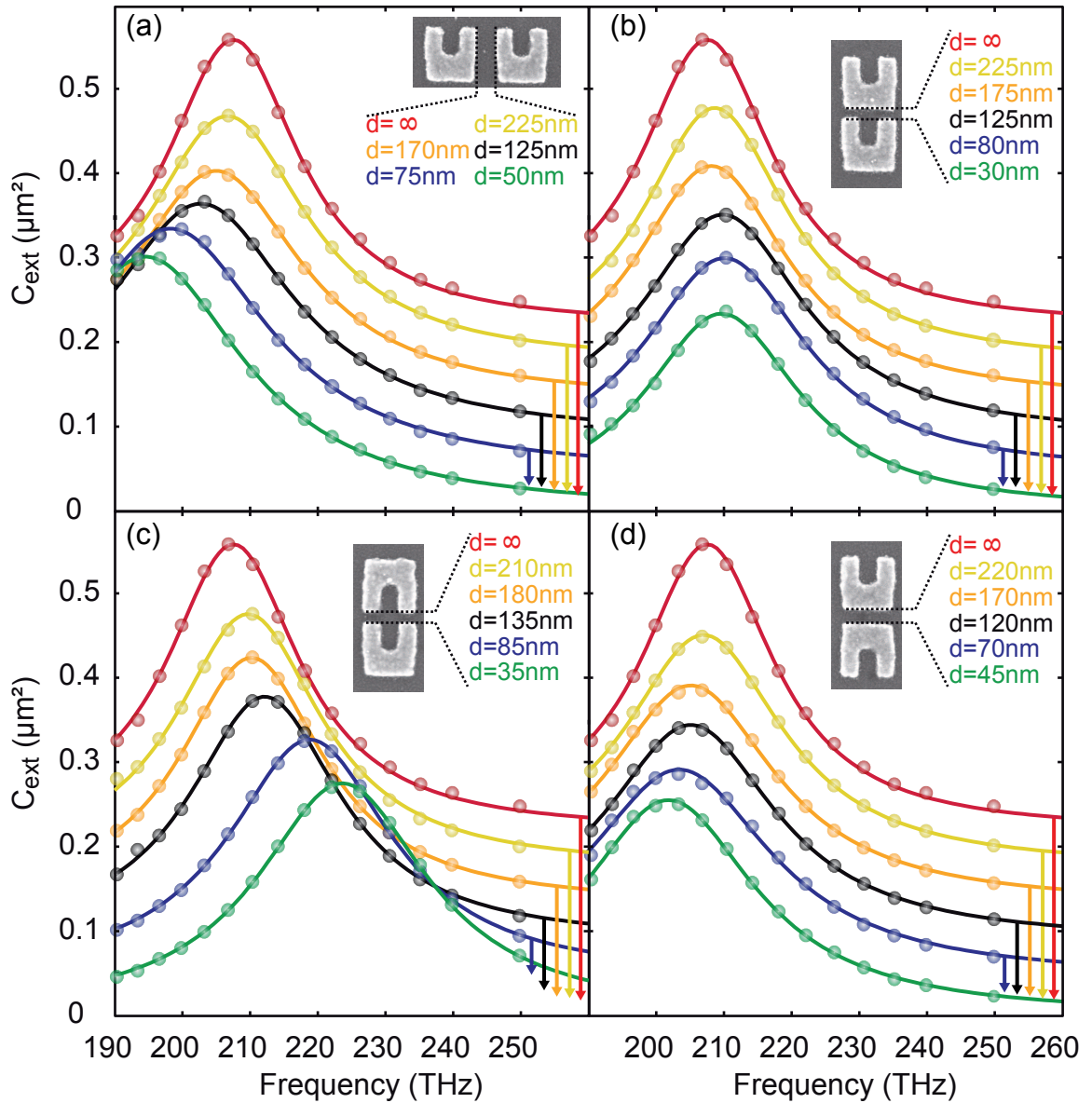


Figure 7.8: Measured extinction-cross-section spectra of four different sets of SRR dimers for different separations. The symbols correspond to the experimental data. The solid curves are Lorentzian fits to the experimental data. The different curves in each set are vertically displaced for clarity (see arrows). (a) Side-by-side configuration, (b) on-top configuration, (c) gap-to-gap configuration, and (d) back-to-back configuration.

oriented parallel to the axis of the SRR dimer resulting in longitudinal electric dipole-dipole coupling. In contrast, the magnetic dipoles are oriented perpendicular to the SRR dimer axis, meaning, the magnetic dipoles are coupled transversely. The longitudinal electric dipole-dipole interaction tends to decrease the resonance frequency while the transverse magnetic dipole-dipole interaction has the opposite effect. Thus, the red shift of the resonance suggests that the interaction between the two SRRs is dominated by electric dipole-dipole coupling in case of the side-by-side configuration. The decrease of the quality factor and the peak value of the extinction cross-section is also consistent with the reasoning given above.

On-top configuration Next, we address the experiments for the on-top configuration. The corresponding measured extinction-cross-section spectra for separations ranging from $d = 30$ nm to $d = 225$ nm are depicted in Fig. 7.8(b). Here, the resonance frequency slightly increases with decreasing separation. The observed spectral shift is comparable to the limits set by the variation of f_{res} due to fabrication tolerances. This small shift is also consistent with the corresponding numerical calculations [see Fig. 7.9(b)]. Additionally, we find a significant reduction of the quality factor and the peak value of the extinction cross-section, respectively. For the smallest separation ($d = 30$ nm), the quality factor is $Q = 7.4$ and the peak value of the extinction cross-section is $C_{\text{ext}} = 0.23 \mu\text{m}^2$. In terms of the dipole-dipole interaction model, one expects a blue shift of the dimers' coupled mode for the on-top configuration since both the electric and the magnetic dipoles are coupled transversely. The weakness of this effect can be traced back to the induction of a mirror electric dipole in the bottom wire of the top SRR by the electric dipole of the bottom SRR. This induced electric dipole counteracts the electric dipole in the top SRR excited by the incident plane wave. For small separations, the magnitude of the spectral shift of the dimer's resonance frequency with respect to the reference is a measure for the coupling strength of the two SRRs. A comparison of the results for the side-by-side configuration and the on-top configuration suggests that the nearest neighbor interaction of equally oriented SRRs in dense square arrays is dominated by the side-by-side configuration rather than by the on-top configuration. This interpretation is further supported by our numerical calculations [see Figs. 7.9(a) and (b)].

Gap-to-gap configuration The measured extinction-cross-section spectra for the gap-to-gap configuration are shown in Fig. 7.8(c). Here, the reduction of the separation between the two SRRs leads to a strong increase of the resonance frequency. At the same time, we observe a continuous reduction of Q and C_{ext} . For the smallest separation ($d = 35$ nm), the shift of the resonance frequency of the dimer's coupled mode is 8% of f_{res} of the reference. The corresponding quality factor is $Q = 7.3$ and the corresponding peak value of the extinction cross-section is $C_{\text{ext}} = 0.27 \mu\text{m}^2$. In the gap-to-gap configuration, the two SRRs are rotated against each other by 180° with respect to the interface normal. Again, the incident light field can only couple to a symmetric mode of the dimer. Thus, the two electric dipoles are excited in phase but the two magnetic dipoles are oscillating with a phase shift of π in the gap-to-gap configuration. For transverse dipole-dipole coupling, the interaction of the parallel oriented electric dipoles increases the resonance frequency while the interaction of

the anti-parallel oriented magnetic dipoles tends to counteract this effect. Again, we find that the interaction between the two SRRs is dominated by electric dipole-dipole coupling.

Back-to-back configuration Finally, we address the experiments for the back-to-back configuration [see Fig. 7.8(d)]. For this configuration, the reduction of the separation between the two SRRs leads to a slight decrease of the resonance frequency which is comparable to the corresponding spectral shift in the numerical calculations [see Fig. 7.9(d)]. At the same time, we observe a continuous reduction of Q and C_{ext} . For the smallest separation ($d = 45$ nm), the quality factor is $Q = 6.5$ and the peak value of the extinction cross-section is $C_{\text{ext}} = 0.25 \mu\text{m}^2$. Like in the previous case, all dipoles are transversely coupled with the two electric dipoles excited in phase and the two magnetic dipoles oscillating with a π -phase shift. However, in our model, the electric dipoles are further separated in the back-to-back configuration than in the gap-to-gap configuration for the same value of d . In contrast, the separation of the magnetic dipoles does not change. Hence, we expect that the relative importance of the electric dipole-dipole interaction becomes weaker. The slight red shift of the resonance even indicates that for the back-to-back configuration the magnetic dipole-dipole coupling is more efficient than the electric dipole-dipole coupling.

Numerical results To support our interpretations, we have performed rigorous numerical calculations based on an in-house DGTD code. The electric permittivity of gold is described with the free-electron Drude model with plasma frequency $\omega_{\text{pl}} = 2\pi \times 2.193 \times 10^{15} \text{ s}^{-1}$ and collision frequency $\gamma = 2\pi \times 2.224 \times 10^{13} \text{ s}^{-1}$. In all our calculations, the SRRs are characterized by the same set of geometrical parameters which has been derived from a scanning-electron micrograph of a single SRR (see insets in Fig. 7.3).

The calculated extinction-cross-section spectra of the four configurations are depicted in Fig. 7.9. Here, the separation matches the corresponding experiment (see Fig. 7.8) in each case. The numerical calculations qualitatively and almost quantitatively reproduce all trends observed in the corresponding experiments (compare Fig. 7.8 and Fig. 7.9). Additionally, we have calculated extinction-cross-section spectra for separations exceeding the experimental range. For separations comparable to or larger than the resonance wavelength, C_{ext} and Q exhibit an oscillatory behavior. Analogous effects have been observed for plasmonic dimers [137, 138]. Furthermore, we find that the DGTD calculations confirm our prediction that the scattering cross-section becomes more important at the expense of the absorption cross-section for the SRR dimer for small separations as shown in Fig. 7.10: in contrast to the reference [dashed curves in Figs. 7.10(a)-(d)], for which the absorption cross-section (red) exceeds the scattering cross-section (blue), for all SRR dimer configurations (solid curves), the scattering cross-section dominates.

7.3 Conclusion

In conclusion, we have measured the absolute extinction-cross-section spectra of individual magnetic SRRs of a specific design to be about one-seventh of the square of the reso-

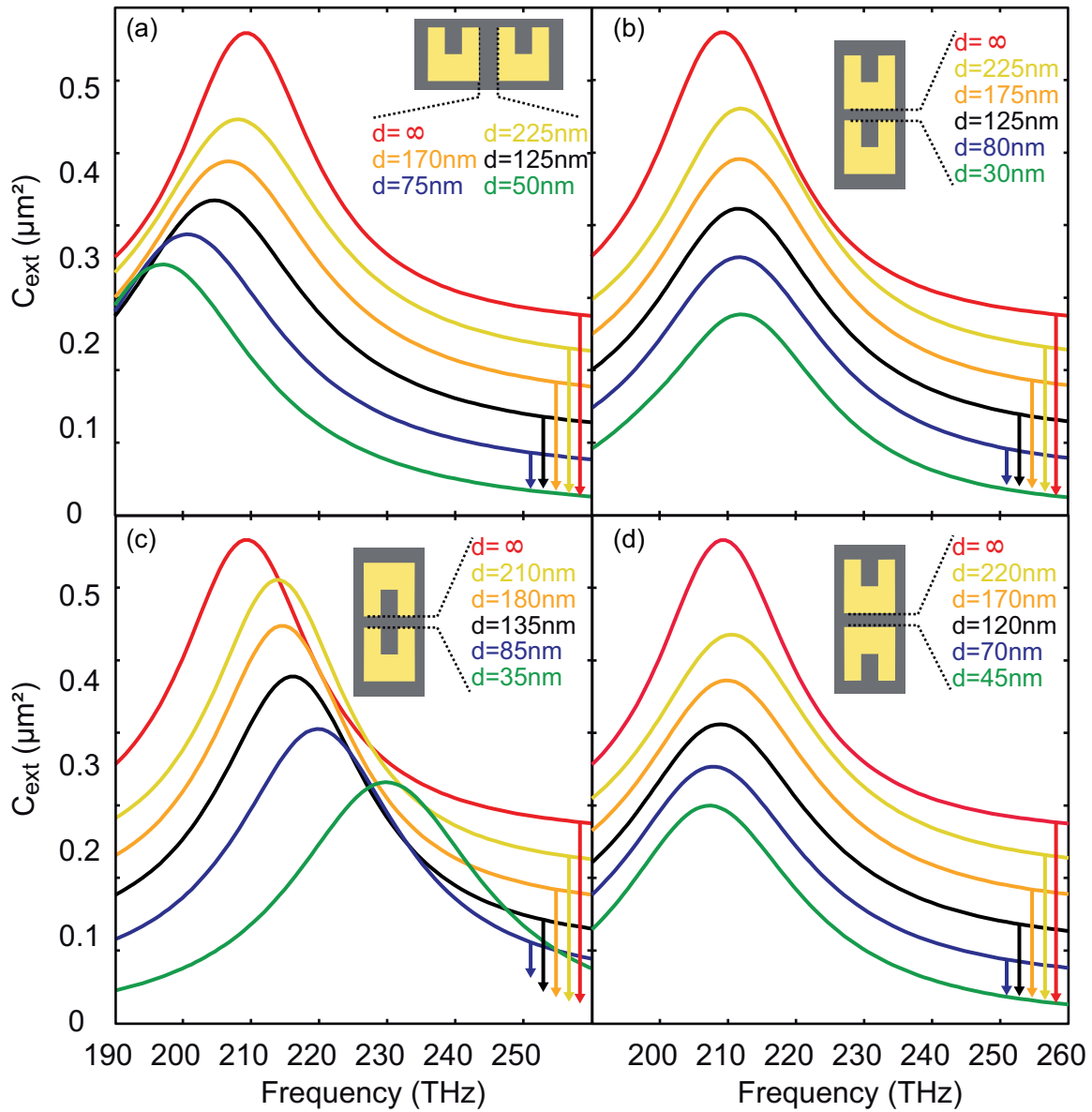


Figure 7.9: Calculated extinction-cross-section spectra of four different sets of SRR dimers. The geometries and separations of the SRRs correspond to the experiments in Fig. 7.8. The different curves in each set are vertically displaced for clarity (see arrows). (a) Side-by-side configuration, (b) on-top configuration, (c) gap-to-gap configuration, and (d) back-to-back configuration.

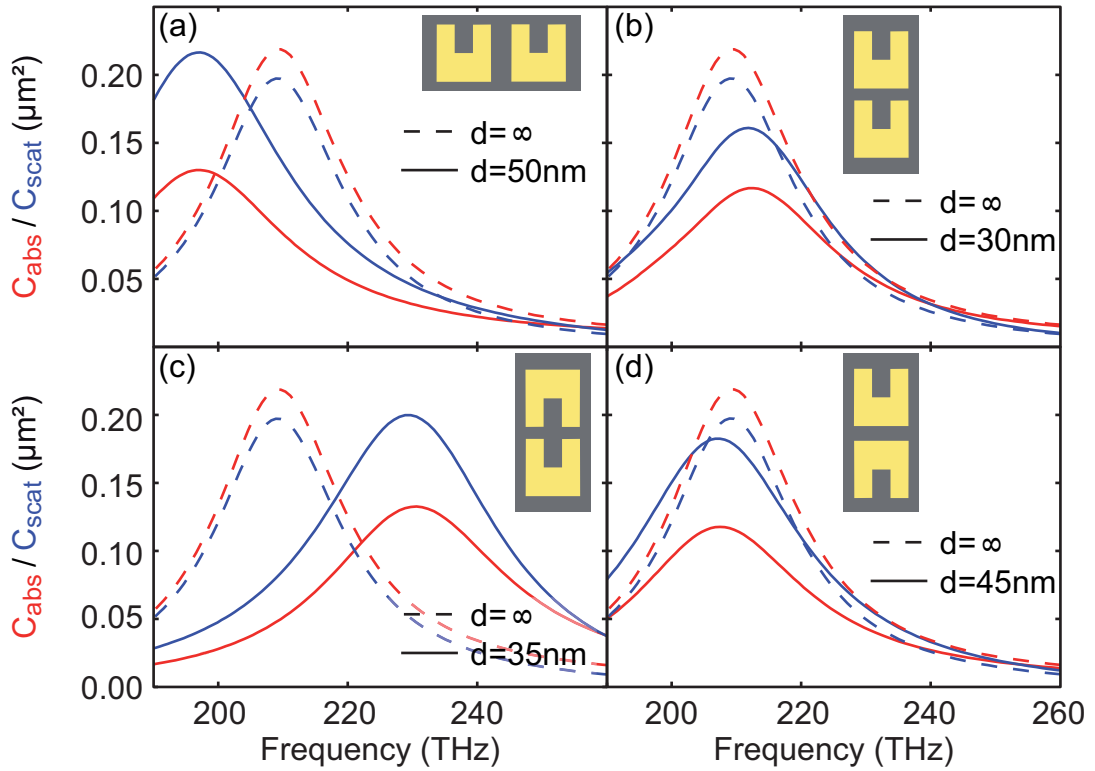


Figure 7.10: Calculated absorption- (red) and scattering- (blue) cross-section spectra for the different SRR dimers with the smallest separations (solid lines) compared to the reference ($d = \infty$, dashed lines). For each configuration, the scattering cross-section wins at expense of the absorption cross-section when the inner-dimer distance is reduced.

nance wavelength at $\lambda = 1.4 \mu\text{m}$ using a modulation technique. For the investigated design, theoretical analysis shows that the absorption cross-section and the scattering cross-section contribute, respectively, one-third and two-thirds of that value. Theoretical analysis of the experiments further reveals that the relative influence of the substrate (half-space geometry) on the extinction cross-section of the metal nanoparticle at the interface can be as large as 30 %.

Furthermore, we have experimentally and theoretically investigated the coupling mechanisms of SRR dimers by means of their extinction-cross-section spectra. We find that the dimer's resonance frequency shifts with increasing SRR separation. The direction of this shift depends on the orientation of the SRRs in the dimer. The measured (calculated) frequency shift for the gap-to-gap configuration can be as large as 8 % (10 %) of the resonance frequency of the corresponding single SRR. Even stronger effects are observed with respect to the quality factor of the dimer's coupled mode. Here, we find for the side-by-side configuration a maximum reduction of the quality factor of 37 % (30 %) compared to the quality factor of a single SRR in our experiments (calculations). An intuitive dipole-dipole interaction model taking electric and magnetic dipoles into account, qualitatively explains the frequency shifts. Our results imply that the in-plane interaction between SRRs strongly influences the optical properties of two dimensional metamaterial arrays.

Chapter 8

Mapping particle plasmons of split-ring resonators

Hitherto, most experimental studies on photonic metamaterials and on metallic nanoparticles completely rely on far-field optical investigations [38, 71, 138]. Thus, for gaining information about the occurring modes on length scales that correspond to the optical near fields, *i.e.*, a couple of nanometers, we have to apply numerical calculations. However, experimentally obtained information about the electromagnetic near fields on length-scales well below the operating wavelength of the nano-optical device can provide additional physical insights: many optical phenomena and devices that are promising candidates for future applications like surface enhanced Raman spectroscopy [150], biosensing [151], or the surface plasmon amplification by stimulated emission of radiation (spaser) [152–154] require precise experimental knowledge of the electromagnetic near-field distribution in order to improve their characteristics and in order to understand the underlying physics.

Indeed, recently the amplitude- and phase-resolved near fields of SRR arrays have been mapped with an apertureless scanning near-field microscope at a fixed wavelength of $2.65\ \mu\text{m}$ [155]. Here, we apply a different method to map the plasmonic modes of individual SRRs with resonance frequencies in a different spectral range. We utilize, that not only light waves but also fast electrons can be used for exciting optical modes. In this context, EELS has proven to be the method of choice for probing the electromagnetic near fields in the optical spectral range [49, 106, 107]. In short (the full discussion can be found in section 5.4), EELS utilizes a tightly focused (diameter of $< 1\ \text{nm}$) electron beam, which is scanned over a specimen. After interacting with the specimen, the electrons are energetically discriminated by means of an electron spectrometer and an attached CCD camera. Finally, we obtain a 2D map that displays the spatially resolved electron-energy-loss probability for a specific energy loss. In section 2.4 and Refs. [50, 53, 54], it has been shown that the electron-energy-loss probability is related to the absolute electric field projected on the (z -) direction of the electron beam. A detailed analysis reveals that the electron-energy-loss probability can be interpreted as the projected electromagnetic local density of states [53].

In the case of quasi-planar metallic nanostructures like SRRs, for which the eigenmodes are directly connected to lateral current and charge oscillations, we can explain the positions of

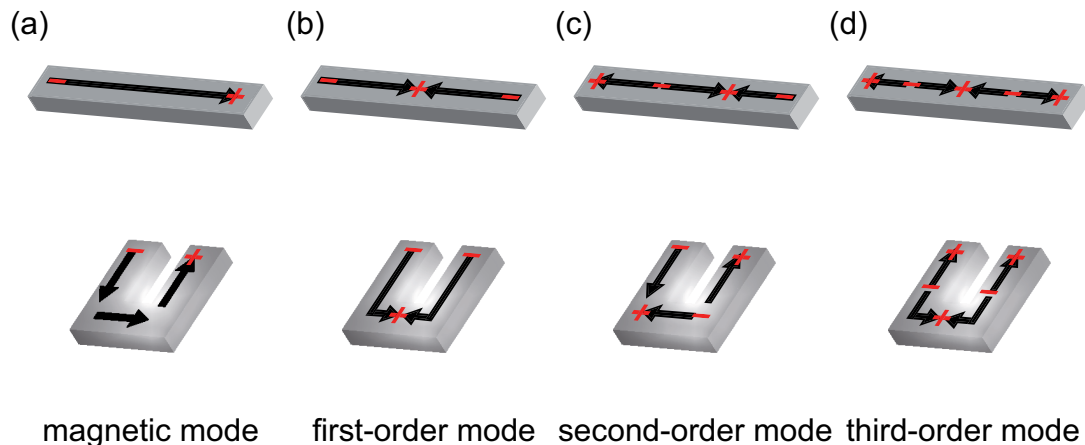


Figure 8.1: Eigenmodes of a straight antenna illustrated by their currents (black arrows) and the corresponding charge accumulations / depletions (red signs) in direct comparison to the eigenmodes of an SRR. (a) Magnetic mode (the oscillating ring current leads to a magnetic dipole moment), (b) first-order mode, (c) second-order mode, and (d) third-order mode. We expect high EELS signals at the antinodes of the corresponding charge oscillations that are depicted as red signs in the SRR sketch.

high or low EELS signal in a more tangible way: at the antinodes of the charge distribution (at these antinodes, charges accumulate and deplete), we clearly have a large z -component of the electric field leading to high EELS signals.

In this chapter, we present our EELS experiments performed on SRRs made of silver. The experiments have been conducted by our collaborators G. Boudarham, M. Kociak, and C. Colliex in the group of O. Stéphan in Paris, France.

8.1 The split-ring resonator's eigenmodes in the antenna model

As already discussed in section 3.3 and in Refs. [38,69], SRRs can be viewed as tiny resonant electromagnets that, if they are sufficiently small, exhibit their fundamental resonance in the optical spectral range. An external light field oscillating at this resonance frequency can induce a resonant ring current that generates a magnetic dipole moment. In an intuitive (but clearly simplifying) model, the optical properties of SRRs can qualitatively be described as LC -circuit composed of a coil with one winding and a capacitor. Referring to this context, for the magnetic resonance, the term LC -resonance is frequently used.

In optical experiments [38], additional to the magnetic mode, higher-order modes of SRRs have been observed. Unfortunately, the occurrence of these higher-order modes can not be explained by the intuitive LC -circuit model. Clearly, a quantitative description of the higher-order modes requires the full microscopic numerical calculations. Alternatively, we describe the SRR as a straight antenna whose ends are folded upwards as illustrated in Fig. 8.1. In this model, the well-known eigenmodes of the straight antenna can be directly transferred to the eigenmodes of the SRR. For the fundamental mode, the current distribution is sketched in

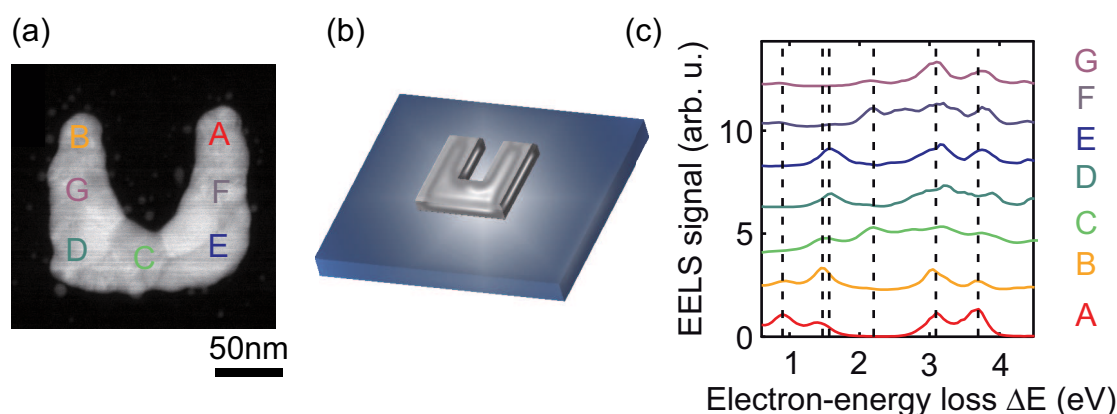


Figure 8.2: (a) Electron micrograph of the investigated SRR. (b) Sketch of the specimen consisting of the SRR (gray) on top of a 30 nm-thin Si₃N₄-membrane (blue). (c) Representative set of electron-energy-loss spectra (vertically shifted for clarity) taken at different positions of the electron beam that are marked as capital letters, which are directly related to the positions marked in (a).

Fig. 8.1(a). We observe two nodes in the current distribution at the two ends of the antenna and the SRR (the current distribution in the SRR's fundamental mode shows nicely the ring-current aspect leading to the out-of-plane magnetic dipole moment). Translated to the charge oscillations of this mode: at the nodes of the current distributions, we obtain antinodes in the charge distribution and here we expect high EELS signals (depicted as red signs in Fig. 8.1). At one end, charges will accumulate and clearly, at the other end, there will be a depletion of charges – the mode is antisymmetric.

For the higher-order modes, the corresponding current and charge distributions exhibit more nodes: one additional current node appears at the mirror axis of the antenna / SRR in the first-order mode [see Fig. 8.1(b)]. Consequently, the first-order mode is symmetric.

The current distribution of the second-order mode exhibits two nodes inside the volume of the antenna / SRR as illustrated in Fig. 8.1(c). For the SRR, the nodes are located at the corners leading to charge accumulation / depletion. Hence, the second-order mode is antisymmetric.

Finally, the third-order mode's current distribution exhibits five nodes and according to the above reasonings, the mode is symmetric. The corresponding charge distribution has five sites of charge accumulation / depletion: one at each end, one at the symmetry axis and one in the middle of each side wire.

8.2 Results and discussion

We have performed EELS on a silver SRR, which is placed on top of a thin Si₃N₄-membrane. A corresponding electron micrograph is shown in Fig. 8.2(a). The SRR's lateral dimensions can be directly deduced from this micrograph, the thickness of the evaporated silver layer is nominally 20 nm. As sketched in Fig. 8.2(b), the SRR is located on a 30 nm-thin Si₃N₄-membrane, which is indicated by the thin blue layer with the gray SRR on top. Hence, the

entire thickness of the specimen is 50 nm – thin enough for performing meaningful EELS measurements. All details of the fabrication procedure are presented in section 4.1.6. Figure 8.2(c) depicts a representative set of electron-energy-loss spectra which are taken at different positions. They are indicated by the capital letters and can be directly compared to the letters in Fig. 8.2(a). Here, we can identify a number of excitations (modes) that clearly depend on the position of the electron beam. The data are obtained by the experimental setup presented in section 5.4. As discussed in the same section, due to the overwhelming ZLP in the spectral region of interest, we have to apply an elaborate numerical analysis in terms of deconvolving the raw data by the RL algorithm. The depicted loss spectra are obtained after 50 iteration steps of the RL algorithm.

From the deconvolved raw data depicted in Fig. 8.2(c), we can identify six modes. Four of them (spectrally located at $\Delta E = 0.89$ eV, $\Delta E = 1.50$ eV, $\Delta E = 1.63$ eV, and $\Delta E = 2.25$ eV) are uniquely related to eigenmodes of the SRR (see below). The other two modes [at (i) $\Delta E = 3.13$ eV and (ii) $\Delta E = 3.80$ eV, respectively] originate (i) from the excitation of surface plasmon polaritons at the silver-Si₃N₄ interface, the so-called interface mode and (ii) from the excitation of the bulk plasmon, that is, the oscillation of all electrons of the metal's free-electron gas with respect to the positively charged ionic background [156]. These two modes do not show a noteworthy variation over the SRR.

For each mode, we gain a 2D map [see Figs. 8.3(a) - (d)] of the EELS signal by fitting a Gaussian to the peaks that occur in the loss spectra. The amplitude of the fitted Gaussian is then color-coded in the 2D map. For interpreting the mapped plasmonic eigenmodes of the SRR, we recall that we expect the measured EELS signal to peak where the charge oscillations of the eigenmodes have antinodes corresponding to the nodes of the current distributions. We observe the lowest-energy mode at an energy loss of $\Delta E = 0.89$ eV. The corresponding 2D map [see second row of Fig. 8.3(a)] exhibits a peak at the tip of each side wire of the SRR. Hence, we can identify this mode to be the magnetic mode of the SRR, for which we argued above to be antisymmetric whereas the EELS-signal is symmetric.

Evidently, we can also identify the higher-order modes, namely the first-, second- and third-order eigenmodes at $\Delta E = 1.50$ eV, $\Delta E = 1.63$ eV, and $\Delta E = 2.25$ eV, respectively. The corresponding 2D maps are shown in Figs. 8.3(b) - (d). The first-order mode at $\Delta E = 1.5$ eV is established by three EELS peaks, one rather diffuse peak located around the symmetry axis of the SRR and again one (very localized) peak at each tip. As discussed, this mode is of symmetric nature. For the second-order mode at $\Delta E = 1.63$ eV [see Fig. 8.3(c)], we find the four expected peaks in the EELS signal. Here, the peaks at the tips are rather weak in comparison to the peaks at the corner of the SRR leading to a mode of antisymmetric nature. Similarly, the 2D map of the third-order eigenmode at $\Delta E = 2.25$ eV exhibits only three distinct EELS peaks. Those expected peaks in the EELS signal at the tips are too weak to be detected¹. Nevertheless, we clearly recognize the main characteristics of the third-order mode – the peak in the middle of each side wire and the peak at the symmetry axis.

¹Preliminary numerical calculations (not shown here) affirmed that these two naively expected EELS peaks are much weaker than the others.

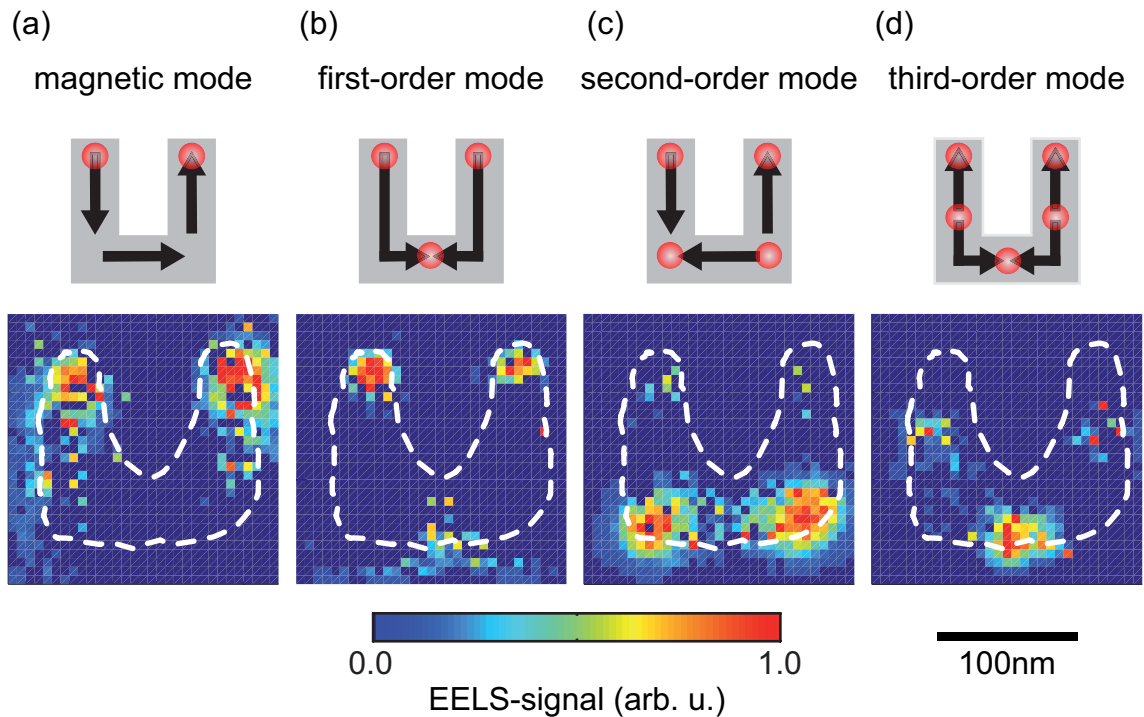


Figure 8.3: First row: current distribution of the SRR eigenmodes deduced from the antenna model (black arrows). Additionally, the positions where we expect high EELS signals are indicated as red dots. Second row: 2D maps of the measured EELS signal at energy losses of $\Delta E = 0.89$ eV, $\Delta E = 1.50$ eV, $\Delta E = 1.63$ eV, and $\Delta E = 2.25$ eV in (a), (b), (c), and (d), respectively.

8.3 Conclusion

For spatially mapping the plasmonic modes in individual SRRs, we used EELS – a technique that has already proven its applicability to other plasmonic nanoparticles [49, 106, 107]. We could identify four SRR eigenmodes: (i) the fundamental, so-called magnetic mode, (ii) the first-order, so-called vertical-electric mode, (iii) the second-order, horizontal-electric mode, and (iv) the third-order mode. Our results can be qualitatively understood in terms of an intuitively antenna model. Still, corresponding rigorous numerical calculations are ongoing in the group of F. J. G. de Abajo at the Instituto de Optica, CSIC in Madrid, Spain.

Our experiments can serve as the starting point for further investigations of this type on plasmonic resonances which are important for planar metamaterials. For instance, the actual near-field distributions are crucial for the occurrence of the spaser [153, 154]. Also, by this technique it might be possible to uniquely distinguish between collective modes in planar metamaterial arrays and modes that are an intrinsic property of the fundamental building blocks [157].

Chapter 9

Conclusions and outlook

In this thesis, we have investigated the nonlinear optical properties of planar metamaterial arrays and the linear optical properties of individual “photonic atoms”; metallic nanostructures with extraordinary optical properties. In detail, we have studied the second- and third-harmonic generation of arrays of complementary split-ring resonators (CSRRs). Our experiments in combination with corresponding microscopic numerical calculations contribute to the identification of the dominant nonlinear source terms in metallic nanostructures. In the second part of this work, we have investigated the linear optical properties of isolated split-ring resonators (SRRs) as well as the interaction effects in pairs of SRRs by means of their absolute extinction-cross-section spectra. Our results provide both quantitative knowledge about the optical properties of isolated SRRs and insight to lateral coupling mechanisms of SRRs. The coupling mechanisms observed influence the optical properties of SRR arrays which are widely used as magnetic metamaterials. Furthermore, we have used the superior resolution capabilities of a scanning-transmission-electron microscope for mapping the SRR’s particle plasmons by means of electron-energy-loss spectroscopy (EELS).

For the fabrication of the metallic nanostructures, we have used state-of-the-art electron-beam lithography resulting in a polymer template textured at the nanometer scale. The templates have been metalized by evaporating thin layers of gold or silver. After a subsequent lift-off procedure, we have obtained high-quality metallic nanostructures with sub-20 nm-feature sizes. Within this work, we have modified the standard fabrication technology to enable the fabrication of photonic atoms on ultra-thin (30 nm) substrates which are required for meaningful EELS measurements.

First nonlinear optical experiments by means of second- and third-harmonic generation (SHG and THG, respectively) on planar SRR arrays were carried out by M. W. Klein *et al.* in Refs. [16–18]. The SHG results on SRRs could qualitatively be explained by considering only the magnetic part of the Lorentz force density as the primary SHG source term within the hydro-dynamic approach. The relative SHG strength was also correlated with the occurrence of an out-of-plane magnetic dipole moment. All investigated metallic nanostructures in Ref. [17] seemed to enforce this interpretation.

In this work, we have attempted to test the interpretation by investigating the nonlinear optical properties of metallic nanostructures that have different linear optical properties, espe-

cially different electric and magnetic near-field distributions but the same symmetry which is an important aspect in nonlinear optics. These conditions are fulfilled by CSRRs which essentially are U-shaped holes in a thin metallic film. The linear optical properties of SRRs and CSRRs are related through the generalized Babinet principle [2, 129, 130]. In short, transmittance and reflectance change role when the exciting polarization is rotated by 90 degrees. Our experiments revealed that the SHG intensity from resonantly excited CSRR arrays is 80 % of the SHG intensity from resonantly excited planar SRR arrays. In contrast to SRR arrays, according to Babinet's principle, there is no out-of-plane magnetic dipole moment for CSRR arrays which exhibit an SHG intensity of similar strength. Our experimental results lead us to conclude that there is generally no correlation between SHG efficiency and the out-of-plane magnetic dipole moment. This correlation exists for all of the previous experiments [16–18], yet it is wrong in general.

Corresponding microscopic numerical calculations based on the hydro-dynamic model could not only qualitatively but also quantitatively reproduce our experimentally determined SHG conversion efficiencies. The good agreement between experiment and theory has encouraged us to determine the dominant SHG source terms of SRRs (CSRRs) with the help of artificially switching on and off the different SHG source terms in the numerical calculations. We find that the so-called convective term accounts for about 68% (81%) of the SHG source current density. The corresponding source term based on the magnetic part of the Lorentz force [16] shows a similar qualitative behavior but accounts for only about 2% (2%) of the overall SHG source current density.

Regarding possible applications, the CSRRs are advantageous in that they reveal a transmittance maximum at the fundamental resonance rather than a minimum for the SRRs. This larger transmittance potentially allows for stacking several layers along the propagation direction of light [134], thereby enhancing the SHG conversion efficiency.

Still, the question which nonlinear source term in metallic nanostructures dominates is under controversial debate [47, 132, 133]. Thus, further experiments are required. For instance, continuously changing the wavelength of the excitation would deliver spectroscopic data that can be compared to theory. Another important experiment to tackle this question is the investigation of the nonlinear optical properties of single metallic nanostructures. In this experiment, the exact geometry of the nanostructure can be measured (for instance by atomic force microscopy) and can be fed into the numerical simulations. Thus, such an experiment would allow for excluding SHG from artifacts like the so-called lightning-rod effect. Also, for single nanostructures the SHG radiation pattern can be measured by imaging the Fourier plane of a high-numerical-aperture objective lens onto a CCD camera. This experiment would provide further information about possible higher-order-multipole contributions to the SHG radiation pattern that can be compared to theoretical approaches.

In our experiments on linear optical properties of individual photonic atoms, we have investigated individual SRRs and the interaction effects in pairs of SRRs. As already pointed out, the optical properties of metamaterials are mainly determined by the properties of their individual building blocks. Still, interaction effects between these individual building blocks are known to play a crucial role [78, 135, 136]. Thus, in order to learn about their individual properties, it is clearly favorable to investigate the optical properties of isolated photonic

atoms instead of arrays of photonic atoms. In a periodic arrangement, effects like far-field and near-field coupling can alter their individual optical properties and even dominate the overall optical properties of the metamaterial [137–139].

We have conducted the measurements with a sophisticated spatial modulation technique that allows for determining the absolute extinction-cross-section spectrum. Other common spectroscopy methods like dark-field and attenuated-total-internal-reflection spectroscopy provide, besides the resonance wavelength and the resonance width, only qualitative information about the scattering strength of the investigated individual nanoparticle.

First, we have studied the linear optical properties of individual SRRs. Their absolute extinction cross-section in the magnetic resonance is about a factor of eight larger than the actual geometrical area covered by the SRR and about one-seventh of the square of the resonance wavelength at $\lambda = 1.4 \mu\text{m}$. We could explain the excess of the extinction cross-section with respect to the geometrical area by modeling the SRR as an LC -circuit and calculating its extinction cross-section. Additionally, our experimental results are in very good agreement with microscopic numerical calculations. Within these calculations, it has been possible to determine the absorption and scattering cross-sections which are not experimentally accessible. The theoretical analysis shows that the absorption cross-section and the scattering cross-section contribute one-third and two-thirds of the extinction cross-section, respectively. Theoretical analysis of the experiments further reveals that the extinction cross-section of an SRR placed in a homogeneous medium can be 30 % larger than in half-space geometry required in our experimental setup.

The large extinction cross-section of isolated SRRs is a strong hint that coupling of SRRs in planar arrays changes their optical properties. For a deeper understanding, we have experimentally and theoretically investigated the coupling mechanisms in planar pairs of SRRs by means of their extinction-cross-section spectra. In analogy to pairs of atoms, we call them SRR dimers. We have found that the dimer's resonance frequency shifts with increasing SRR separation. The direction of this shift depends on the orientation of the SRRs in the dimer. The measured (calculated) frequency shift can be as large as 8 % (10 %) of the resonance frequency of the corresponding single SRR. Even stronger effects have been observed with respect to the quality factor of the dimer's coupled mode. We have also found a maximum reduction of the quality factor of 37 % (30 %) compared to the quality factor of a single SRR in our experiments (calculations). An intuitive dipole-dipole interaction model taking electric and magnetic dipoles into account, qualitatively explains the frequency shifts. Our results confirm that the in-plane interaction between SRRs strongly influences the optical properties of two-dimensional metamaterial arrays.

A major step in the investigation of isolated metallic nanoparticles would be the experimental determination of the scattering cross-section, which is not accessible by our current setup. Precisely, measuring the scattering cross-section for dipole-dominated scattering can be translated into the experimental determination of the absolute value of the vector-scattering amplitude – the current experiment only provides the real part. However, one could utilize the Gouy phase to introduce a phase shift between the scattered and the incident electric field by axially shifting the scatterer. The signal acquired at different axial positions of the scatterer provides quantitative knowledge of the imaginary part of the vector-scattering

amplitude. Another attempt to introduce such a phase shift is to use an interferometer-based setup.

Clearly, there is almost an infinite number of systems that can be investigated by the spatial modulation technique. For instance, the transition from an isolated photonic atom to an array of photonic atoms can be studied. Another possibility is to search for Fano resonances in coupled metallic nanostructures [158, 159]. Here, both nanostructures have the same resonance frequency but different damping. Thus, asymmetric resonances in the extinction-cross-section spectra accompanied by spectral regions of relatively small extinction cross-section will occur. In this case also, the determination and comparison of both the absolute extinction and scattering cross-section would be very interesting.

Hitherto, most experiments on photonic metamaterials and photonic atoms have been done by means of far-field optical measurements. However, it is equally interesting to investigate their optical near fields which otherwise are only accessible *via* numerical calculations. For spatially mapping the plasmonic modes in individual SRRs, we have used EELS, a technique that has already proven its applicability to mapping plasmonic modes in other metallic nanoparticles [49, 106, 107]. In our experiments, we have mapped four eigenmodes of the studied SRR for the first time: (i) the fundamental, so-called magnetic mode, (ii) the first-order, vertical-electric mode, (iii) the second-order, horizontal-electric mode, and (iv) the third-order mode. The recorded maps and the identification of the modes could be qualitatively explained in terms of an intuitive antenna model.

Our experiments can serve as the starting point for further investigations of this type on plasmonic resonances that are important for planar metamaterials. For instance, the actual near-field distribution are crucial for the occurrence of the spaser [153, 154]. Also, by this technique it is possible to uniquely distinguish between collective modes in planar metamaterial arrays and modes that are an intrinsic property of the fundamental building blocks. In combination with cathodoluminescence, the identification of dark, *i.e.*, non-radiating modes should be possible [157]. These experiments, and by additionally investigating the optical far-field properties with our sophisticated modulation technique, might serve as additional input to the exact interpretation of the connection between the EELS signal and the electromagnetic local density of states [53, 54].

Appendix A

Derivation of the Optical Theorem

We recall, that for deriving the Optical Theorem [Eq. (2.30)], we discuss an incident plane wave with an electric field \mathbf{E}_i impinging onto a small particle that absorbs parts of the incident power; the rest is scattered. In the far field, the scattered wave is a spherical wave with the electric field $\mathbf{E}_s = \frac{\exp(ikr)}{-ikr} \mathbf{X}(\theta, \phi) E_i$. Here, $\mathbf{X}(\theta, \phi)$ is the vector scattering amplitude. The extinguished power reads

$$P_{\text{ext}} = P_{\text{scat}} + P_{\text{abs}} = \int_A (\mathbf{S}_{\text{scat}} - \mathbf{S}_{\text{tot}}) \cdot \mathbf{u}_r dA, \quad (\text{A.1})$$

where $\mathbf{S} = \frac{1}{2} \text{Re}(\mathbf{E} \times \mathbf{H}^*)$ is the Poynting vector, A denotes a closed surface around the small particle, and \mathbf{u}_r is the unit vector in r -direction. Again, the magnetic field can be retrieved from the electric field by the relation $\mathbf{H} = \frac{k}{\mu_0 \omega} \mathbf{u}_k \times \mathbf{E}$, where \mathbf{u}_k is the unit vector in the direction of the wave vector \mathbf{k} .

Thus,

$$\mathbf{S}_{\text{scat}} - \mathbf{S}_{\text{tot}} = -\frac{1}{2} \text{Re} \left\{ \mathbf{E}_i \times \mathbf{H}_i^* + \frac{k}{\mu_0 \omega} [\mathbf{E}_s \times (\mathbf{u}_z \times \mathbf{E}_i^*) + \mathbf{E}_i \times (\mathbf{u}_r \times \mathbf{E}_s^*)] \right\}. \quad (\text{A.2})$$

The condition that no net energy enters or leaves the volume enclosed by the surface A , precisely, $\int_A \text{Re}(\mathbf{E}_i \times \mathbf{H}_i^*) \cdot \mathbf{u}_r dA = 0$, leads to

$$P_{\text{ext}} = -\frac{k}{2\mu_0 \omega} \int_A \text{Re} [\mathbf{E}_s \times (\mathbf{u}_z \times \mathbf{E}_i^*) + \mathbf{E}_i \times (\mathbf{u}_r \times \mathbf{E}_s^*)] \cdot \mathbf{u}_r dA. \quad (\text{A.3})$$

Applying the Jacobi identity and $\mathbf{u}_r \cdot \mathbf{E}_s = 0$ (the scattered field is transverse in the far field), yields

$$P_{\text{ext}} = -\frac{k}{2\mu_0 \omega} \int_A \text{Re} [\mathbf{u}_z \cdot \mathbf{u}_r (\mathbf{E}_s \cdot \mathbf{E}_i^*) - \mathbf{E}_i^* \cdot \mathbf{u}_r (\mathbf{u}_z \cdot \mathbf{E}_s) + \mathbf{E}_i \cdot \mathbf{E}_s^*] dA. \quad (\text{A.4})$$

Assuming the incident field to be x -polarized, that is, $\mathbf{E}_i = E_i \mathbf{u}_x$ gives

$$P_{\text{ext}} = -\frac{E_i^2}{2r\mu_0 \omega} \int_A \text{Re} \left\{ i \left[\exp(ik(r-z)) \cos \theta \mathbf{u}_x \cdot \mathbf{X}(\theta, \phi) - \exp(ik(r-z)) \sin \theta \cos \varphi \mathbf{u}_z \cdot \mathbf{X}(\theta, \phi) - \exp(-ik(r-z)) \mathbf{u}_x \cdot \mathbf{X}^*(\theta, \phi) \right] \right\} dA. \quad (\text{A.5})$$

With $z = r \cos \theta$ and $dA = -r^2 d \cos \theta d\varphi$, it becomes obvious that we have integrals of the form $\int_{-1}^1 \exp(ikr\alpha) f(\alpha) d\alpha$, that can be solved by partial integration, leading to

$$\int_{-1}^1 \exp(ikr\alpha) f(\alpha) d\alpha = \left[\frac{1}{ikr} \exp(ikr\alpha) f(\alpha) \right]_{\alpha=-1}^1 - \underbrace{\int_{-1}^1 \frac{\exp(ikr\alpha)}{ikr} \frac{\partial f(\alpha)}{\partial \alpha} d\alpha}_{\mathcal{O}\left(\frac{1}{(ikr)^2}\right)}. \quad (\text{A.6})$$

The second term vanishes in the far field for $kr \rightarrow \infty$. Thus,

$$P_{\text{ext}} = -\frac{E_i^2}{2kr^2\mu_0\omega} \int \text{Re} \left\{ \exp(ikr) \left\{ -\exp(-ikr) [\mathbf{u}_x \cdot \mathbf{X}(\theta = 0)] - \exp(ikr) [\mathbf{u}_x \cdot \mathbf{X}(\theta = \pi)] \right\} - \exp(-ikr) \left\{ \exp(ikr) [\mathbf{u}_x \cdot \mathbf{X}(\theta = 0)] - \exp(-ikr) [\mathbf{u}_x \cdot \mathbf{X}(\theta = \pi)] \right\} \right\} r^2 d\varphi. \quad (\text{A.7})$$

After some basic algebra, we find

$$P_{\text{ext}} = -\frac{E_i^2}{2k\mu_0\omega} \text{Re} \left\{ \int -2\text{Re} [\mathbf{u}_x \cdot \mathbf{X}(\theta = 0)] + 2i\text{Im} \left\{ \exp(-2ikr) [\mathbf{u}_x \cdot \mathbf{X}^*(\theta = \pi)] \right\} d\varphi \right\}. \quad (\text{A.8})$$

Clearly, the integration over φ yields a factor 2π . Then Eq. (A.8) directly leads to the Optical Theorem (considering that the intensity I of the incoming plane wave is given by $I = \frac{E_i^2 k}{2\omega\mu_0}$)

$$P_{\text{ext}} = I \frac{4\pi}{k} \text{Re} [\mathbf{u}_x \cdot \mathbf{X}(\theta = 0)]. \quad (\text{A.9})$$

In words: the power that is extinguished from the incident beam equals the real part of the projected vector scattering amplitude, evaluated in forward direction. From here, we can easily deduce Eq. (2.30)

$$C_{\text{ext}} = \frac{P_{\text{ext}}}{I} = \frac{4\pi}{k^2} \text{Re} [\mathbf{u}_x \cdot \mathbf{X}(\theta = 0)]. \quad (\text{A.10})$$

Appendix B

Analysis of the spatial modulation experiment – step by step

In this appendix, we explicitly derive Eqs. (5.9) and (5.13). Both equations are essential for analyzing the experimental data that we obtain from the spatial modulation set-up (see section 5.3). Equation (5.9) describes the connection between the measured relative signal drop $\Delta P/P_0$ and the absolute value of the extinction cross-section. Equation (5.13) describes the signal drop, when the small particle is placed off-axis but still in the focal plane of a Gaussian beam.

B.1 A small particle in a Gaussian focus

As in the discussion in section 5.3, we first aim for the power P_0 that reaches the detector when illuminated by a Gaussian beam, with the beam waist radius w_0 , Rayleigh length z_R and maximum electric field strength E_0 . In the far field where $\rho/z \approx \theta$ (here $\rho = \sqrt{x^2 + y^2}$), we can write the electric field distribution of the Gaussian beam in spherical coordinates. Additionally, we assume a small numerical aperture NA_B of the Gaussian beam, leading to $w_0/z_R \approx \text{NA}_B$ and $z \approx r$ (here r denotes the distance from the focus). Herewith, we find for the electric field distribution in the far field

$$\mathbf{E}_i(r, \theta) = \mathbf{u}_{xz} E_0 \frac{z_R}{ir} \exp\left(-\frac{\theta^2}{\text{NA}_B^2}\right) \exp(ikr). \quad (\text{B.1})$$

Here, \mathbf{u}_{xz} with $\mathbf{u}_{xz} \cdot \mathbf{u}_r = \mathbf{u}_{xz} \cdot \mathbf{u}_y = 0$ denotes the direction of the electric field vector when the field in the focal plane is x -polarized.

For calculating the power that impinges onto the detector, we need to integrate the Poynting vector \mathbf{S} over the solid angle that is covered by the collecting microscope objective lens with numerical aperture NA_D

$$P_0 = \int_{\theta < \text{NA}_D} d\Omega r^2 \mathbf{S} \cdot \mathbf{u}_r = \int_{\theta < \text{NA}_D} d\Omega r^2 \frac{1}{2} \text{Re}(\mathbf{E}_i \times \mathbf{H}_i^*) \cdot \mathbf{u}_r. \quad (\text{B.2})$$

With $\mathbf{H}_i = \frac{\mathbf{u}_r \times \mathbf{E}_i}{\mu_0 c}$, we find

$$P_0 = \int_{\theta < \text{NA}_D} d\Omega \frac{r^2}{2} \text{Re} \left[\frac{E_0^2 z_R^2}{r^2 c \mu_0} \exp \left(-2 \frac{\theta^2}{\text{NA}_B^2} \right) \right] [\mathbf{u}_{xz} \times (\mathbf{u}_r \times \mathbf{u}_{xz})] \cdot \mathbf{u}_r. \quad (\text{B.3})$$

Applying the Jacobi identity to the vector product leads to two terms of which only one term is non zero, namely the one proportional to \mathbf{u}_r . Performing the integration over $d\varphi$ generates only a prefactor of 2π . Thus, only the integration over $d\theta$ remains

$$P_0 = \frac{E_0^2 z_R^2 \pi}{c \mu_0} \int_{\theta < \text{NA}_D} \sin \theta d\theta \exp \left(-2 \frac{\theta^2}{\text{NA}_B^2} \right). \quad (\text{B.4})$$

We assume that the exponential term decays much faster than $\sin \theta$ varies, thus we can set $\sin \theta \approx \theta$. Additionally, this assumption allows us to expand the boundaries to $\theta = 0 \dots \infty$

$$P_0 = \frac{E_0^2 z_R^2 \pi}{c \mu_0} \int_{\theta=0}^{\infty} \theta \exp \left(-2 \frac{\theta^2}{\text{NA}_B^2} \right) d\theta. \quad (\text{B.5})$$

With the substitution $x = 2 \frac{\theta^2}{\text{NA}_B^2}$, the integral is easy to solve and finally we obtain the power of the Gaussian beam

$$P_0 = \frac{E_0^2 z_R^2 \pi}{4c \mu_0} \text{NA}_B^2. \quad (\text{B.6})$$

In our experimental set-up, we move a scattering particle periodically in and out of the focus. The measured quantity is the signal drop $\Delta P = P_0 - P_{\text{part}}$ that occurs when the particle is moved into the focus. The electric field that reaches the detector is then $(\mathbf{E}_i + \mathbf{E}_s)$. Thus, the power P_{part} that reaches the detector when the particle is in the Gaussian focus is given by

$$\begin{aligned} P_{\text{part}} &= \int_{\theta < \text{NA}_D} d\Omega \frac{r^2}{2} \text{Re} [(\mathbf{E}_i + \mathbf{E}_s) \times (\mathbf{H}_i + \mathbf{H}_s)^*] \cdot \mathbf{u}_r \\ &= \int_{\theta < \text{NA}_D} d\Omega \frac{r^2}{2} \text{Re} \left(\underbrace{\mathbf{E}_i \times \mathbf{H}_i^*}_{=P_0} + \mathbf{E}_i \times \mathbf{H}_s^* + \mathbf{E}_s \times \mathbf{H}_i^* + \underbrace{\mathbf{E}_s \times \mathbf{H}_s^*}_{\approx 0} \right) \cdot \mathbf{u}_r. \end{aligned} \quad (\text{B.7})$$

The first term is just the incident power P_0 and the last term is much smaller than all the others since the scattered fields are much smaller than the incident fields. Then we obtain as signal drop

$$\Delta P = P_0 - P_{\text{part}} = - \int_{\theta < \text{NA}_D} d\Omega \frac{r^2}{2} \text{Re} (\mathbf{E}_i \times \mathbf{H}_s^* + \mathbf{E}_s \times \mathbf{H}_i^*) \cdot \mathbf{u}_r. \quad (\text{B.8})$$

The incident electric and magnetic fields are given above, whereas the scattered electric and magnetic fields are given by Eq. (2.22). Precisely, we obtain

$$\mathbf{E}_s = E_0 \mathbf{X}(\theta, \varphi) \frac{\exp(ikr)}{-ikr} \quad \text{and} \quad \mathbf{H}_s = E_0 \frac{\exp(ikr)}{-ikr} [\mathbf{u}_r \times \mathbf{X}(\theta, \varphi)]. \quad (\text{B.9})$$

Here, $\mathbf{X}(\theta, \varphi)$ is the vector-scattering amplitude as introduced in section 2.1.5. Next, we evaluate the two terms of Eq. (B.8).

(i)

$$\begin{aligned} \mathbf{E}_i \times \mathbf{H}_s^* &= -\frac{E_0^2 z_R}{\mu_0 c k r^2} \exp \left[-\left(\frac{\theta}{\text{NA}_B} \right)^2 \right] \mathbf{u}_{xz} \times [\mathbf{u}_r \times \mathbf{X}^*(\theta, \varphi)] \\ &= -\frac{E_0^2 z_R}{\mu_0 c k r^2} \exp \left[-\left(\frac{\theta}{\text{NA}_B} \right)^2 \right] [\mathbf{X}^*(\theta, \varphi) \cdot \mathbf{u}_{xz}] \mathbf{u}_r. \end{aligned} \quad (\text{B.10})$$

Here, we applied the Jacobi identity and used $\mathbf{u}_{xz} \cdot \mathbf{u}_r = 0$.

(ii) Analogous, we obtain

$$\mathbf{E}_s \times \mathbf{H}_i^* = -\frac{E_0^2 z_R}{\mu_0 c k r^2} \exp \left[-\left(\frac{\theta}{\text{NA}_B} \right)^2 \right] [\mathbf{X}(\theta, \varphi) \cdot \mathbf{u}_{xz}] \mathbf{u}_r. \quad (\text{B.11})$$

Thus, the signal drop reads

$$\Delta P = \frac{E_0^2 z_R}{2\mu_0 c k} \int_{\theta < \text{NA}_D} d\Omega 2\text{Re} [\mathbf{X}(\theta, \varphi) \cdot \mathbf{u}_{xz}] \exp \left[-\left(\frac{\theta}{\text{NA}_B} \right)^2 \right]. \quad (\text{B.12})$$

With $d\Omega = \sin \theta d\theta d\varphi \approx \theta d\theta d\varphi$, we find

$$\Delta P = \frac{E_0^2 z_R}{\mu_0 c k} \int_0^{2\pi} \int_{\theta < \text{NA}_D} \text{Re} [\mathbf{X}(\theta, \varphi) \cdot \mathbf{u}_{xz}] \exp \left[-\left(\frac{\theta}{\text{NA}_B} \right)^2 \right] d\varphi \theta d\theta. \quad (\text{B.13})$$

For dipole scattering, we can assume that the vector-scattering amplitude varies weakly with θ and φ within the numerical aperture NA_D of the detector system. Thus, $\text{Re}(\mathbf{X}(\theta, \varphi) \cdot \mathbf{u}_{xz}) \approx \text{Re}(\mathbf{X}(\theta = 0) \cdot \mathbf{u}_x)$, where $\mathbf{X}(\theta = 0)$ denotes the vector-scattering amplitude in forward direction. This enables us to take $\text{Re}(\mathbf{X}(\theta = 0) \cdot \mathbf{u}_x)$ out of the integral and the integration over φ only results in a factor of 2π . Finally, we obtain for the signal drop

$$\begin{aligned} \Delta P &= \frac{E_0^2 z_R}{\mu_0 c k} 2\pi \text{Re} [\mathbf{X}(\theta = 0) \cdot \mathbf{u}_x] \int_{\theta < \text{NA}_D} \exp \left[-\left(\frac{\theta}{\text{NA}_B} \right)^2 \right] \theta d\theta \\ &= \frac{E_0^2 z_R}{\mu_0 c k} \pi \text{NA}_B^2 \text{Re} [\mathbf{X}(\theta = 0) \cdot \mathbf{u}_x], \end{aligned} \quad (\text{B.14})$$

where we use $\int_{\theta < \text{NA}_D} \exp \left[-\left(\frac{\theta}{\text{NA}_B} \right)^2 \right] \theta d\theta \approx \int_{\theta=0}^{\infty} \exp \left[-\left(\frac{\theta}{\text{NA}_B} \right)^2 \right] \theta d\theta = \frac{\text{NA}_B^2}{2}$.

Hence, the relative signal drop reads

$$\begin{aligned} \frac{\Delta P}{P_0} &= \frac{4}{z_R k} \text{Re} [\mathbf{X}(\theta = 0) \cdot \mathbf{u}_x] \\ &= \frac{8}{k^2 w_0^2} \text{Re} [\mathbf{X}(\theta = 0) \cdot \mathbf{u}_x], \end{aligned} \quad (\text{B.15})$$

where we used $z_R = \frac{\pi w_0^2}{\lambda} = \frac{k w_0^2}{2}$. Combining Eqs. (B.15) and (2.30) results in

$$C_{\text{ext}} = \frac{\pi w_0^2}{2} \frac{\Delta P}{P_0}. \quad (\text{B.16})$$

This is the very important result that connects the measured data with the absolute value of the extinction cross-section.

B.2 A small particle outside a Gaussian focus

In this section, we derive the signal that we obtain when the particle is in the focal plane but not in the focus. The particle's position is given by $(R, z = 0)$.

The signal drop is again given by Eq. (B.8). Similar to the preceding section, we will analyze the two terms in the integral (in order to increase the readability, we omit the factor $\exp[-(\theta/\text{NA}_B)^2]$):

(i)

$$\mathbf{E}_i \times \mathbf{H}_s^* = -\frac{E_0^2 z_R}{kr^2 \mu_0 c} \underbrace{\exp[-(R/w_0)^2]}_{(a)} \underbrace{\exp(-ikR \sin \theta \cos \varphi)}_{(b)} \underbrace{\{\mathbf{u}_{xz} \times [\mathbf{u}_r \times \mathbf{X}^*(\theta, \varphi)]\}}_{=\mathbf{u}_r [\mathbf{X}^*(\theta, \varphi) \cdot \mathbf{u}_{xz}]} \quad (\text{B.17})$$

When comparing with Eq. (B.10), there are two modifications

(a) $\exp[-(R/w_0)^2]$: the exciting field is smaller off-axis than on-axis.

(b) $\exp(-ikR \sin \theta \cos \varphi)$: an interference term that is caused through different path lengths.

(ii) Analogously, the second term finally reads

$$\mathbf{E}_s \times \mathbf{H}_i^* = -\frac{E_0^2 z_R}{kr^2 \mu_0 c} \exp[-(R/w_0)^2] \exp(ikR \sin \theta \cos \varphi) [\mathbf{X}(\theta, \varphi) \cdot \mathbf{u}_{xz}] \mathbf{u}_r. \quad (\text{B.18})$$

Combining terms (i) and (ii) yields

$$\Delta P(R) = \frac{E_0^2 z_R}{kr^2 \mu_0 c} \exp[-(R/w_0)^2] \int_{\theta < \text{NA}_D} \exp[(\theta/\text{NA}_B)^2] \dots \text{Re} \{ \exp(ikR \sin \theta \cos \varphi) [\mathbf{X}(\theta, \varphi) \cdot \mathbf{u}_{xz}] \} d\Omega. \quad (\text{B.19})$$

Further evaluation of Eq. (B.19) requires some approximations:

- Similar to the reasoning above, we assume that the exponential function decays much faster than $\sin \theta$ varies. Thus, only small values of θ contribute to the integral. This approximation allows for the following simplification

$$\begin{aligned} \exp(ikR \sin \theta \cos \varphi) &= \cos(kR \sin \theta \cos \varphi) + i \sin(kR \sin \theta \cos \varphi) \\ &\approx \cos(kR\theta \cos \varphi) + i \sin(kR\theta \cos \varphi) \\ &\approx \cos(kR\theta \cos \varphi). \end{aligned}$$

- As above, we assume that $\mathbf{X}(\theta, \varphi)$ does not vary much within the numerical aperture of the detector system. Thus, we can set

$$\mathbf{X}(\theta, \varphi) \cdot \mathbf{u}_{xz} \approx \mathbf{X}(\theta = 0) \cdot \mathbf{u}_x.$$

With these two approximations, we obtain

$$\Delta P(R) = \frac{E_0^2 z_R}{kr^2 \mu_0 c} \underbrace{\exp[-(R/w_0)^2]}_{=m_1(R)} \operatorname{Re}[\mathbf{X}(\theta=0) \cdot \mathbf{u}_x] \dots \int_{\theta=0}^{\infty} \exp[-(\theta/\text{NA}_B)^2] \theta d\theta \int_{\varphi=0}^{2\pi} \cos(kR\theta \cos \varphi) d\varphi. \quad (\text{B.20})$$

Utilizing Eq. (B.14), we obtain

$$\Delta P(R) = m_1(R) \frac{\Delta P}{\pi \text{NA}_B^2} \int_{\theta=0}^{\infty} \exp[-(\theta/\text{NA}_B)^2] \theta d\theta \int_{\varphi=0}^{\pi} \cos(kR\theta \cos \varphi) d\varphi, \quad (\text{B.21})$$

where $\Delta P = \Delta P(R=0)$. We can rewrite Eq. (B.21) by using the Bessel functions of first kind and zeroth order that reads [41]

$$J_0(x) = \frac{1}{\pi} \int_{\tau=0}^{\pi} \cos(x \sin \tau) d\tau. \quad (\text{B.22})$$

In order to reformulate the Bessel function such that we can put it into Eq. (B.21), we have to perform the substitution $\tau' = \tau + \pi/2$ ($d\tau = d\tau'$). The integration boundaries can remain unchanged since integrating $\cos(x \cos \tau')$ from 0 to π is equivalent to the integrating it from $\pi/2$ to $3\pi/2$. Additionally, we put $x = kR\theta$ and $\tau' = \varphi$. Then the Bessel function reads

$$J_0(kR\theta) = \frac{1}{\pi} \int_{\varphi=0}^{\pi} \cos(kR\theta \cos \varphi) d\varphi. \quad (\text{B.23})$$

In Eq. (B.21), we furthermore substitute $\theta/\text{NA}_B = \alpha$ and $d\theta = \text{NA}_B d\alpha$. Thus, the signal drop explicitly reads

$$\Delta P(R) = 2m_1(R) \Delta P \int_{\alpha=0}^{\infty} \exp(-\alpha^2) J_0(kR\alpha \text{NA}_B) \alpha d\alpha. \quad (\text{B.24})$$

Utilizing the Taylor expansion of the Bessel function $J_0(x) = \sum_{l=0}^{\infty} \frac{(-1)^l}{2^{(2l)} l! l!} x^{(2l)}$ then yields

$$\Delta P(R) = 2m_1(R) \Delta P \int_{\alpha=0}^{\infty} \exp(-\alpha^2) \sum_{l=0}^{\infty} \frac{(-1)^l}{2^l l! l!} (kR\alpha \text{NA}_B)^{(2l)} \alpha d\alpha. \quad (\text{B.25})$$

Now, by substituting $\beta = \alpha^2$ and by taking the sum out of the integral, we obtain

$$\Delta P(R) = m_1(R) \Delta P \sum_{l=0}^{\infty} \frac{(-1)^l}{l! l!} \left(\frac{kR \text{NA}_B}{2} \right)^l \underbrace{\int_{\beta=0}^{\infty} \beta^l \exp(-\beta) d\beta}_{=(-1)^l \frac{d^l}{dx^l} \int_{\beta=0}^{\infty} \exp(-x\beta) d\beta = \frac{d^l}{dx^l} \frac{1}{x} = l!}, \quad (\text{B.26})$$

where x is an auxiliary variable.

We obtain the final equation that models the signal drop when the small particle is outside the focus but within the focal plane by using the relation $kR \text{NA}_B = R/w_0$ and by identifying $\sum_{l=0}^{\infty} \frac{(-1)^l}{l!} x^l = \exp(-x)$:

$$\Delta P(R) = m_1(R) \exp[-(R/w_0)^2] \Delta P = m_1^2(R) \Delta P. \quad (\text{B.27})$$

Finally, we can state that the decay of the signal drop will be Gaussian when the particle is placed off-axis but still within the focal plane.

Bibliography

- [1] T. H. Maiman, *Stimulated Optical Radiation in Ruby*, Nature **187**, 493 (1960).
- [2] J. D. Jackson, *Classical Electrodynamics* (John Wiley & Sons, Inc., 1998), 3rd edition.
- [3] V. G. Veselago, *The Electrodynamics of Substances with Simultaneously Negative Values of ϵ and μ* , Sov. Phys. Usp. **10**, 509 (1968).
- [4] J. B. Pendry, A. J. Holden, D. J. Robbins, and W. J. Stewart, *Magnetism from Conductors and Enhanced Nonlinear Phenomena*, IEEE Trans. on Microwave Theory Tech. **47**, 2075 (1999).
- [5] J. B. Pendry, *Negative Refraction Makes a Perfect Lens*, Phys. Rev. Lett. **85**, 3966 (2000).
- [6] M. Born and E. Wolf, *Principles of Optics* (Cambridge University Press, 1999), 7th edition.
- [7] U. Leonhardt, *Optical Conformal Mapping*, Science **312** (5781), 1777 (2006).
- [8] J. B. Pendry, D. Schurig, and D. R. Smith, *Controlling Electromagnetic Fields*, Science **312** (5781), 1780 (2006).
- [9] D. Schurig, J. J. Mock, B. J. Justice, S. A. Cummer, J. B. Pendry, A. F. Starr, and D. R. Smith, *Metamaterial Electromagnetic Cloak at Microwave Frequencies*, Science **314** (5801), 977 (2006).
- [10] W. Cai, U. K. Chettiar, A. V. Kildishev, and V. M. Shalaev, *Optical Cloaking with Metamaterials*, Nature Photon. **1**, 224 (2007).
- [11] J. Valentine, J. Li, T. Zentgraf, G. Bartal, and X. Zhang, *An Optical Cloak made of Dielectrics*, Nat. Mater. **8**, 568 (2009).
- [12] L. H. Gabrielli, J. Cardenas, C. B. Poitras, and M. Lipson, *Silicon Nanostructure Cloak Operating at Optical Frequencies*, Nature Photon. **3**, 461 (2009).
- [13] Y. G. Ma, C. K. Ong, T. Tyc, and U. Leonhardt, *An Omnidirectional Retroreflector Based on the Transmutation of Dielectric Singularities*, Nat. Mater. **8**, 639 (2009).

- [14] V. M. Shalaev, *Optical Negative-Index Metamaterials*, Nature Photon. **1** (1), 41 (2007).
- [15] C. M. Soukoulis, S. Linden, and M. Wegener, *Negative Refractive Index at Optical Wavelengths*, Science **315** (5808), 47 (2007).
- [16] M. W. Klein, C. Enkrich, M. Wegener, and S. Linden, *Second-Harmonic Generation from Magnetic Metamaterials*, Science **313**, 502 (2006).
- [17] M. W. Klein, M. Wegener, N. Feth, and S. Linden, *Experiments on Second- and Third-Harmonic Generation from Magnetic Metamaterials*, Opt. Express **15**, 5238 (2007).
- [18] M. W. Klein, M. Wegener, N. Feth, and S. Linden, *Experiments on Second- and Third-Harmonic Generation from Magnetic Metamaterials: Erratum*, Opt. Express **16**, 8055 (2008).
- [19] C. E. Kriegler, M. S. Rill, S. Linden, and M. Wegener, *Bianisotropic Photonic Metamaterials*, IEEE J. Sel. Top. Quantum Electron. (accepted for publication) (2009).
- [20] L. Novotny and B. Hecht, *Principles of Nano-Optics* (Cambridge University Press, 2007).
- [21] J. Kästel and M. Fleischhauer, *Quantum Electrodynamics in Media with Negative Refraction*, Laser Phys. **15**, 135 (2005).
- [22] E. Hecht, *Optik* (Oldenbourg Verlag, 2005).
- [23] C. F. Bohren and D. R. Huffman, *Absorption and Scattering by Small Particles* (John Wiley & Sons, Inc., 1983).
- [24] H. A. Lorentz, *Über die Beziehung zwischen der Fortpflanzungsgeschwindigkeit des Lichtes und der Körperdichte*, Ann. Phys. **9**, 641 (1880).
- [25] M. O. Scully and M. S. Zubairy, *Quantum Optics* (Cambridge University Press, 1997).
- [26] P. Drude, *Zur Elektronentheorie der Metalle*, Ann. Phys. **306**, 566 (1900).
- [27] P. B. Johnson and R. W. Christy, *Optical Constants of the Noble Metals*, Phys. Rev. B **6** (12), 4370 (Dec 1972).
- [28] N. E. Christensen and B. O. Seraphin, *Relativistic Band Calculations and the Optical Properties of Gold*, Phys. Rev. B **4**, 3321 (1971).
- [29] L. Solymar and E. Shamonina, *Waves in Metamaterials* (Oxford University Press, 2009).
- [30] A. Otto, *Excitation of Nonradiative Surface Plasma Waves in Silver by the Method of Frustrated Total Reflection*, Z. Phys. **216**, 398 (1968).

- [31] E. Kretschmann and Raether H., *Radiative Decay of Nonradiative Surface Plasmons Excited by Light*, Z. Naturforsch. A **23**, 2135 (1968).
- [32] Y. Teng and E. A. Stern, *Plasma Radiation from Metal Grating Surfaces*, Phys. Rev. Lett. **19**, 511 (1967).
- [33] R. B. Pettit, S. Silcox, and R. Vincent, *Measurement of Surface-Plasmon Dispersion in Oxidized Aluminum Films*, Phys. Rev. B **11**, 3116 (1975).
- [34] U. Kreibig and M. Vollmer, *Optical Properties of Metal Clusters*, Springer Series in Materials Science 25 (Springer-Verlag, 1995).
- [35] R. Ruppin, *Plasmon Frequencies of Cube Shaped Metal Clusters*, Z. Phys. D **36**, 69 (1996).
- [36] H. S. Zhou, I. Honma, H. Komiyama, and J. W. Haus, *Controlled Synthesis and Quantum-Size Effect in Gold-Coated Nanoparticles*, Phys. Rev. B **50**, 12052 (1994).
- [37] R. D. Averitt, D. Sarkar, and N. J. Halas, *Plasmon Resonance Shifts of Au-Coated Au₂S Nanoshells: Insight into Multicomponent Nanoparticle Growth*, Phys. Rev. Lett. **78**, 4217 (1997).
- [38] S. Linden, C. Enkrich, M. Wegener, J. F. Zhou, T. Koschny, and C. M. Soukoulis, *Magnetic Response of Metamaterials at 100 Terahertz*, Science **306** (5700), 1351 (2004).
- [39] S. Zhang, W. J. Fan, N. C. Panoiu, K. J. Malloy, R. M. Osgood, and S. R. J. Brueck, *Experimental Demonstration of Near-Infrared Negative-Index Metamaterials*, Phys. Rev. Lett. **95** (13), 137404 (2005).
- [40] G. Mie, *Beiträge zur Optik trüber Medien, speziell kolloidaler Metallösungen*, Ann. Phys. **25**, 377 (1908).
- [41] M. Abramowitz and I. A. Stegun (eds.), *Handbook of Mathematical Functions with Formulas, Graphs and Mathematical Tables*, volume 10 of *Applied Mathematics Series 55* (National Bureau of Standards, 1972).
- [42] P. A. Franken, A. E. Hill, C. W. Peters, and G. Weinreich, *Generation of Optical Harmonics*, Phys. Rev. Lett. **7**, 118 (1961).
- [43] G. P. Agarwal, *Nonlinear Fiber Optics* (Academic Press, 2001).
- [44] R. W. Boyd, *Nonlinear Optics* (Academic Press, 2008), 3rd edition.
- [45] Y. R. Shen, *The Principles of Nonlinear Optics* (John Wiley & Sons, Inc., 1984).
- [46] R. Dendy, *Plasma Physics: An Introductory Course* (Cambridge University Press, 1993).

- [47] Y. Zeng, W. Hoyer, J. Liu, S. W. Koch, and J. V. Moloney, *Classical Theory for Second-Harmonic Generation from Metallic Nanoparticles*, Phys. Rev. B **79**, 235105 (2009).
- [48] E. Yablonovitch, *Inhibited Spontaneous Emission in Solid-State Physics and Electronics*, Phys. Rev. Lett. **58**, 2059 (1987).
- [49] J. Nelayah, M. Kociak, O. Stéphan, J. Garcia de Abajo, M. Tencé, L. Henrard, D. Taverna, I. Pastoriza-Santos, L. M. Liz-Marzan, and C. Colliex, *Mapping Surface Plasmons on a Single Metallic Nanoparticle.*, Nature Phys. **3**, 348 (2007).
- [50] R. H. Ritchie, *Plasma Losses by Fast Electrons in Thin Films*, Phys. Rev. **106**, 874 (1957).
- [51] M. Sunjic and A. A. Lucas, *Multiple Plasmon Effects in the Energy-Loss Spectra of Electrons in Thin Films*, Phys. Rev. B **3**, 719 (1971).
- [52] T. L. Ferrell and P. M. Echenique, *Generation of Surface Excitations on Dielectric Spheres by an External Electron Beam*, Phys. Rev. Lett. **55**, 1526 (1985).
- [53] F. J. Garcia de Abajo and M. Kociak, *Probing the Photonic Local Density of States with Electron Energy Loss Spectroscopy*, Phys. Rev. Lett. **100**, 106804 (2008).
- [54] U. Hohenester, H. Ditlbacher, and K. R. Krenn, *Electron-Energy-Loss Spectra of Plasmonic Nanoparticles*, Phys. Rev. Lett. **103**, 106801 (2009).
- [55] B. E. A. Saleh and M. C. Teich, *Fundamentals of Photonics* (Wiley&Sons, 2007), 2nd edition.
- [56] S. Zhang, W. Fan, K. J. Malloy, S. R. J. Brueck, N. C. Panoiu, and R. M. Osgood, *Near-Infrared Double Negative Metamaterials*, Opt. Express **13**, 4922 (2005).
- [57] J. B. Pendry, *A Chiral Route to Negative Refraction*, Science **306**, 1353 (2004).
- [58] R. Merlin, *Analytical Solution of the Almost-Perfect-Lens Problem*, Appl. Phys. Lett. **84**, 1290 (2004).
- [59] J. B. Pendry, A. J. Holden, W. J. Stewart, and I. Youngs, *Extremely Low Frequency Plasmons in Metallic Mesostructures*, Phys. Rev. Lett. **76**, 4773 (1996).
- [60] R. A. Shelby, D. R. Smith, and S. Schultz, *Experimental Verification of a Negative Index of Refraction*, Science **292**, 77 (2001).
- [61] G. Dolling, C. Enkrich, M. Wegener, C. M. Soukoulis, and S. Linden, *Simultaneous Negative Phase and Group Velocity of Light in a Metamaterial*, Science **312** (5775), 892 (2006).

- [62] G. Dolling, C. Enkrich, M. Wegener, C. M. Soukoulis, and S. Linden, *Low-Loss Negative-Index Metamaterial at Telecommunication Wavelengths*, *Opt. Lett.* **31** (12), 1800 (2006).
- [63] S. Linden, M. Decker, and M. Wegener, *Model System for a One-Dimensional Magnetic Photonic Crystal*, *Phys. Rev. Lett.* **97**, 083902 (2007).
- [64] N. Feth, C. Enkrich, M. Wegener, and S. Linden, *Large-Area Magnetic Metamaterials via Compact Interference Lithography*, *Opt. Express* **15**, 501 (2007).
- [65] W. N. Hardy and L. A. Whitehead, *Split-Ring Resonator for Use in Magnetic Resonance From 200-2000MHz*, *Rev. Sci. Instrum.* **52**, 213 (1981).
- [66] J. Zhou, T. Koschny, M. Kafesaki, E. N. Economou, J. B. Pendry, and C. M. Soukoulis, *Saturation of the Magnetic Resonance of Split-Ring Resonators at Optical Frequencies*, *Phys. Rev. Lett.* **95**, 223902 (2005).
- [67] M. W. Klein, C. Enkrich, M. Wegener, C. M. Soukoulis, and S. Linden, *Single-Slit Split-Ring Resonators at Optical Frequencies: Limits of Size Scaling*, *Opt. Lett.* **31**, 1259 (2006).
- [68] Pérez-Willard F. Enkrich, C., D. Gerthsen, J. Zhou, T. Koschny, C. M. Soukoulis, M. Wegener, and S. Linden, *Focused-Ion-Beam Nanofabrication of Near-Infrared Magnetic Metamaterials*, *Adv. Mater.* **17**, 2547 (2005).
- [69] S. Linden, C. Enkrich, G. Dolling, M. W. Klein, J. Zhou, T. Koschny, C. M. Soukoulis, M. Burger, F. Schmidt, and M. Wegener, *Photonic Metamaterials: Magnetism at Optical Frequencies*, *IEEE J. Sel. Top. Quantum Electron.* **12**, 1097 (2006).
- [70] T. P. Meyrath, T. Zentgraf, and H. Giessen, *Lorentz Model for Metamaterials: Optical Frequency Resonance Circuits*, *Phys. Rev. B* **75**, 205102 (2007).
- [71] C. Enkrich, M. Wegener, S. Linden, S. Burger, L. Zschiedrich, F. Schmidt, J. Zhou, T. Koschny, and C. M. Soukoulis, *Magnetic Metamaterials at Telecommunication and Visible Frequencies*, *Physical Review Letters* **95**, 203901 (2005).
- [72] T. J. Yen, W. J. Padilla, N. Fang, D. C. Vier, D. R. Smith, J. B. Pendry, D. N. Basov, and X. Zhang, *Terahertz Magnetic Response from Artificial Materials*, *Science* **303**, 1494 (2004).
- [73] G. Dolling, C. Enkrich, M. Wegener, J. F. Zhou, and C. M. Soukoulis, *Cut-Wire Pairs and Plate Pairs as Magnetic Atoms for Optical Metamaterials*, *Opt. Lett.* **30**, 3198 (2005).
- [74] G. Dolling, *Design, Fabrication, and Characterization of Double-Negative Metamaterials for Photonics*, Ph.D. thesis, University of Karlsruhe (TH) (2007).

- [75] J. Valentine, S. Zhang, T. Zentgraf, E. Ulin-Avila, D. A. Genov, G. Bartal, and X. Zhang, *Three-Dimensional Optical Metamaterial with a Negative Refractive Index*, *Nature* **455**, 376 (2008).
- [76] G. Dolling, M. Wegner, C. M. Soukoulis, and S. Linden, *Negative-Index Metamaterial at 780 nm Wavelength*, *Opt. Lett.* **32**, 53 (2007).
- [77] G. Dolling, M. Wegener, and S. Linden, *Realization of a Three-Functional-Layer Negative-Index Photonic Metamaterial*, *Opt. Lett.* **32**, 551 (2007).
- [78] G. Dolling, M. Wegener, A. Schädle, S. Burger, and S. Linden, *Observation of Magnetization Waves in Negative-Index Photonic Metamaterials*, *Appl. Phys. Lett.* **89**, 231118 (2006).
- [79] W. Wu, E. Kim, E. Ponizovskaya, Y. Liu, Z. Yu, N. Fang, Y. R. Shen, A. M. Bratkovsky, W. Tong, C. Sun, X. Zhang, S.-Y. Wang, and R. S. Williams, *Optical Metamaterials at Near and Mid-IR Range Fabricated by Nanoimprint Lithography*, *Appl. Phys. A* **87**, 143 (2007).
- [80] R. Ruppin, *Surface Polaritons of a Left-Handed Medium*, *Phys. Lett. A* **277**, 61 (2000).
- [81] K. Busch, G. von Freymann, S. Linden, S. F. Mingalaevev, L. Tkeshelashvili, and M. Wegener, *Periodic Nanostructures for Photonics*, *Phys. Rep.* **444**, 101 (2007).
- [82] C. F. Klingshirn, *Semiconductor Optics* (Springer-Verlag, 2005), 2nd edition.
- [83] M. I. Stockman, *Criterion for Negative Refraction with Low Optical Losses from a Fundamental Principle of Causality*, *Phys. Rev. Lett.* **98**, 177404 (2007).
- [84] P. Kinsler and M. W. McCall, *Causality-Based Criteria for a Negative Refractive Index Must Be Used With Care*, *Phys. Rev. Lett.* **101**, 167401 (2008).
- [85] C. Enkrich, *Metamaterials for Photonics*, Ph.D. thesis, University Karlsruhe (TH) (2006).
- [86] *Data Sheet Heraeus Suprasil 3001 and 3002* .
- [87] C. Guillen and J. Herrero, *Comparison Study of ITO Thin Films Deposited by Sputtering at Room Temperature onto Polymer and Glass Substrates*, *Thin Solid Films* **480**, 129 (2005).
- [88] Y. Zhu, H. Inada, K. Nakamura, and J. Wall, *Imaging Single Atoms Using Secondary Electrons with an Aberration-Corrected Electron Microscope*, *Nat. Mater.* **8**, 808 (2009).
- [89] P. Rai-Choudhury (ed.), *SPIE Handbook of Microlithography, Micromachining, and Microfabrication* (SPIE, 1980).

- [90] S. Yasin, D. G. Hasko, and H. Ahmed, *Fabrication of $< 5\text{nm}$ - Width Lines in Poly(methylmethacrylate) Resist Using a Water: Isopropyl Alcohol Developer and Ultrasonically-Assisted Development*, Appl. Phys. Lett. **78**, 2760 (2001).
- [91] A. A. Tseng, *Recent Developments in Micromilling Using Focused Ion Beam Technology*, J. Micromech. Microeng. **14**, R15 (2004).
- [92] S. R. J. Brueck, *Optical and Interferometric Lithography – Nanotechnology Enablers*, Proc. IEEE **93**, 1704 (2005).
- [93] S. Zhang, W. Fan, B. K. Minhas, A. Frauenglass, K. J. Malloy, and S. R. J. Brueck, *Midinfrared Resonant Magnetic Nanostructures Exhibiting a Negative Permeability*, Phys. Rev. Lett. **94**, 037402 (2005).
- [94] S. Y. Chou, P. R. Krauss, and P. J. Renstrom, *Imprint Lithography with 25-Nanometer Resolution*, Science **272**, 85 (1996).
- [95] M. Bender, A. Fuchs, U. Plachetka, and H. Kurz, *Status and Prospects of UV-Nanoimprint Technology*, Microelectron. Eng. **83**, 827 (2006).
- [96] M. W. Klein, *Nonlinear Optics of Metallic Photonic Crystal Slabs and Planar Metamaterials*, Ph.D. thesis, University Karlsruhe (TH) (2006).
- [97] C. Sönnichsen, S. Geier, N. E. Hecker, G. von Plessen, J. Feldmann, H. Ditlbacher, B. Lamprecht, J. R. Krenn, F. R. Aussenegg, V. Z-H. Chan, J. P. Spatz, and M. Möller, *Spectroscopy of Single Metallic Nanoparticles Using Total Internal Reflection Microscopy*, Appl. Phys. Lett. **77**, 2949 (2000).
- [98] C. Sönnichsen, T. Franzel, T. Wilk, G. von Plessen, and J. Feldmann, *Drastic Reduction of Plasmon Damping in Gold Nanorods*, Phys. Rev. Lett. **88**, 077402 (2002).
- [99] G. Wrigge, I. Gerhardt, J. Hwang, G. Zumofen, and V. Sandoghdar, *Efficient Coupling of Photons to a Single Molecule and the Observation of its Resonance Fluorescence*, Nat. Phys. **4**, 60 (2008).
- [100] P. Kukura, M. Celebrano, A. Renn, and V. Sandoghdar, *Imaging a Single Quantum Dot when It Is Dark*, Nano Lett. **9**, 926 (2009).
- [101] A. Arbouet, D. Christofilos, N. Del Fatti, F. Vallee, J. R. Huntzinger, L. Arnaud, L. Billaud, and M. Broyer, *Direct Measurement of the Single-Metal-Cluster Optical Absorption*, Phys. Rev. Lett. **93**, 127401 (2004).
- [102] O. L. Muskens, N. Del Fatti, F. Vallee, J. R. Huntzinger, P. Billaud, and M. Broyer, *Single Metal Nanoparticle Absorption Spectroscopy and Optical Characterization*, Appl. Phys. Lett. **88**, 063109 (2006).
- [103] M. Gehrtz, G. C. Bjorklund, and E. A. Whittaker, *Quantum-Limited Laser Frequency-Modulation spectroscopy*, J. Opt. Soc. Am. B **2**, 1510 (1985).

- [104] M.W. Klein, *Theory for the Single-Particle Extinction Experiment*, 11th October 2007.
- [105] M. Husnik, *Spektroskopische Untersuchung des absoluten Extinktionquerschnitts eines einzelnen Split-Ring Resonators*, Master's thesis, University Karlsruhe (TH) (2008).
- [106] M. N'Gom, J. Ringnalda, J. F. Mansfield, Agarwal A., N. Kotov, N. J. Zaluzec, and T. B. Norris, *Single Particle Plasmon Spectroscopy of Silver Nanowires and Gold Nanorods*, *Nano Lett.* **8**, 3200 (2008).
- [107] J. Nelayah, L. Gu, C. T. Koch, I. Pastoriza-Santos, L. M. Liz-Marzan, and P. A. van Aken, *Direct Imaging of Surface-Plasmon Resonances on Single Triangular Silver Nanoprisms at Optical Wavelength Using Low-Loss EFTEM imaging*, *Opt. Lett.* **34**, 1003 (2009).
- [108] M.-W. Chu, V. Myroshnychenko, C. H. Chen, J.-P. Deng, C.-Y. Mou, and F. J. Garcia de Abajo, *Probing Bright and Dark Surface-Plasmon Modes in Individual and Coupled Nanoparticles Using an Electron Beam*, *Nano Lett.* **9**, 399 (2009).
- [109] E. A. Ash and G. Nichols, *Super-Resolution Aperture Scanning Microscope*, *Nature* **237**, 510 (1970).
- [110] T. A. Klar, S. Jakobs, M. Dyba, A. Egner, and S. W. Hell, *Fluorescence Microscopy with Diffraction Resolution Barrier Broken by Stimulated Emission*, *PNAS* **97**, 8206 (1997).
- [111] M. Kuttge, E. J. R. Vesseur, A. F. Koenderink, H. J. Lezec, H. A. Atwater, F. J. Garcia de Abajo, and A. Polman, *Local Density of States, Spectrum, and Far-Field Interference of Surface Plasmon Polaritons Probed by Cathodoluminescence*, *Phys. Rev. B* **79**, 113405 (2009).
- [112] C. Jeanguillaume and C. Colliex, *Spectrum-Image: the Next Step in EELS Digital Acquisition and Processing*, *Ultramicroscopy* **28**, 252 (1989).
- [113] M. Kociak, O. Stéphan, M. G. Walls, M. Tencé, and C. Colliex, *Spatially Resolved EELS: the Spectrum-Imaging Technique and Its Applications* (Springer-Verlag, 2010).
- [114] R. F. Egerton, H. Qian, and M. Malac, *Improving the Energy Resolution of X-Ray and Electron Energy-Loss Spectra*, *Micron* **37**, 310 (2006).
- [115] W. H. Richardson, *Bayesian Iterative Method of Image Restoration*, *J. Opt. Soc. Am. A* **62**, 55 (1972).
- [116] L. B. Lucy, *An Iterative Technique for the Rectification of Observed Distributions*, *Astron. Journal* **79**, 745 (1974).

- [117] A. Gloter, A. Douir, M. Tence, and C. Colliex, *Improving Energy Resolution of EELS Spectra: an Alternative to the Monochromator solution*, *Ultramicroscopy* **96**, 385 (2003).
- [118] D. Reefman, *Towards Higher Resolution: a Mathematical Approach*, volume 10 of *Defect and Microstructure Analysis by Diffraction* (Oxford University Press, 2000).
- [119] E. Kim, F. Wang, W. Wei, Z. Yu, and Y. R. Shen, *Nonlinear Optical Spectroscopy of Photonic Metamaterials*, *Phys. Rev. B* **78**, 113102 (2008).
- [120] A. K. Popov and V. M. Shalaev, *Compensating Losses in Negative-Index Metamaterials by Optical Parametric Amplification*, *Opt. Lett.* **31**, 2169 (2006).
- [121] A. K. Popov and V. M. Shalaev, *Negative-Index Metamaterials: Second-Harmonic Generation, Manley-Rowe Relations and Parametric Amplification*, *Appl. Phys. B* **84**, 131 (2006).
- [122] I. R. Gabitov, R. A. Indik, N. M. Litchinitser, A. I. Maimistov, V. M. Shalaev, and J. E. Soneson, *Double-Resonant Optical Materials with Embedded Metal Nanostructures*, *J. Opt. Soc. Am. B* **23**, 535 (2006).
- [123] I. V. Shadrivov, A. A. Zharov, and Y. S. Kivshar, *Second-Harmonic Generation in Nonlinear Left-Handed Metamaterials*, *J. Opt. Soc. Am. B* **23**, 529 (2006).
- [124] W. L. Schaich, *Second Harmonic Generation by Periodically-Structured Metal Surfaces*, *Phys. Rev. B* **78**, 195416 (2008).
- [125] B. K. Canfield, S. Kujala, K. Jefimovs, Y. Svirko, J. Turunen, and M. Kauranen, *A Macroscopic Formalism to Describe the Second-Order Nonlinear Optical Response of Nanostructures*, *J. Opt. A: Pure Appl. Opt.* **8**, S278 (2006).
- [126] H. Husu, B. K. Canfield, J. Laukkanen, B. Bai, M. Kuittinen, J. Turunen, and M. Kauranen, *Local-Field Effects in the Nonlinear Optical Response of Metamaterials*, *Metamaterials* **2**, 155 (2008).
- [127] M. D. McMahon, R. Lopez, R. F. Haglund, E. A. Ray, and P. H. Bunton, *Second-Harmonic Generation From Arrays of Symmetric Gold Nanoparticles*, *Phys. Rev. B* **73**, 041401(R) (2006).
- [128] N. Feth, S. Linden, M. W. Klein, M. Decker, F. B. P. Niesler, Y. Zeng, W. Hoyer, J. Liu, S. W. Koch, J. V. Moloney, and M. Wegener, *Second-Harmonic Generation from Complementary Split-Ring Resonators*, *Opt. Lett.* **33** (17), 1975 (2008).
- [129] F. Falcone, T. Lopetegi, M. A. G. Laso, J. D. Baena, J. Bonache, M. Beruete, R. Marques, F. Martin, and M. Sorolla, *Babinet Principle Applied to the Design of Metasurfaces and Metamaterials*, *Phys. Rev. Lett.* **93**, 197401 (2004).

- [130] T. Zentgraf, T. P. Meyrath, A. Seidel, S. Kaiser, H. Giessen, C. Rockstuhl, and F. Lederer, *Babinet's Principle for Optical Frequency Metamaterials and Nanoantennas*, Phys. Rev. B **76**, 033407 (2007).
- [131] A. Taflove and S. C. Hagness, *Computational Electrodynamics: The Finite-Difference Time-Domain Method* (Norwood, MA: Artech House, 2005), 3rd edition.
- [132] Y. Zeng and J. V. Moloney, *Volume Electric Dipole Origin of Second-Harmonic Generation from Metallic Membrane with Noncentrosymmetric Patterns*, Opt. Lett. **34**, 2844 (2009).
- [133] F. X. Wang, F. J. Rodriguez, W. M. Albers, R. Ahorinta, J. E. Sipe, and M. Kauranen, *Surface and Bulk Contributions to the Second-Order Nonlinear Optical Response of a Gold Film*, Phys. Rev. B **80**, 233402 (2009).
- [134] N. Liu, H. Guo, L. Fu, S. Kaiser, H. Schweizer, and H. Giessen, *Three-Dimensional Photonic Metamaterials at Optical Frequencies*, Nat. Mater. **7**, 31 (2008).
- [135] M. C. K. Wiltshire, E. Shamonina, I. R. Young, and L. Solymar, *Dispersion Characteristics of Magneto-Inductive Waves: Comparison Between Theory and Experiment*, Electron. Lett. **39**, 215 (2003).
- [136] F. Hesmer, E. Tatartschuk, O. Zhuromskyy, A. A. Radkovskaya, M. Shamonin, T. Hao, C. J. Stevens, G. Faulkner, D. J. Edwards, and E. Shamonina, *Coupling Mechanisms for Split Ring Resonators: Theory and Experiment*, Phys. Status Solidi B **244**, 1170 (2007).
- [137] C. Dahmen, B. Schmidt, and G. von Plessen, *Radiation Damping in Metal Nanoparticle Pairs*, Nano Lett. **7**, 318 (2007).
- [138] P. Olk, J. Renger, M. T. Wenzel, and L. M. Eng, *Distance Dependent Spectral Tuning of two Coupled Metal Nanoparticles*, Nano Lett. **8**, 1174 (2008).
- [139] M. Decker, S. Linden, and M. Wegener, *Coupling Effects in Low-Symmetry Planar Split-Ring Resonator Arrays*, Opt. Lett. **34**, 1579 (2009).
- [140] M. Husnik, M. W. Klein, N. Feth, M. König, J. Niegemann, K. Busch, S. Linden, and M. Wegener, *Absolute Extinction Cross-Section of Individual Magnetic Split-Ring Resonators*, Nature Photon. **2**, 614 (2008).
- [141] N. Liu, H. Liu, S. Zhu, and H. Giessen, *Stereometamaterials*, Nature Photon. **3**, 157 (2009).
- [142] O. Sydoruk, O. Zhuromskyy, E. Shamonina, and L. Solymar, *Phonon-Like Dispersion Curves of Magnetoinductive Waves*, Appl. Phys. Lett. **87**, 072501 (2005).

- [143] W. Rechberger, A. Hohenau, A. Leitner, J. R. Krenn, B. Lamprecht, and F. R. Aussenegg, *Optical Properties of Two Interacting Gold Nanoparticles*, *Opt. Commun.* **220**, 137 (2003).
- [144] K.-H. Su, Q.-H. Wei, X. Zhang, J. J. Mock, D. R. Smith, and S. Schultz, *Interparticle Coupling Effects on Plasmon Resonances of Nanogold Particles*, *Nano Letters* **3**, 1087 (2003).
- [145] A. M. Funston, C. Novo, T. J. Davis, and P. Mulvaney, *Plasmon Coupling of Gold Nanorods at Short Distances and in Different Geometries*, *Nano Lett.* **9**, 1651 (2009).
- [146] J. S. Hesthaven and T. Warburton, *Nodal High-order Methods on Unstructured Grids - I. Time-Domain Solution of Maxwell's Equations*, *J. Comput. Phys.* **181**, 186 (2002).
- [147] J. Niegemann, M. König, K. Stannigel, and K. Busch, *Higher-Order Time-Domain Methods for the Analysis of Nano-Photonic Systems*, *Photonics Nanostruct. Fundam. Appl.* **7**, 2 (2009).
- [148] K. Stannigel, M. König, J. Niegemann, and K. Busch, *Discontinuous Galerkin Time-Domain Computations of Metallic Nanostructures*, *Opt. Express* **17**, 14934 (2009).
- [149] B. T. Drain and P. J. Flatau, *Discrete-Dipole Approximation for Scattering Calculations*, *J. Opt. Soc. Am. A* **11**, 1491 (1994).
- [150] M. Moskovits, *Surface-Enhanced Spectroscopy*, *Rev. Mod. Phys.* **57**, 783 (1985).
- [151] Y. W. C. Cao, R. Jin, and C. A. Mirkin, *Nanoparticles with Raman Spectroscopic Fingerprints for DNA and RNA Detection*, *Science* **297**, 1536 (2002).
- [152] D. J. Bergman and M. I. Stockman, *Surface Plasmon Amplification by Stimulated Emission of Radiation: Quantum Generation of Coherent Surface Plasmons in Nanosystems*, *Phys. Rev. Lett.* **90**, 027402 (2003).
- [153] M. A. Noginov, G. Zhu, A. M. Belgrave, R. Bakker, V. M. Shalaev, E. E. Narimanov, E. Herz, T. Suteewong, and U. Wiesner, *Demonstration of a Spaser-Based Nanolaser*, *Nature* **460**, 1110 (2009).
- [154] R. F. Oulton, V. J. Sorger, T. Zentgraf, R. Ma, C. Gladden, L. Dai, G. Bartal, and X. Zhang, *Plasmon Laser at Deep Subwavelength Scale*, *Nature* **461**, 629 (2009).
- [155] T. Zentgraf, J. Dorfmueller, C. Rockstuhl, C. Etrich, R. Vogelgesang, K. Kern, T. Pertsch, F. Lederer, and H. Giessen, *Amplitude- and Phase-Resolved Optical Near Fields of Split-Ring-Resonator-Based Metamaterials*, *Opt. Lett.* **33**, 848 (2008).
- [156] E. D. Palik, *Handbook Of Optical-Constants*, volume 1 (Academic Press, 1984).
- [157] N. Papasimakis, V. A. Fedotov, Y. H. Fu, D. P. Tsai, and N. I. Zheludev, *Coherent and Incoherent Metamaterials and Order-Disorder Transitions*, *Phys. Rev. B* **80**, 041102(R) (2009).

-
- [158] S. Zhang, D. A. Genov, Y. Wang, M. Liu, and X. Zhang, *Plasmon-Induced Transparency in Metamaterials*, Phys. Rev. Lett. **101**, 047401 (2008).
- [159] T. J. Davis, K. C. Vernon, and D. E. Gómez, *Designing Plasmonic Systems using Optical Coupling between Nanoparticles*, Phys. Rev. B **79**, 155423 (2009).

Acknowledgments

It is a beautiful tradition to dedicate the last pages of a thesis to saying thank you to people who contributed to this thesis.

Clearly, at first I want to thank my advisor Prof. Dr. Martin Wegener for giving me the opportunity to work in and to contribute to the research of his group which is outstanding in the world. He also gave me the chance to explore three very different characterization methods of metallic nanoparticles. In many discussions and group meetings, I definitively benefited a lot from his profound knowledge. He gave numerous hints, comments, and great ideas that contributed to the success of my thesis. Besides the intellectual input, he took great care of the financial support such that nearly every idea could be realized. Especially, it has been a pleasure to me to present our results on conferences.

Dr. Stefan Linden was officially my co-advisor but in fact his contributions were ingredients of major importance assuring the success of this thesis. He was supporting and steering my work starting with my diploma thesis. My enthusiasm and knowledge about the field of metamaterials was raised in so many discussions with him – thank you! It was a pleasure to work in his Helmholtz-Hochschul-Nachwuchsgruppe "Metamaterials for Photonics". I am also grateful for his contributions beyond the every-day work.

I would like to acknowledge Prof. Dr. Kurt Busch for kindly agreeing to co-referee this thesis. Furthermore, he is co-authoring three papers that we could published along the way of this work. He and parts of his group, namely Dr. Jens Niegemann and Michael König contributed to the success of this work by discussions and numerical support on the optical properties of isolated photonic atoms.

I want to express my gratitude to Prof. Dr. Stephan W. Koch and Prof. Dr. Jerome V. Moloney and their groups for theoretical support regarding the second-harmonic generation in planar metamaterial arrays.

Our electron-energy-loss-spectroscopy project would not have been possible without the experiments conducted out by Guillaume Boudarham, Dr. Mathieu Kociak, and Prof. Dr. Christian Colliex from the group of Prof. Dr. Odile Stéphane. I am grateful for their work, for many discussions, and for their warm welcome at their laboratories in Paris. Especially, I would like to thank Mathieu for patiently answering many e-mails from me, the optics guy. Thanks to the diploma students I had the pleasure to work with and to learn from (in order of appearance): Mathias Ruther, Nina Meinzer, Martin Husnik, and Fabian Niesler.

Next, I would like to thank all members of the Wegener group for their support and stimulating and helpful discussion. Especially, I would like to mention Andreas Frölich and Dr. Matthias W. Klein: Andreas was partner in many fruitful discussions about the theoretical

background of electron-energy-loss spectroscopy. Matthias introduced me to the nonlinear optics on metamaterial arrays and gave invaluable input to the interpretation of the spatial-modulation spectroscopy.

I am indebted to all proof readers of this thesis for their supporting comments and many hints which improved the readability.

I would like to thank the workshops of the Institute of Applied Physics for their contributions without which this thesis would not have been possible. Especially thank goes to our former technician Thorsten Kuhn with whom I could discuss the feasibility of many experimental details – he deceased last year. Also the electronics workshop with Heinz Hoffmann, Helmuth Lay, and Werner Gilde has contributed by supplying parts for the experiments and taking care of our computing facilities. Furthermore, the secretary of the Institute of Applied Physics headed by Renate Helfen and the the secretary of the Institute of Nanotechnology, Erika Schütze, have assured that the administrative paper work has been well taken care of. The very last sentence is dedicated to my girl-friend Sabine, my family and friends, who did not contribute to the scientific part but even more important they gave loving support regarding all aspects of life.